SAND76-8001
Unlimited Release

Roll Torque Evaluation (RTE) Vehicle Postflight Test Report

J. K. Kryvoruka

Prepared by Sandia Laboratories, Albuquerque New Mexico 87115 and Livermore, California 94550 for the United States Energy Research and Development Administration under Contract AT (29-1) 789

Printed March 1976

When printing a copy of any digitized SAND Report, you are required to update the markings to current standards.

Sandia Laboratories

SF 2900 Q(7-73)

Issued by Sandia Laboratories, operated for the United States Energy Research and Development Administration by Sandia Corporation.

NOTICE

This report was prepared as an account of work sponsored by the United States Government. Neither the United States nor the United States Energy Research and Development Administration, nor any of their employees, nor any of their contractors, subcontractors, or their employees, makes any warranty, express or implied, or assumes any legal liability or responsibility for the accuracy, completeness or usefulness of any information, apparatus, product or process disclosed, or represents that its use would not infringe privately owned rights.

SAND76-8001
Unlimited Release
Printed March 1976

ROLL TORQUE EVALUATION (RTE) VEHICLE POSTFLIGHT TEST REPORT

J. K. Kryvoruka
Advanced Mechanical Division 8158
Sandia Laboratories

ABSTRACT

This report presents the results of analyses of the roll torque evaluation (RTE) vehicle, a reentry configuration which was flight-tested during May 1974 at the Sandia Laboratories Tonopah Test Range. The purpose of the test program was to evaluate, in a controlled environment, the roll-torque-producing effect of an ablating tape-wrapped carbon phenolic (TWCP) heat shield. The boost system, a Talos-Terrier-Recruit (TATER) rocket, delivered the reentry configuration to conditions approximating the latter portion of full-scale reentry while providing nominal payload separation. Flight instrumentation, designed to evaluate the aerodynamic performance and thermal response of the vehicle, indicates that the flight environment was severe enough to produce the desired level of ablation and that significant rolling moments were obtained. In addition, the vehicle was recovered intact for postflight inspection.

ACKNOWLEDGMENT

The author gratefully acknowledges the contributions made to the program by the following individuals:

R. D. Fellerhoff, 1324	Booster, Adapter and Separation System Mechanical Design and Interface
D. W. Johnson, 1332	Recovery System
L. R. Rollstin, 1335	Booster Trajectory Analysis
R. M. Green, 8111	Nosetip Aerothermodynamic Analysis
L. E. Voelker, 8113	Structural Analysis
F. W. Kent, 8116	Telemetry and Instrumentation System
H. D. Sorenson, 8183	Telemetry and Instrumentation System
J. Dremalas, 8157	Mechanical Drafting
M. H. Rogers, 8158	Heat Shield NDT
B. D. Pontsler, 8165	Mechanical Design and Coordination
D. M. Pegan, 8168	Mechanical Design and Hardware Procurement
R. F. Carrell, 8183-1	Instrumentation
D. C. Stoner, 8183-1	Instrumentation
T. T. Bramlette, 8313	Aerodynamics and Aerodynamic Heating and Ablation
T. F. Jones, 8345	Safety and Reliability
G. W. Henderson, 8362	Mass Properties
L. R. Myers, 8412	Testing Coordination and Data Reduction
K. Livingstone, 8412-1	Vehicle Assembly
S. Schwegel, 8431	Electrical Drafting

TABLE OF CONTENTS

	Page
Summary and Conclusions	15
Introduction	17
RTE Program Objectives	19
RTE Flight System Description	20
Booster	20
Flight Vehicle	20
Payload Adapter and Separation System	27
Instrumentation and Telemetry	28
Range Instrumentation and Support	28
Preflight Qualification Testing	28
Trajectory Analysis	30
General Flight Characteristics	30
Flight Trajectory Data	32
Meteorological Data	32
Payload Trajectory Characteristics	37
Aerodynamic Analysis	37
Flight Motion Data	37
Roll Dynamics Analysis	43
Aerodynamic Drag	44
Angular Motion	47
Static Stability	47
Aerothermodynamic Analysis	52
Heat Shield Thermal Data	53
Theoretical Heat Shield Aerodynamic Heating	54

	Page
Heat Shield Performance	55
Recovered RTE Heat Shield	57
Nosetip Performance	62
Nosetip Thermal Stress Analysis	73
References	77
Appendix A--RTE Heat Shield Construction	81
Appendix B--RTE Telemetry System Description	85
Appendix C--Summary of Ballistic Computations and Range Safety	99
Appendix D--RTE Postflight Trajectory Simulation	103/104

ILLUSTRATIONS

Figure		Page
1.	TATER Booster Schematic	21
2.	RTE/Booster Flight System	22
3.	Roll Torque Evaluation Vehicle Schematic	23
4a.	RTE Vehicle Assembly	24
4b.	RTE Payload Adapter and Separation System	25
5.	RTE Trajectory Events	31
6.	Payload Axial Acceleration History (±50g Accelerometer)	33
7.	Payload Axial Acceleration History (±100g Accelerometer)	33
8.	Comparison of Flight Velocity and Altitude History Derived from Radar and Onboard Accelerometer	34
9.	Observed Atmospheric Conditions--Speed of Sound Versus Altitude	36
10.	Observed Atmospheric Conditions--Air Density Versus Altitude	36
11.	RTE Payload Altitude History	38
12.	RTE Payload Velocity History	38
13.	RTE Payload Mach Number History	39
14.	RTE Payload Dynamic Pressure History	39
15.	RTE Payload Axial Acceleration History	40
16.	Pitching Velocity Versus Time	40
17.	Yawing Velocity Versus Time	41
18.	Rolling Velocity Versus Time	41
19.	Lateral Acceleration History (Body Z-Axis AZ-1)	42
20.	Lateral Acceleration History (Body Y-Axis AY-1)	42
21.	Lateral Acceleration History (Body Y-Axis AY-2)	43

Figure		Page
22.	Total Rolling Moment Coefficient Versus Flight Time	45
23.	Total Rolling Moment Coefficient Versus Flight Mach Number	45
24.	Comparison of RTE Total Rolling Moment Coefficient With Available Theory	46
25.	RTE Axial Force Coefficient (Wind Tunnel and Flight Data) Versus Mach Number	46
26.	Angle-of-Attack History (Computed From Flight Data)	48
27.	Angle-of-Sideslip History (Computed From Flight Data)	48
28.	Total Angle-of-Attack History (Computed From Flight Data)	49
29.	Aerodynamic Roll Angle History (Computed From Flight Data)	49
30.	RTE Normal Force Coefficient Versus Mach Number (From Wind Tunnel)	51
31.	RTE Static Stability Coefficient (C_{m_α}) Versus Mach Number (Comparison of RTE Flight Test and Wind Tunnel Data)	51
32.	Center-of-Pressure (X_{cp})	52
33.	RTE Spin Rate and Natural Pitch Frequency History	53
34.	RTE Heat Shield Temperature Response Versus Time (Flight Data)	54
35.	Cold Wall Convective Heat Transfer Rate (Station 2 and Aft of Station 9)	55
36.	Thermal Stack Temperature Response (Temperature History at Depths of 0.020, 0.040, and 0.10 Inch From the Cone Surface at Stations 19.0, 22.75, and 28.5)	56
37.	Theoretical and Flight Test Surface Recession for Station 2 and Aft of Station 9	58
38.	Recovered RTE Heat Shield	59
39.	Recovered RTE Heat Shield	60
40.	Recovered RTE Heat Shield	61
41.	Recovered RTE Nosetip (0° Orientation)	63
42.	Recovered RTE Nosetip (90° Orientation)	64
43.	Recovered RTE Nosetip (180° Orientation)	65

Figure		Page
44.	Recovered RTE Nosetip (270° Orientation)	66
45.	Comparison of Preflight and Postflight Nosetip	67
46.	RTE Recovered Nosetip Showing Longitudinal Groove Patterns	68
47.	Preflight and Postflight Nosetip Profiles	68
48.	Stagnation Point Pressure and Cold Wall Heat Transfer	69
49.	Laminar and Turbulent Cold Wall Heat Flux (0.75 Inch Downstream of Stagnation Point)	69
50.	Calculated Nosetip Surface Profiles for Fully Turbulent Flow	70
51.	Calculated Nosetip Surface Profile for Case of Laminar Flow to the Tangency Point and Turbulent Flow Aft of the Tangency Point	70
52.	Calculated Nosetip Surface Profile for Case of Delayed Boundary Layer Transition (Transition from Fully Laminar to Fully Turbulent Flow at T=11 Seconds From Launch)	71
53.	Temperature Distribution Along Nosetip Centerline for Fully Turbulent Flow	71
54.	Temperature Distribution Along Nosetip Centerline for Case of Laminar Flow to the Tangency Point and Turbulent Flow Aft of the Tangency Point	72
55.	Temperature Distribution Along Nosetip Centerline for Delayed Boundary Layer Transition (Transition from Fully Laminar to Fully Turbulent Flow at T=11 Seconds From Launch)	72
56.	RTE Nosetip Temperature Profile	74
57.	RTE Nosetip Stress Profile	74
58.	RTE Nosetip Strain Profile	75/76

TABLES

Table		Page
I.	Flight Vehicle Physical Properties	26
II.	Nominal RTE TWCP Heat Shield Wrap Properties	27
III.	RTE Instrumentation (Payload)	29
IV.	Summary of RTE and RTE Subsystems Environmental and Qualification Testing	31
V.	RTE Trajectory Maximum Conditions	35
VI.	RTE Separation Conditions	35

SUMMARY AND CONCLUSIONS

The roll torque evaluation (RTE) vehicle was successfully flight-tested on May 7, 1974, at the Sandia Laboratories Tonopah Test Range (TTR). The purpose of the program was to evaluate, in a realistic environment which approximates the latter portion of full-scale reentry, the roll-torque-producing effect of a tape-wrapped carbon phenolic (TWCP) heat shield. Roll torque from extraneous sources was minimized by exercising stringent control over the thermal shield construction and the reentry vehicle mass properties. Flight data and analyses indicate that all program and flight test objectives were accomplished.

The payload was delivered to nominal separation conditions of Mach 8.8, velocity of 9710 ft/s, and altitude of 10,525 feet mean sea level (MSL) by a Talos-Terrier-Recruit (TATER) rocket booster. An initial rolling velocity of -62 rad/s was also achieved by introducing fin cant on the second-stage booster fins. Throughout boosted flight, the rocket exhibited good flight stability and small angle of attack. Smooth and relatively undisturbed payload separation was accomplished by a specially designed system which produced small angular disturbances (less than 3 degrees). The utility of the TATER system was increased through the development of the payload separation system. In addition, the capability to perform these types of experiments with the flight system was demonstrated. Thus a highly instrumented reentry vehicle configuration with proven aerodynamic, thermal, and structural capabilities and with the ability for recovery has been developed.

Thermodynamic instrumentation, which included thermocouples imbedded at depths of 0.020, 0.040, and 0.100 inch from the heat shield outer surface, monitored the temperature profile through the shield, as well as the progress of surface recession due to ablation. At payload separation at least 0.040 inch of recession had occurred; this is more than enough to expose the roll-producing aerodynamic surfaces at the tape lap joints which are characteristic of TWCP shields. The flight thermal response is in good agreement with theoretical calculations.

Significant roll torque was observed from payload separation to deployment of the recovery parachute. The initial spin rate of -62 rad/s decreased to approximately -30 rad/s during this time. Onboard instrumentation permitted the reduction of the spin rate history to aerodynamic

rolling moment coefficients. At the peak Mach number (8.8), a heat shield roll moment coefficient C_{ℓ_0} of 0.44×10^{-5} was calculated. The C_{ℓ_0} increased significantly with lower Mach numbers ($C_{\ell_0} = 7.5 \times 10^{-5}$ at Mach 2.0). Comparisons are made with preflight theoretical predictions in the body of the report. Predictions based on LMSC, Kaman, and Sandia estimates show favorable agreement with flight test data.

The reentry vehicle was recovered intact. Postflight inspection of the physical appearance of the heat shield did not provide any conclusive evidence concerning the tape joints. There was no consistent surface irregularity that could be observed. Tape laps, holes, and exposed threads were all present to some extent.

The recovered RTE ATJ-S graphite nosetip revealed a turbulent flow type of erosion pattern with excessive shoulder erosion, which took place in a region from about 30 degrees to 60 degrees from the stagnation point. Approximately 0.30 inch of stagnation point ablation was measured, while sidewall ablation was less than 0.005 inch at the base of the nosetip (two inches aft of the stagnation point).

Aerodynamic analysis of the flight data indicated that the vehicle demonstrated good static and dynamic stability. The spin rate passed through a momentary condition of roll resonance sometime after payload separation. At this time the total angle of attack diverged to approximately 1.8 degrees but subsequently damped after the resonance condition. A trim angle of attack of 0.20 degree was experienced. In addition, the vehicle exhibited 20 percent more drag than anticipated, while the static stability was lower throughout the flight. A forward movement of the center of pressure by 1 to 2 percent at Mach numbers of 3 and 8 and as much as a 3 percent forward movement at Mach 6 were determined. The trim angle, higher drag, and lower static stability may all be attributed to the nosetip erosion pattern.

ROLL TORQUE EVALUATION (RTE) VEHICLE POSTFLIGHT TEST REPORT

Introduction

Flight tests of full-scale reentry vehicles with tape-wrapped carbon phenolic heat shields (TWCPs) have, on many occasions, shown large excursions in spin rate.[1,2] These anomalous roll rate variations include spin through zero and the attainment of roll resonance, both of which can degrade system performance. Spin through zero can produce considerable impact dispersion,[3] while steady-roll resonance can result in excessive aerodynamic loading, as well as dispersion.[4,5] The cause of these spin rate excursions has been the subject of intensive study. Ablation-induced phenomena have been given extensive treatment in the literature.[6,7,8] These studies have postulated a mechanism for producing surface irregularities due to the aerodynamic flow pattern, which in turn leads to significant rolling moments. Observations made in ground test facilities have substantiated the development of patterns (including streamwise vortex grooving, turbulent wedge erosion, and cross-hatching) on conical wind tunnel models made of camphor and naphthalene.

It has been determined, however, that another source of rolling moments is dependent on the material of which the thermal shield is constructed, rather than on the aerodynamic flow pattern. Analysis of flight test data suggests a strong correlation between the direction of wrap on TWCP heat shields and the vehicle spin rate performance. Seams or tape edges produced in the manufacture of the shield tape wrap material have been postulated as a source of roll torque. These edges typically become exposed at or near boundary layer transition for reentry trajectories (or at the onset of significant aerodynamic heating and ablation) and, once exposed, act as small aerodynamic surfaces which produce significant roll torques and spin excursions. Thus the ablation pattern and resulting roll torques on these types of shields depend on the surface recession only and not on the existence of a particular aerodynamic flow pattern. Based on this line of reasoning (the assumption that a step or "finlet" develops at each tape lap), several analytical models explaining observed flight performance have been formulated.[2,9,10,11]

Although there is an abundance of theoretical work on this phenomenon, the problem facing the analyst is that good quantitative verification has been, to date, quite difficult. The application of these models to existing flight test data has been to some extent limited because of uncertainties in manufacturing process control on the vehicle tested, data acquisition, and alternate flight test objectives. Furthermore, in most cases it has not been possible to separate the roll torques that are purely heat-shield-induced from those caused by other sources, such as trim-CG offset effects. In ground test facilities (wind tunnels), it is not possible to simulate a realistic flight environment (that is, one severe enough to produce ablation on the heat shield of interest while providing the proper Mach and Reynolds numbers) and measure aerodynamic rolling moments. Additionally, it is important that conditions of mass blowing be simulated.

A further complication in formulating analytic models is that, since heat shields have not been recovered intact, the character of the exposed aerodynamic surface is not known and remains a modeling uncertainty.

Since TWCP heat shields possess excellent thermo-structural properties at relatively low cost, they have been widely used in reentry system application. However, owing to the ablation-induced roll torque phenomenon, system performance can be, and has been, severely degraded. It is important, therefore, that a theoretical understanding of this mechanism and its effect on flight performance be obtained and verified. The important parameters can then be identified, and some insight can be provided to obtain a more predictable (controllable) performance through shield construction, process control, etc.

The roll torque evaluation (RTE) program, initiated in November 1973, was designed to obtain accurate rolling moment data on an ablating TWCP heat shield in flight. The heat shield was manufactured under stringent process control to eliminate wrap uncertainties, and the test vehicle was designed with a large static margin and close mass properties control to minimize extraneous roll torques.

The Sandia Talos-Terrier-Recruit (TATER)[12] rocket was chosen as the boost system, since it provides flight conditions severe enough to produce considerable aerothermodynamic ablation. The vehicle performance was therefore observed under conditions closely simulating reentry, and roll torques were measured under blowing conditions.

The flight test took place on May 9, 1974, at the Sandia Laboratories Tonopah Test Range (TTR). All major test and program objectives were accomplished. Booster performance was nominal, as was payload separation. Sufficient ablation took place to expose the torque-producing surfaces, and the rolling history was observed, along with the flight motion and aerothermodynamic response. The payload was recovered intact by means of a

parachute recovery system. This report presents a complete description of the program and flight system, along with an analysis of the flight data. The flight data and analysis are also supplemented extensively with theoretical calculations in order to provide a more complete presentation.

RTE Program Objectives

The purpose of the roll torque evaluation (RTE) program was to obtain an understanding of the nature of ablation-induced surface irregularities on tape-wrapped carbon phenolic (TWCP) heat shields on reentry vehicles and their associated effect on aerodynamic rolling moments and spin rate. To accomplish this, a flight test was conceived in which a reentry vehicle (manufactured under stringent process control) would be flown in an environment severe enough to produce surface ablation of sufficient order to expose the aerodynamic surface irregularities. Spin rate of the reentry vehicle was measured in free flight, while the adverse effects of trim-CG induced roll torques were mitigated by mass properties control and a large static margin (about 15 percent). Such an approach reduces measurement uncertainty. The design was evaluated in terms of the following program and flight test objectives:

1. Determine the vehicle spin rate change and rolling moment coefficient caused by the ablated TWCP surface irregularities in a flight environment closely simulating reentry conditions.

2. Determine heat shield surface recession and degree of tape lap exposure, and correlate with the roll torque experienced.

3. Recover the reentry vehicle for postflight investigation to ascertain the nature of the surface irregularities and to conduct postflight ground testing, if warranted.

4. Demonstrate the utility of the TATER system for free-flight reentry vehicle dynamics experiments while developing a capability for payload/booster separation.

RTE Flight System Description

Booster

The booster employed for the RTE flight experiment was the TATER rocket system shown in Figures 1 and 2. This system consists of a Talos first stage, a Terrier second stage, and a Recruit third stage. Designed to achieve high velocities at low altitudes, the boost system was developed by Sandia Laboratories, Albuquerque, in support of the SAMS (Sandia ABRES Materials Study) program.[12]

The complete system was first successfully flown in August 1973. It attained nominal burnout conditions of 11,000 ft/s velocity at about 11 kft altitude mean sea level. For the RTE flight test, the rocket motors were separated by aerodynamic drag, and the payload was deployed from the third-stage adapter by a specially designed separation system (to be described later).

Flight Vehicle*

A schematic of the flight vehicle is given in Figure 3, and a description of the physical properties is provided in Table I. The test vehicle was a 7-degree half-angle cone with a 9.5-inch base diameter, a 1.06-inch nose radius (bluntness ratio of 0.223), and a total weight of 86 pounds. In order to minimize the effects of extraneous roll torques (from a combination of trim angle and center-of-mass offset) the vehicle was designed to have a 14 percent static margin (to reduce trim angle) while the CG offset was held to less than 0.001 inch by careful balancing. The details of the flight vehicle design are shown in Figure 4.

The nosetip is a standard plug type constructed of Union Carbide ATJ-S graphite. These tips are fabricated for reentry testing by Sandia and typically follow a nondestructive evaluation and annealing program which minimizes flaw content and maximizes uniformity. The RTE flight and backup nosetip followed such a procedure, as outlined in Reference 13. In the assembly, after the tip has been properly aligned in the test unit, it is bonded to the heat shield-substructure using a high-temperature bond (in this case Epon 934®). The nut threaded to the nosetip material is not an alignment feature but serves as a capturing device to ensure that the nosetip will not slip off during parachute deployment in the event of a bond failure.

*The payload was designed by B. D. Pontsler, Division 8165.

®Registered trademark of Shell Chemical Co., New York.

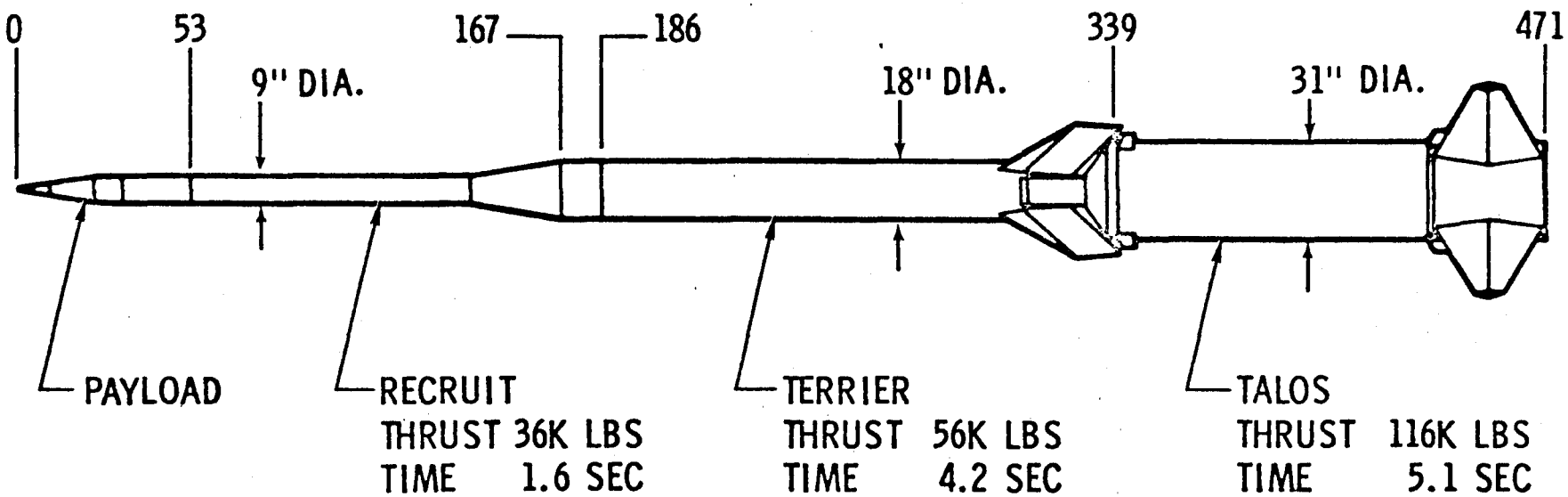

Figure 1. TATER Booster Schematic

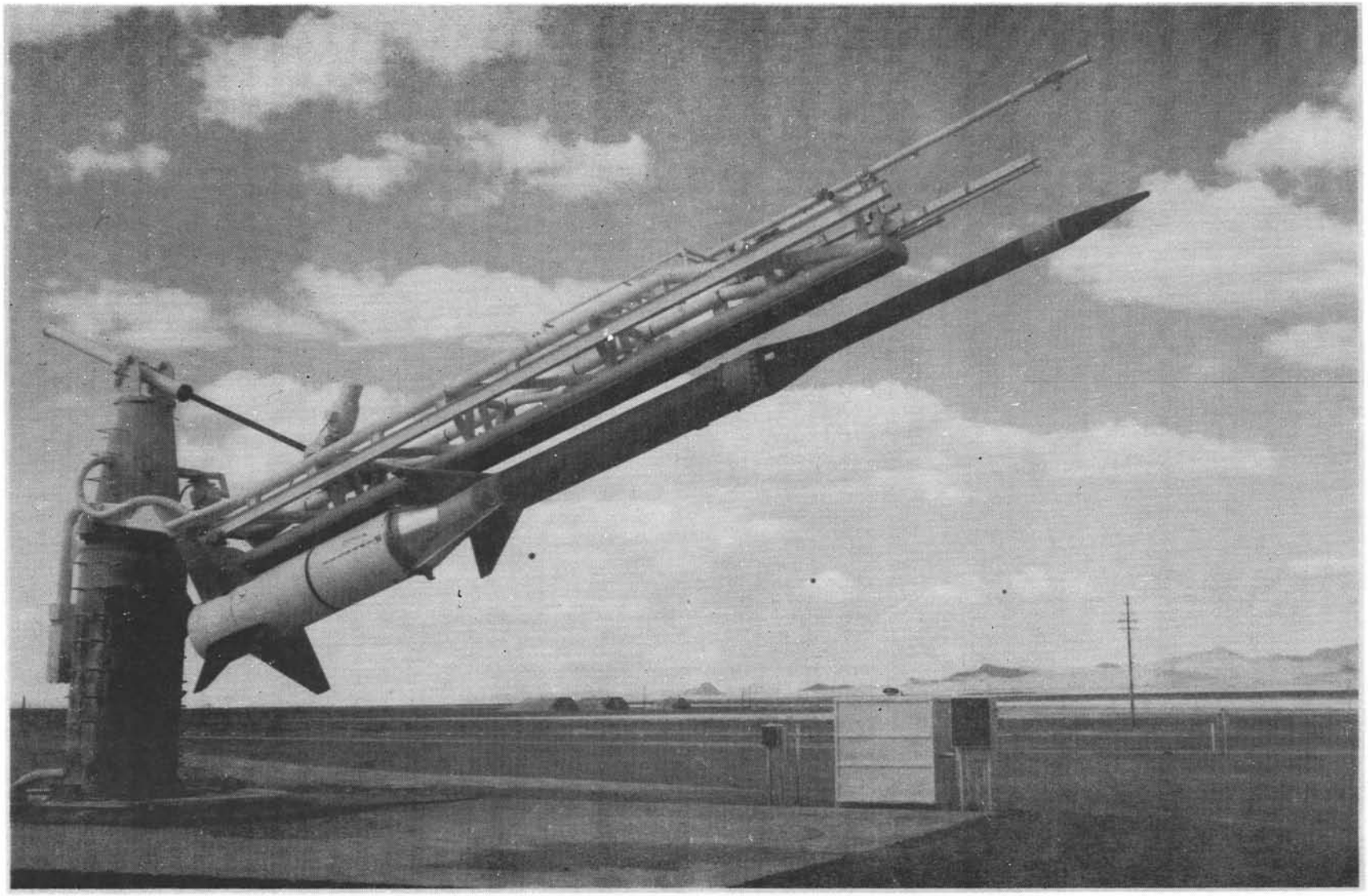

Figure 2. RTE/Booster Flight System

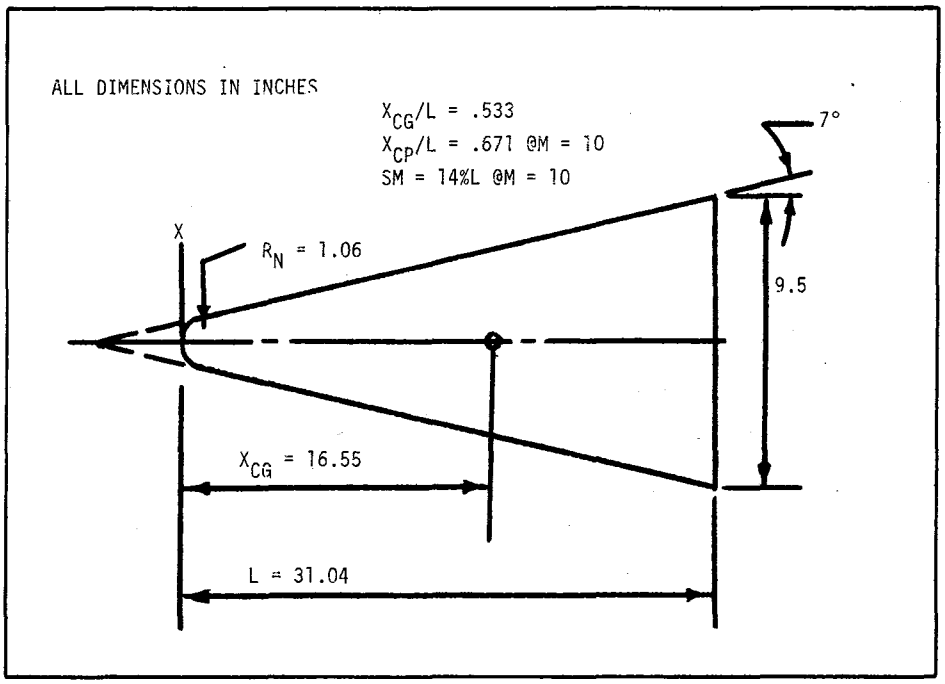

Figure 3. Roll Torque Evaluation Vehicle Schematic

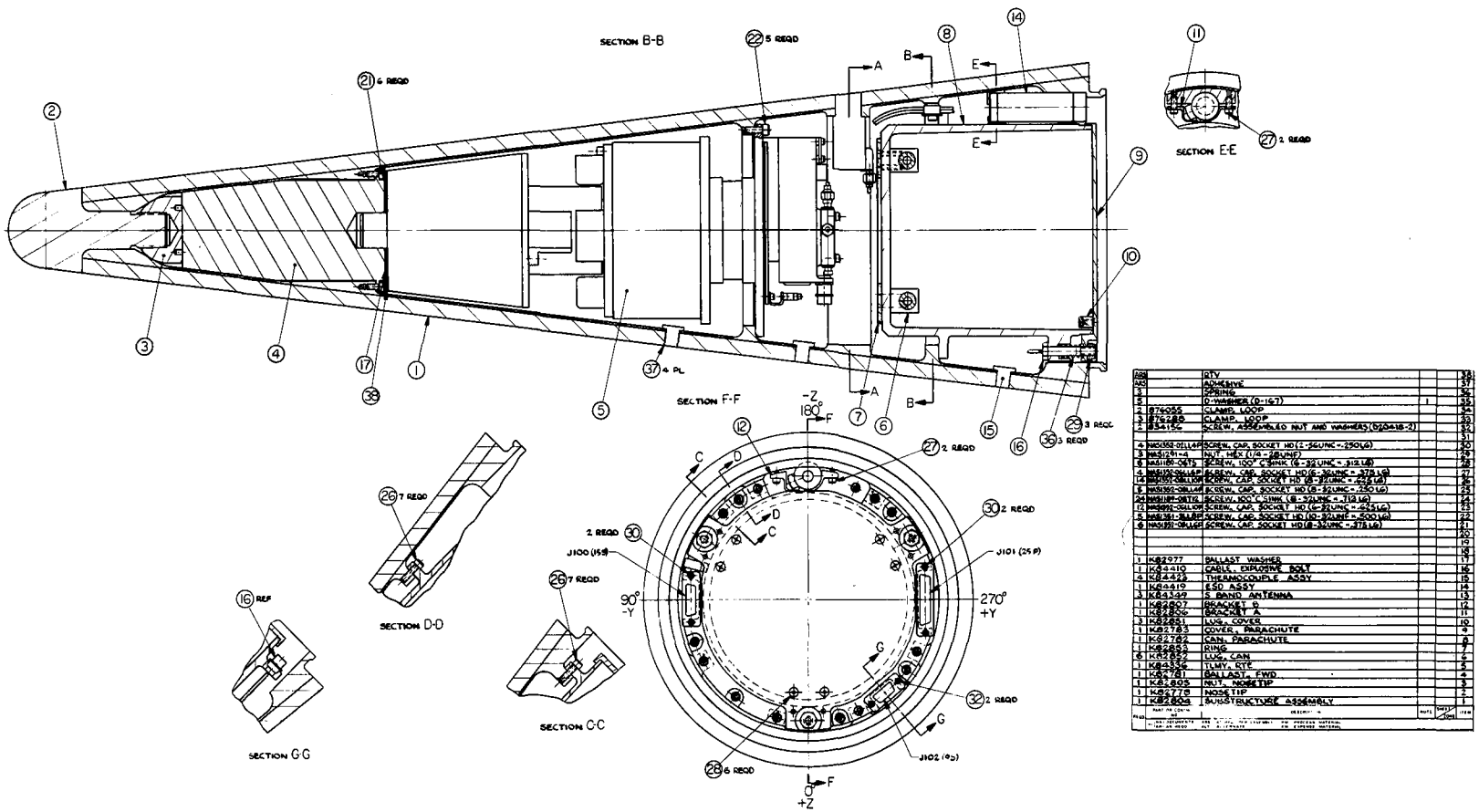

ASG		RTV			38
ASG		ADHESIVE			37
3		SPRING			36
5		O-WASHER (O-167)	1		35
2	876055	CLAMP, LOOP			34
3	876280	CLAMP, LOOP			33
2	834156	SCREW, ASSEMBLED NUT AND WASHERS (D2D4418-2)			32
					31
4	NAS1352-08LL4P	SCREW, CAP, SOCKET HD (1/2-56UNC-.250LG)			30
3	NAS1291-4	NUT, HEX (1/4-28UNF)			29
8	NAS1189-06T5	SCREW, 100° C'SINK (6-32UNC-.312 LG)			28
4	NAS1352-06LL6P	SCREW, CAP, SOCKET HD (6-32UNC-.375 LG)			27
14	NAS1352-06LL10P	SCREW, CAP, SOCKET HD (6-32UNC-.625 LG)			26
3	NAS1352-08LL4P	SCREW, CAP, SOCKET HD (8-32UNC-.250 LG)			25
24	NAS1189-08T12	SCREW, 100° C'SINK (8-32UNC-.750 LG)			24
12	NAS1352-08LL10P	SCREW, CAP, SOCKET HD (8-32UNC-.625 LG)			23
5	NAS1351-8LL8P	SCREW, CAP, SOCKET HD (10-32UNF-.500 LG)			22
6	NAS1351-8LL6P	SCREW, CAP, SOCKET HD (10-32UNF-.375 LG)			21
					20
					19
					18
1	K82977	BALLAST WASHER			17
1	K84410	CABLE, EXPLOSIVE BOLT			16
4	K84423	THERMOCOUPLE ASSY			15
1	K84419	ESD ASSY			14
3	K84347	S BAND ANTENNA			13
1	K82807	BRACKET B			12
1	K82806	BRACKET A			11
3	K82851	LUG, COVER			10
1	K82783	COVER, PARACHUTE			9
1	K82782	CAN, PARACHUTE			8
1	K82853	RING			7
6	K82852	LUG, CAN			6
1	K84336	TUBE, STE			5
1	K84781	BALLAST, FWD			4
1	K82805	NUT, NOSETIP			3
1	K82778	NOSETIP			2
1	K82804	SUBSTRUCTURE ASSEMBLY			1
PART OR COMP NO		DESCRIPTION		NOTE	SHEET ITEM

Figure 4a. RTE Vehicle Assembly

NOTES:

1. ITEMS NOT SHOWN ARE 15, 16, 34, 35 AND 39.
2. REMOVE THESE BOLTS AFTER SPRINGS HAVE BEEN COMPRESSED BETWEEN NOSE ASSY. AND SPRING HOUSING (ITEM 9).
3. NOSE ASSEMBLY SUPPLIED BY ORG 8168.
4. MOTORS AND RELATED HARDWARE USED WITH THIS PAYLOAD ARE SAME AS USED ON TATER TEST VEHICLE (DWG T21048).
5. FOR INSULATION INFORMATION (DE 350) SEE DWG T25717.
6. THIS ITEM HAS BEEN ROTATED INTO SECTION.

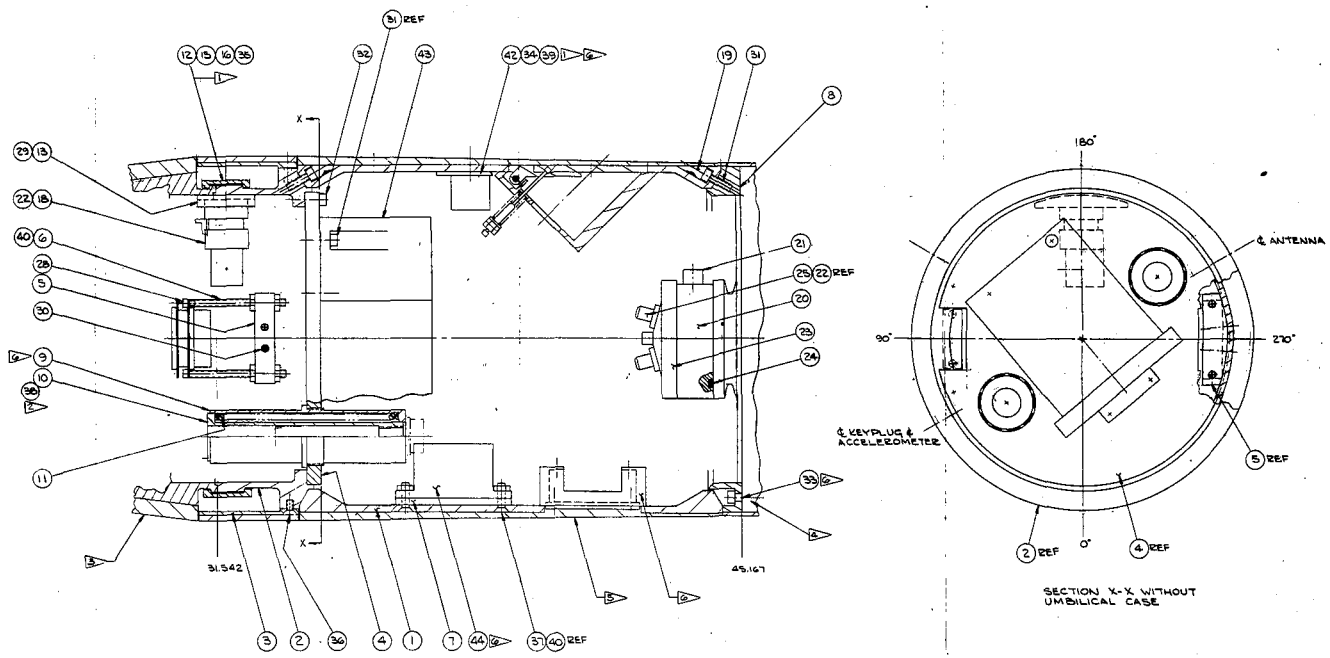

1		ACCELEROMETER			44
1		TRANSPONDER			43
3		ANTENNA			42
					41
10	MS35650-302	NUT 10-32			40
12	MS35649-262	NUT 6-32			39
2		BOLT, HEX. HD. STEEL 1/2-13 x 3 1/2			38
2	MS35191-274	SCREW, MACH. FLAT 82° 10-32 x 3/4			37

LIST OF MATERIAL

8	MS35191-210	SCREW, MACH. FLAT 82°, 10-32 x 3/8			36
2	MS35190-291	" " " 82°, 8-32 x 5/8			35
12	MS35190-238	" " " 82°, 6-32 x 1/2			34
24	MS16998-41	SCREW, SOC. HD CAP 1/4-28 x 1/2			33
8	MS16998-29	" " " 10-32 x 3/4			32
52	MS16998-28	" " " 10-32 x 3/8			31
4	MS16998-27	" " " 10-32 x 1/2			30
2	MS16998-26	" " " 10-32 x 3/8			29
4	MS16997-9	" " " 4-40 x 1/4			28
					27
					26
2	MS28775-6	O-RING			25
2	MS9021-226	O-RING			24
1		IGNITER ASSY (THIOKOL TE-P-372-4)			23
3		TC 26 INITIATOR			22
1	T17358-000	CONNECTOR, MODIFIED			21
1	T17358-000	ADAPTER, PRESSURE			20
48	T10160-000	INSULATOR, SCREW			19
1	SN7012-2C	SEPARATION NUT HI-SHEAR			18
					17
1	T12168-001	RETAINER ASSY			16

LIST OF MATERIAL

1	P73926-001	PIN ASSY			15
					14
1	P69384-000	NUT, MOUNTING PLATE			13
1	T22291-000	V-BAND			12
2	T26722-000	SPRING			11
2	T25709-000	SLEEVE, SPRING			10
2	T25713-000	HOUSING, SPRING			9
1	T21068-000	RING, ADAPTER			8
1	T25721-000	SPACER, ACCELEROMETER			7
4	T25720-000	ROD			6
2	T25719-000	CONNECTOR BRACKET			5
1	T25718-000	PLATE			4
1	T25714-000	SHROUD			3
1	T26704-000	SEPARATION ADAPTER			2
1	T25703-000	UMBILICAL CASE ASSY			1

LIST OF MATERIAL

Figure 4b. RTE Payload Adapter and Separation System

TABLE I

FLIGHT VEHICLE PHYSICAL PROPERTIES

Cone Half Angle, θ_c	7°
Bluntness Ratio, η	0.223
Nose Radius, R_N	1.06 in.
Base Diameter, D_B	9.5 in.
Vehicle Actual Length, L	31.04 in.
Weight, W	89.74 lb
Center-of-Gravity Distance, X_{CG} From Nose (54% of Length)	16.783 in.
Pitch Moment of Inertia, I_Y	1.3989 slug-ft^2
Yaw Moment of Inertia, I_Z	1.3978 slug-ft^2
Roll Moment of Inertia, I_X	0.1019 slug-ft^2
Static Margin (at M = 10)	13% of length
Radial CG Offset	<0.001 in.

The heat shield was constructed of tape-wrapped carbon* phenolic (TWCP) with a nominal thickness of 0.400 inch. A description of the TWCP manufacturing process is given in Appendix A. Table II lists the carbon phenolic tape and wrap properties. A nominal 0.025-inch Epon 934 bond was used to bond the heat shield to a 0.050-inch stainless steel substructure. A positive wrap** was employed over the aft 21.5 inches of the heat shield while the forward 7.44 inches had a neutral wrap. A neutral wrap is accomplished by alternating positive and negative wraps in zones of approximately 2 inches in length. With this fabrication process, the total heat shield will produce a positive roll torque that will cause the spin rate to increase in the positive direction.

*CCA-2[1641]-10 Carbon Cloth. The RTE heat shield was fabricated by Hitco.

**A positive wrap is defined as one which, because of the alignment of the tape lap surfaces, produces a roll torque on the vehicle which is in a clockwise direction when viewed from the rear.

TABLE II

NOMINAL RTE TWCP HEAT SHIELD WRAP PROPERTIES

Length Between Laps, L_S	44 in.
Bias Angle, ψ_S	45 deg
Initial Tape Thickness, T	0.020 in.
Layup Angle	20 deg
Tape Width	2 in.
Heat Shield Thickness	0.040 in.

A parachute recovery system* was included and packaged in the aft end of the flight vehicle. The recovery system consisted of a 2-foot-diameter pilot parachute and a 7-foot-diameter main parachute. This combination of parachutes was the largest that could be packaged in the volume available. Initial deployment was nominally set at 45 seconds after launch. Impact velocity did not exceed 50 ft/s.

Payload Adapter and Separation System**

The payload adapter and separation system design is shown in Figure 4b. With this design, the flight vehicle is held to the missile adapter system by a spring clamp, which in turn is locked in place with a bolt through a serrated plate and attached to an explosive nut. Separation of the payload from the missile is initiated by the explosive separation nut. Destruction of the nut allows the clamp to spring free from the payload flange. Two coil springs attached to the adapter provide the necessary axial force for clearing the payload from the missile adapter. Ground and flight test data and photo observations indicate that the system performed nominally. The concept was therefore verified for use on future testing.

*Designed by D. W. Johnson, Parachute Systems Division 1332.

**System designed by R. D. Fellerhoff, Mechanical Design Division, 1324.

Instrumentation and Telemetry

The RTE telemetry system was designed to function (1) as a data acquisition system to monitor and transmit the payload flight dynamic and thermodynamic data and (2) as a firing circuit to provide the proper timing and sequencing for the rocket motor, separation system, and parachute deployment initiators. A complete description of the telemetry and instrumentation system is presented in Appendix B and in Reference 14.

Onboard instrumentation was designed to provide a detailed evaluation of vehicle flight dynamics, the primary data being spin rate. The RTE telemetry system, which includes a tri-axis rate gyro, linear accelerometers, and thermocouple stacks, is summarized in Table III. The rate gyro and lateral accelerometers are used to provide vehicle static and dynamic stability data. Axial accelerometers provide vehicle drag and trajectory information. One of the lateral accelerometers was offset 2 inches from the vehicle centerline in order to provide a backup measurement of spin rate. The thermal stacks were designed to measure heat shield in-depth temperature profiles at different locations and to monitor the progress of heat shield surface recession due to ablation. Four thermal stacks were included in the payload, three of these along one body meridian (designated the 0-degree meridian) at axial stations which are 19.0, 22.75, and 28.5 inches from the actual nose. An additional stack is located 28.5 inches from the nose at the 180-degree meridian. Each stack provides measurements at depths of 0.020, 0.040, and 0.10 inch from the heat shield outer surface. Nominal ablation during the flight range of interest was to exceed the depths of the first two thermocouples.

Range Instrumentation and Support

The RTE system flight test took place at the Sandia Tonopah Test Range on May 9, 1974. A general description of the range facilities and operation is presented in Reference 15. Specific details and operating procedures pertaining to the RTE flight test are contained in Reference 16. Complete hazards information and safe operating procedures are given in Reference 17.

Preflight Qualification Testing

Environmental and qualification testing was performed on the payload and its subsystems. These tests were intended to qualify the payload to the

TABLE III

RTE INSTRUMENTATION (PAYLOAD)

Measurement	Range	Sampling Rate
Vehicle Dynamics		
Roll Rate	±3600 deg/s	2 kHz continuous and 60 SPS
Pitch Rate	±400 deg/s	2 kHz continuous and 60 SPS
Yaw Rate	±400 deg/s	2 kHz continuous and 60 SPS
X-Acceleration	±100 g	1 kHz continuous and 60 SPS
X-Acceleration	±50 g	1 kHz continuous and 60 SPS
Y-Acceleration	±50 g	1 kHz continuous and 60 SPS
Z-Acceleration	±50 g	1 kHz continuous and 60 SPS
Y-Acceleration (offset 2 in. from vehicle centerline)	±40 g	1 kHz continuous and 60 SPS
X-Acceleration	-75 to +125g	60 SPS
Thermodynamics		
Thermal Stacks (4) (three measurements each)	1295° to 2295°F	20 SPS
Thermocouples (4)	0°-500°F	20 SPS

expected flight environment and to perform proof tests of the system mechanical and electrical designs. The environmental testing performed on the flight vehicle is summarized in Table IV. The flight unit was successfully qualified to the levels shown. Additionally, the firing circuit and design qualification tests were performed to satisfaction.

Trajectory Analysis

General Flight Characteristics

The nominal flight trajectory sequence of events and altitude history are illustrated in Figure 5. The TATER booster system consists of a Talos first stage having a nominal burn time of 5.5 seconds, a Terrier second stage with a nominal burn time of 4.0 seconds, and a Recruit third stage with a nominal burn time of 1.5 seconds. Booster staging and separation are accomplished by aerodynamic drag.

Payload separation is accomplished through the release mechanism described in a previous section. A nominal separation acceleration of 5g between booster and payload was obtained. The separation mechanism was initiated after a delay of 0.65 second after a 20-g deceleration was sensed. This delay is to ensure that payload release will not take place until after the third stage is completely burned and no residual thrust is present.

Approximately 45 seconds after launch (33 seconds after payload separation), a 2-foot diameter pilot parachute was deployed. This was followed at t=55 seconds by a 7-foot-diameter main parachute.

The boost-phase trajectory[18] was computed with the Air Force 6DOF trajectory program. A desired payload separation spin rate of -50 rad/s (negative spin rate is counterclockwise when viewed from the rear) was to be obtained by introducing a fin cant on the first- and second-stage boosters. During second-stage burn a brief roll resonance was experienced. However, this is not significant because of the rapid passage of the spin rate through the natural pitch frequency.

The ballistic computations and impact dispersions are summarized in Appendix C.

TABLE IV

SUMMARY OF RTE AND RTE SUBSYSTEMS ENVIRONMENTAL AND QUALIFICATION TESTING

Environmental Tests

1. Resonance Survey: 0.5 g from 20 to 2000 Hz, sweep rate of 1 octave/minute, in longitudinal axis and lateral axis
2. Vibration: 0.03 g^2/Hz, 20 to 2000 Hz for 30 seconds in longitudinal and lateral axis
3. Acceleration: +100, -60 g along longitudinal axis
   ± 30 g along lateral axis

Qualification Tests

1. Parachute Cover: Fire explosive bolts (Holex 2504) releasing spring-loaded cover and observe deployment.
2. Separation Test: Fire the TC26 separation system initiator releasing the separation ring and observe deployment.
3. ESD Test: Observe acceleration level of ESD closure.
4. Full Firing Circuit Test: Perform a complete firing circuit test in which all initiators (Terrier motor, Recruit motor, separation system, parachute cover) are fired in sequence.

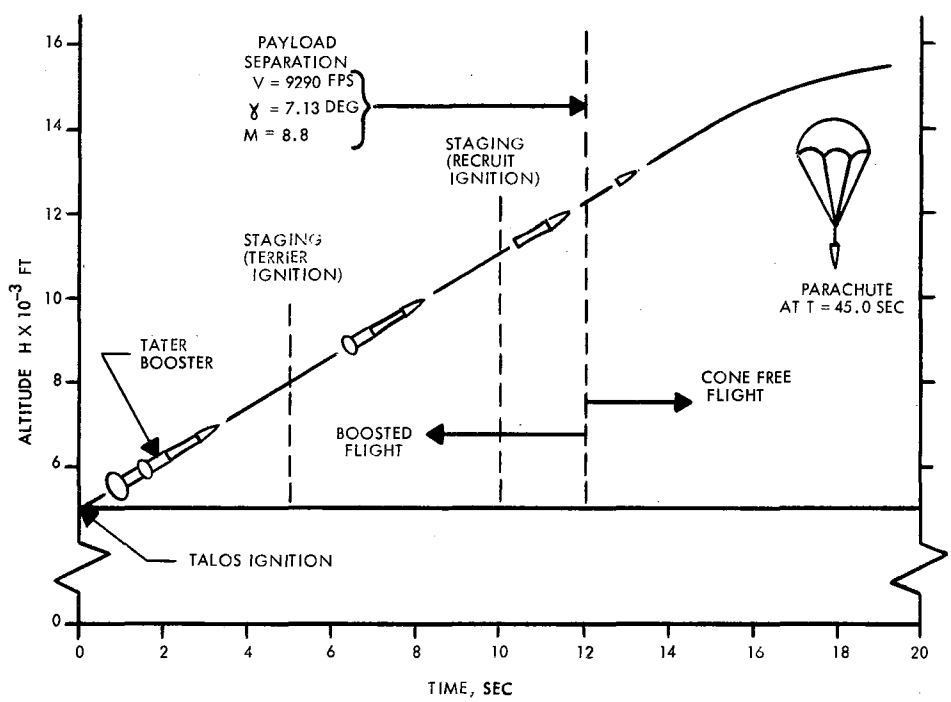

Figure 5. RTE Trajectory Events

Flight Trajectory Data

The flight vehicle trajectory is reconstructed from the ground-based radar and the payload telemetry data. These data, in conjunction with trajectory simulations, are used in establishing the payload separation conditions, as well as the time history of the trajectory performance variables. The radar-measured position and velocity are used primarily to establish the boost phase trajectory and payload separation conditions. Since the payload presents a relatively poor target for both radar and optical ground stations, tracking was lost shortly after payload separation.

Two onboard accelerometers (aboard the payload) were used to monitor the axial acceleration history during boost and free-flight stages. Data provided by these two instruments are shown in Figures 6 and 7. These accelerations (excluding any instrument bias) may be integrated to determine the axial velocity history. Since the ±50 g accelerometer became saturated at approximately t ≈ 10 to 12 seconds, it was not used to determine the velocity history. The ±100 g instrument was used for this purpose. The axial velocity history is considered equal to the total velocity, since the angle of attack remains small for the duration of the trajectory.

The results of the trajectory reconstruction are summarized in Figure 8, which shows the altitude and velocity history determined from the 12-36 radar.[19] Only the boost phase is available, since the payload was not tracked after separation. Also shown is the velocity history obtained by an integration of the onboard acceleration given in Figure 7. Close agreement is noted. Although the data are not shown, good agreement was also obtained with the optical tracking system (ground-based photo cinetheodolites) trajectory data.[20] With this approach, the maximum environmental conditions achieved on the flight vehicle, as well as the separation conditions, were established and summarized in Tables V and VI.

Meteorological Data

Immediately prior to flight, atmospheric data were obtained by means of rawinsonde balloons released in the neighborhood of the launch area. The speed of sound and the air density obtained through this procedure[20] are presented as functions of altitude in Figures 9 and 10 and are used with post-flight trajectory simulations.

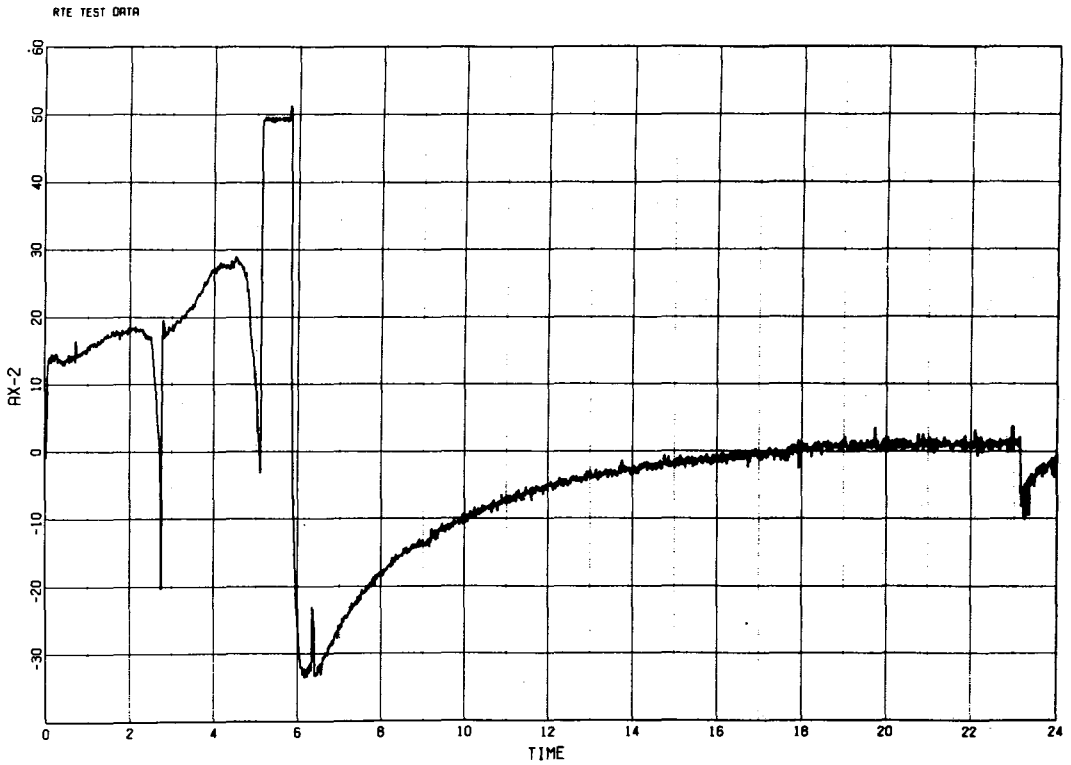

Figure 6. Payload Axial Acceleration History (±50g Accelerometer)

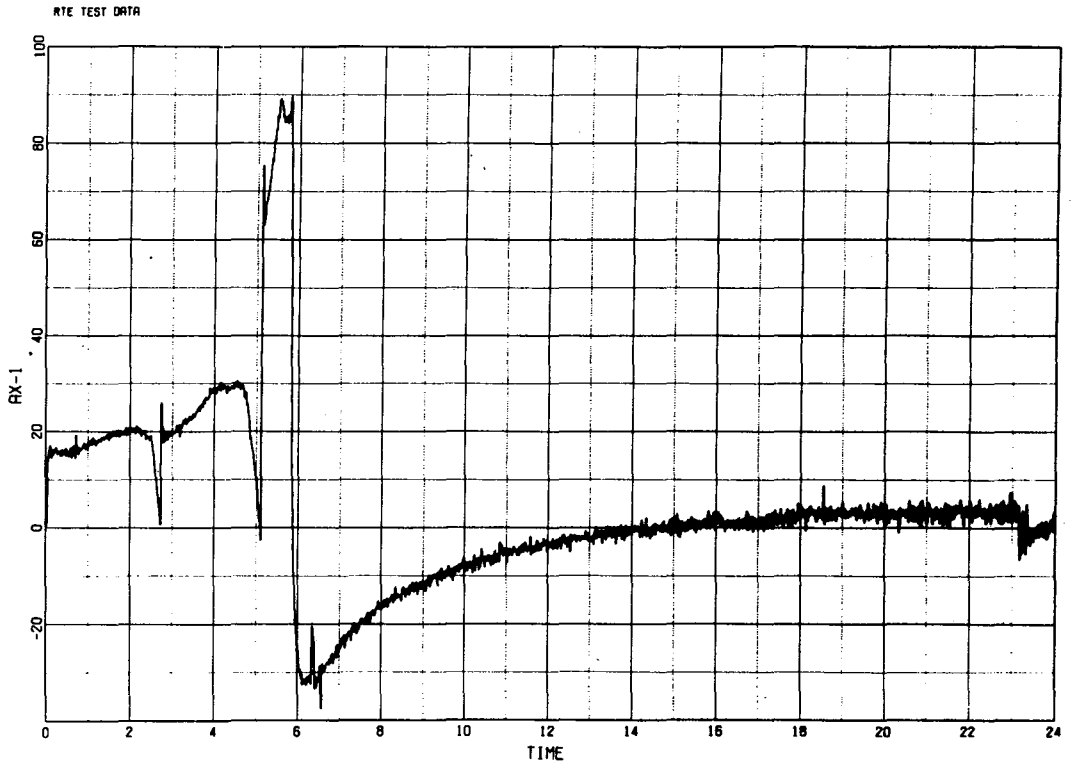

Figure 7. Payload Axial Acceleration History (±100g Accelerometer)

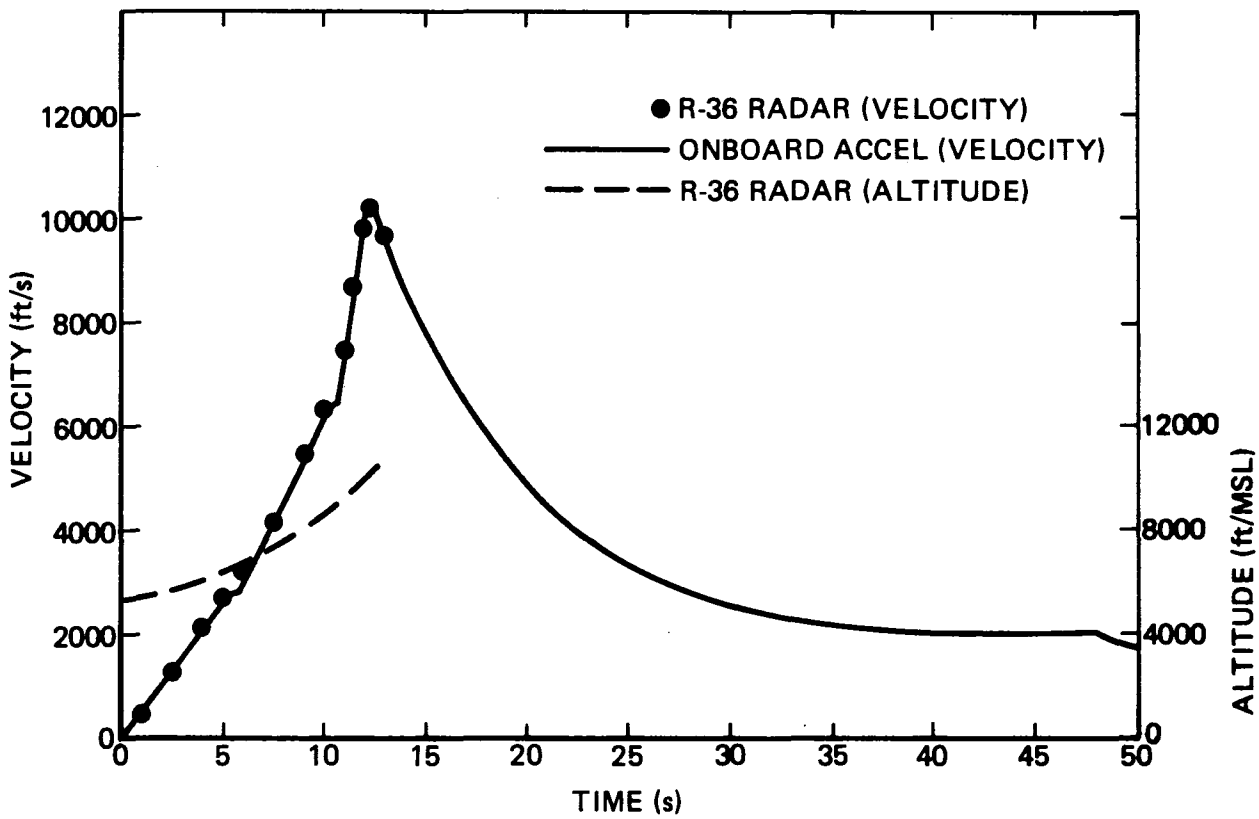

Figure 8. Comparison of Flight Velocity and Altitude History Derived from Radar and Onboard Accelerometer

TABLE V

RTE TRAJECTORY MAXIMUM CONDITIONS

Velocity	10,110 ft/s
Mach Number	9.2
Altitude (MSL)	10,050 ft
Dynamic Pressure	85,000 lb/ft^2
Nosetip Stagnation Pressure	75 atmospheres
Nosetip Stagnation Heating (cold wall)	2500 Btu/ft^2-s
Cone Surface Heating (at base)	600 Btu/ft^2-s

TABLE VI

RTE SEPARATION CONDITIONS

Velocity	9710 ft/s
Mach Number	8.8
Flight Path Angle	4.25 deg
Altitude (MSL)	10,525 ft
Dynamic Pressure	77,600 lb/ft^2
Roll Rate	-62 rad/s

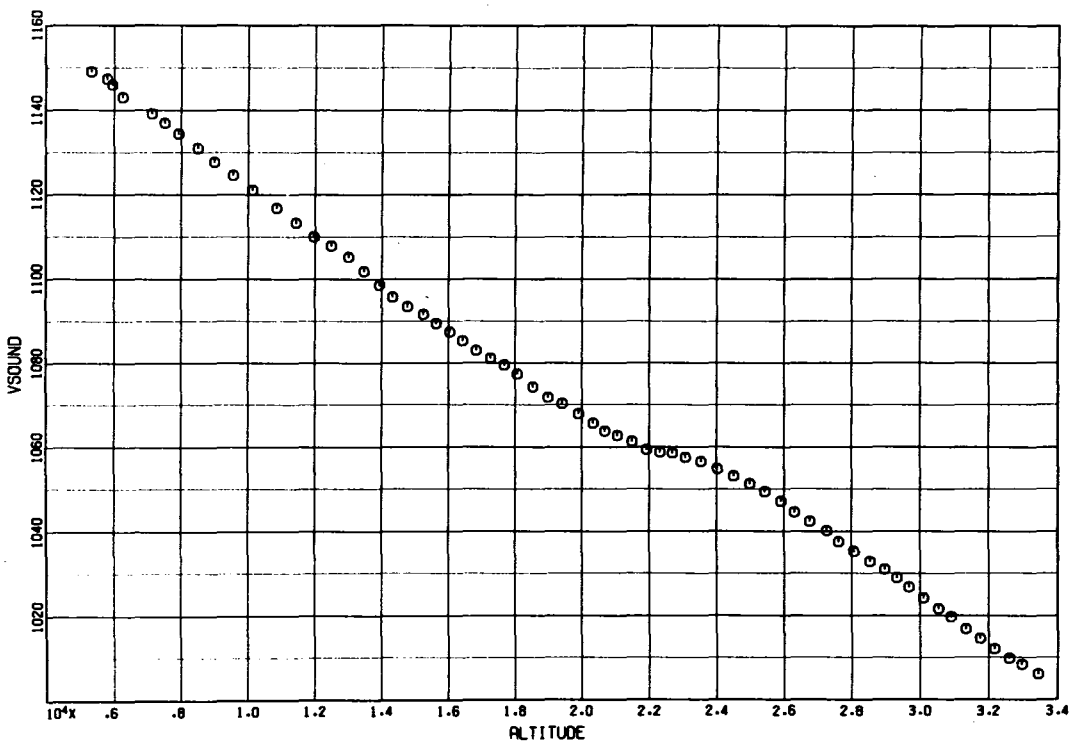

Figure 9. Observed Atmospheric Conditions--Speed of Sound Versus Altitude

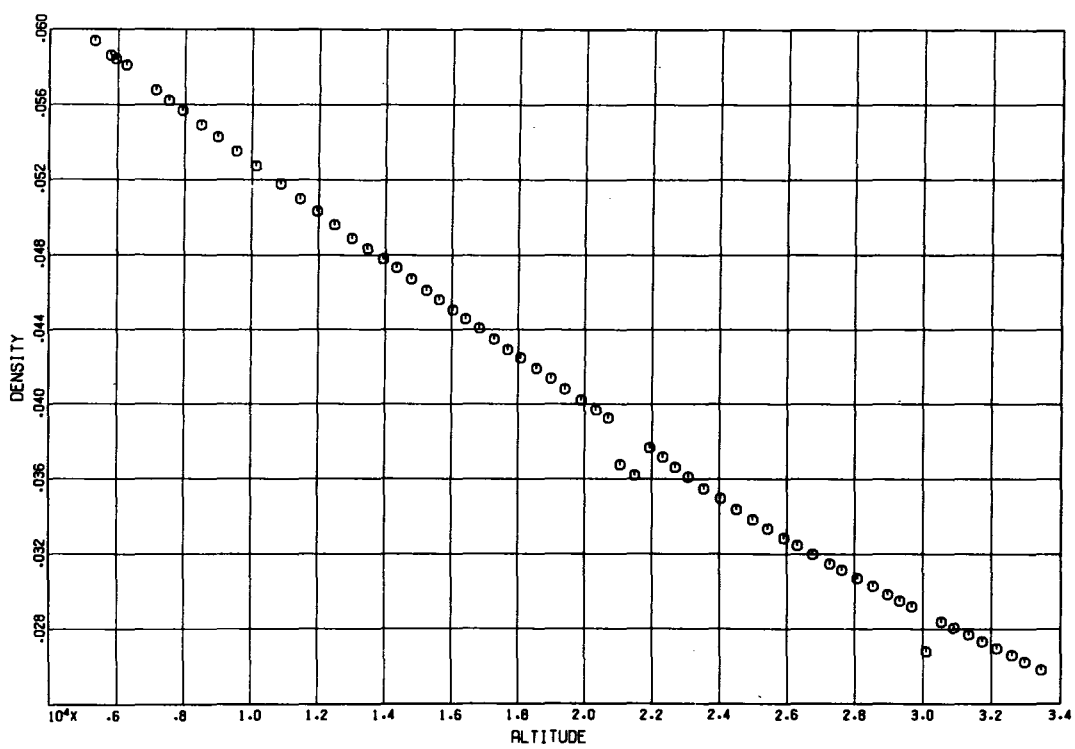

Figure 10. Observed Atmospheric Conditions--Air Density Versus Altitude

Payload Trajectory Characteristics

The payload trajectory characteristics computed with the SPINFIN trajectory simulation program[21, 22] are presented in Figures 11 through 15. These calculations, for the payload alone, were initiated at the separation conditions listed in Table VI and are shown for the period from RV separation to parachute deployment. The flight environment is noted to correspond to that experienced on a full reentry trajectory from shortly after peak dynamic pressure to impact. This environment is severe enough to produce significant nosetip and heat shield ablation, as well as aerodynamic loading.

Aerodynamic Analysis

Flight Motion Data

The RTE vehicle was instrumented to provide flight motion and dynamical data that is as complete as possible without exceeding the weight and volume constraints. This instrumentation was summarized in Table III and discussed in a previous section.

The body-fixed components of angular rate (pitch, yaw, and roll rate) obtained for the tri-axis rate gyro are presented in Figures 16, 17, and 18, respectively. Nominal pitch rates at payload separation were less than 40 deg/s, and an initial spin rate of -3550 deg/s was obtained. The initial motion exhibits good damping to T = 16 seconds. At this time a divergence to approximately 80 deg/s pitch rate and 60 deg/s yaw rate occurs. This divergence can be attributed to the passage of the spin rate through the condition of roll resonance at about T = 18 seconds. The divergence is temporary and good stability is noted subsequent to the peak angular rates as the motion damps to small rates. The spin rate begins to decrease immediately upon separation because of the roll-producing heat shield surfaces. The vehicle spins down from a peak rate of -3550 deg/s to approximately -1750 deg/s at T = 45 seconds, at which time recovery parachute deployment occurs.

Lateral acceleration histories are presented in Figures 19, 20, and 21. In order to provide a backup measurement of spin rate, each lateral accelerometer was offset from the vehicle centerline. These offsets are listed below:

	Y Offset (in.)	Z Offset (in.)
AZ-1	0	1.668
AY-1	1.628	0
AY-2	-2.0	0

The output of these instruments may be easily corrected for their offsets from the centerline. Axial acceleration histories were presented in the previous section.

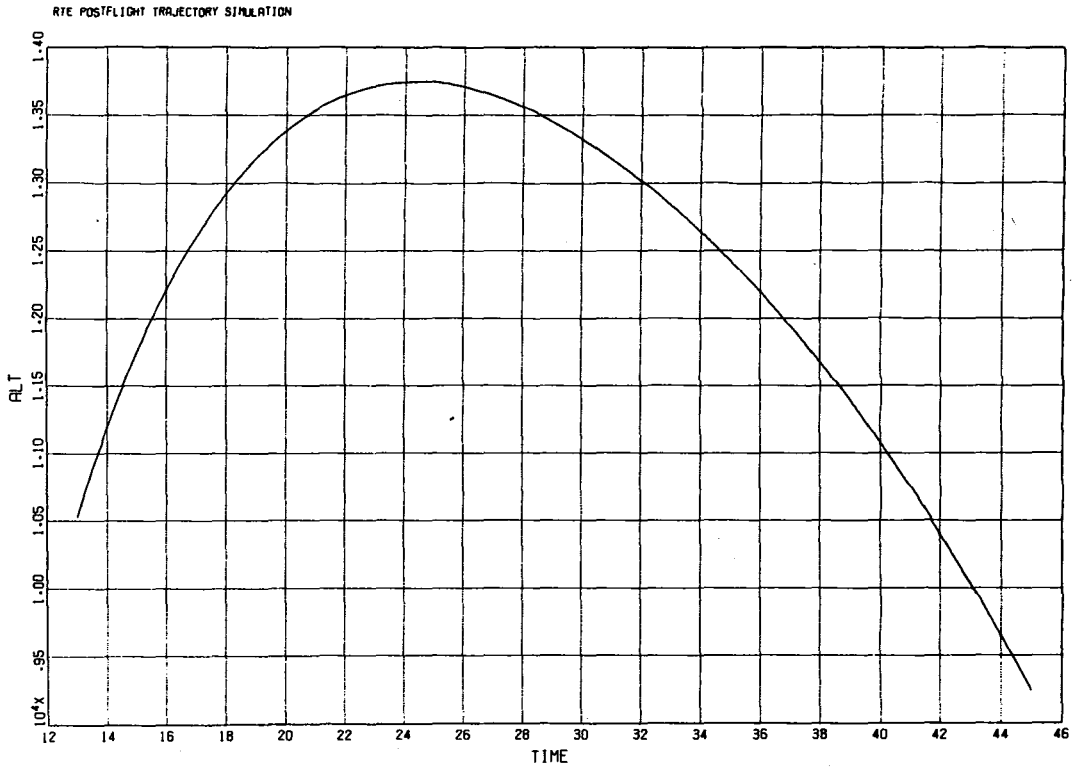

Figure 11. RTE Payload Altitude History

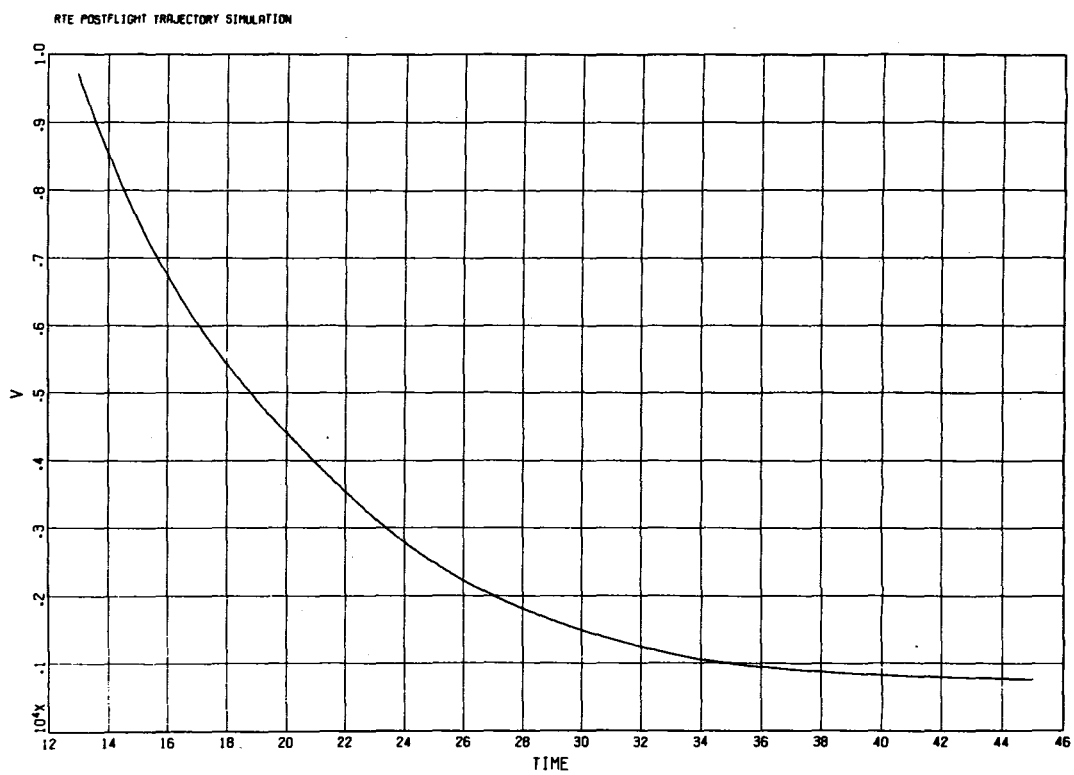

Figure 12. RTE Payload Velocity History

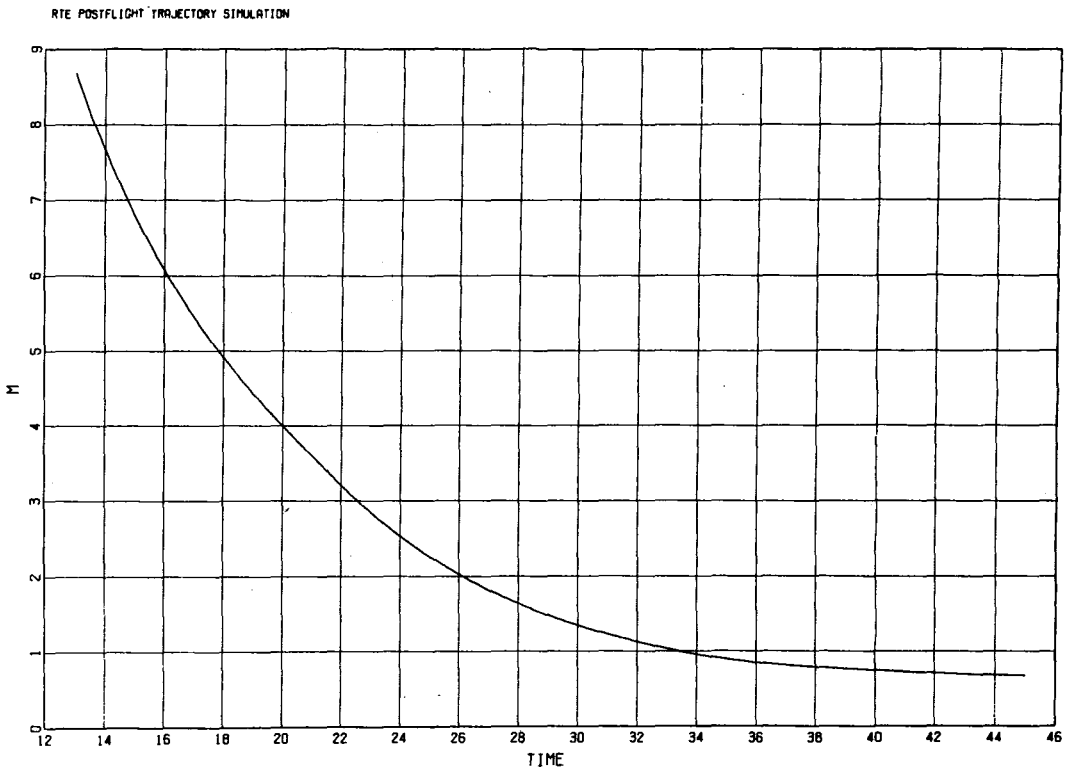

Figure 13. RTE Payload Mach Number History

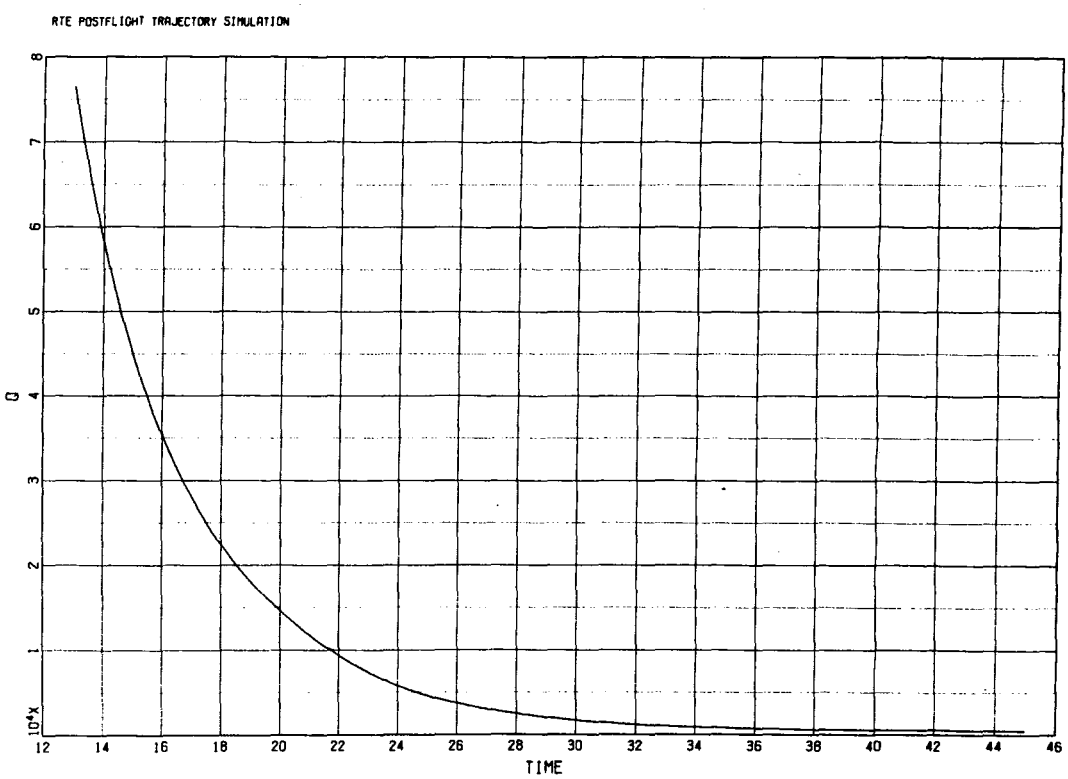

Figure 14. RTE Payload Dynamic Pressure History

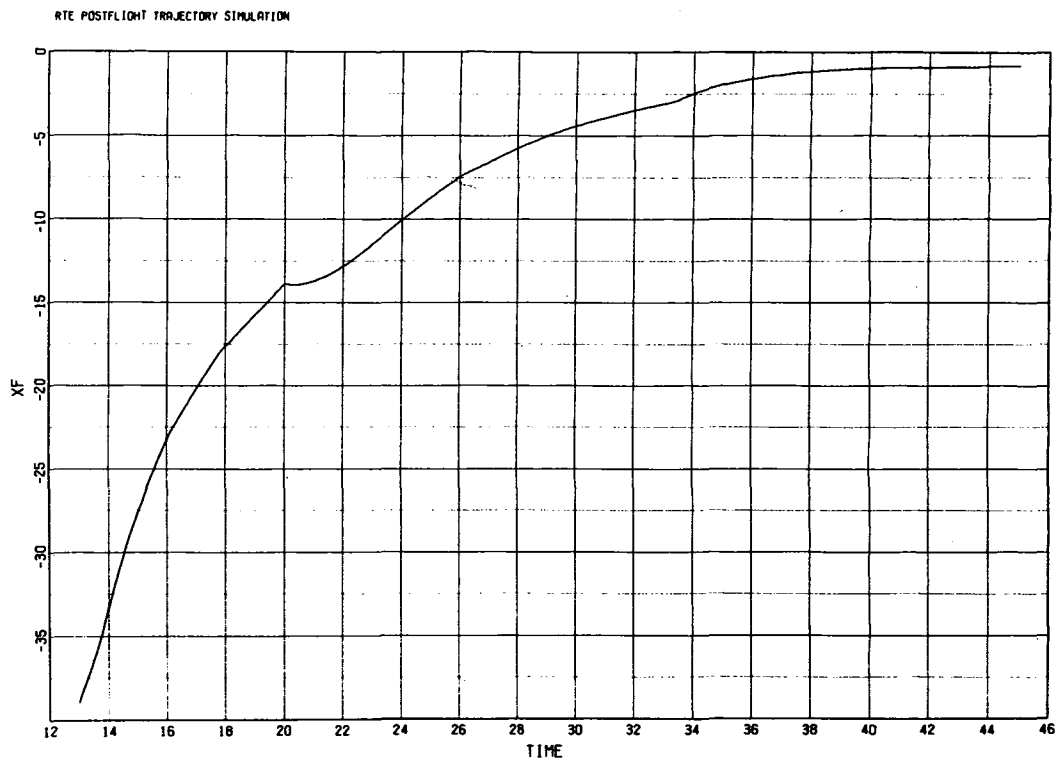

Figure 15. RTE Payload Axial Acceleration History

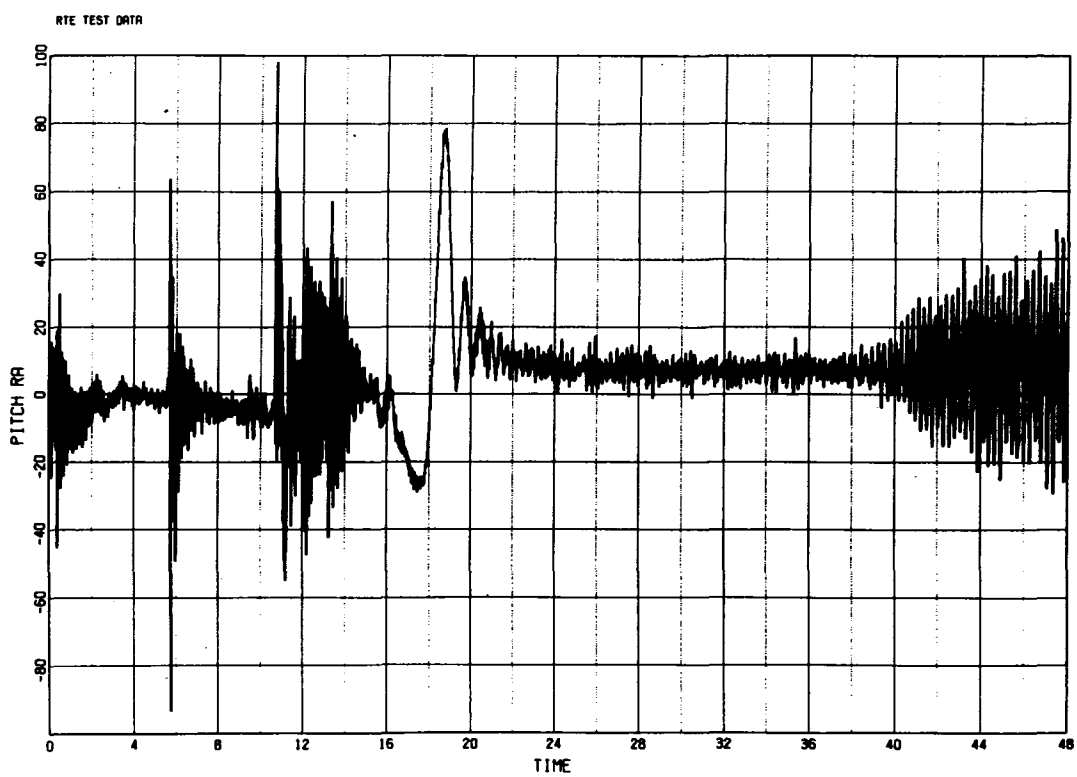

Figure 16. Pitching Velocity Versus Time

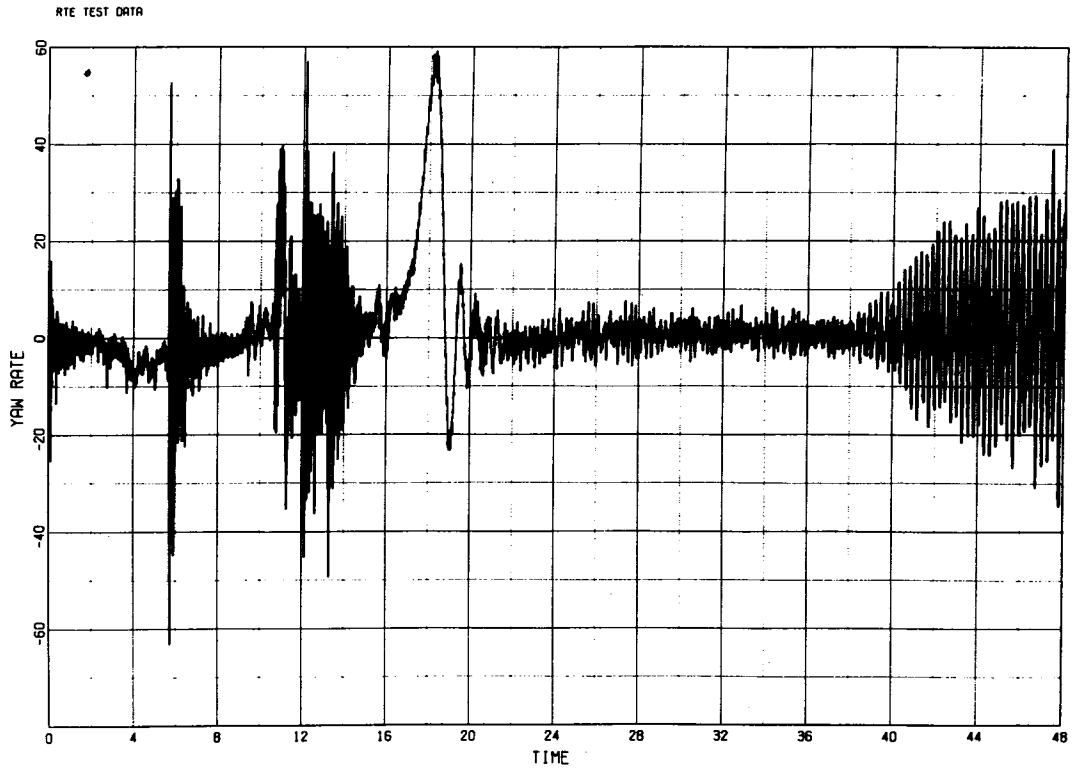

Figure 17. Yawing Velocity Versus Time

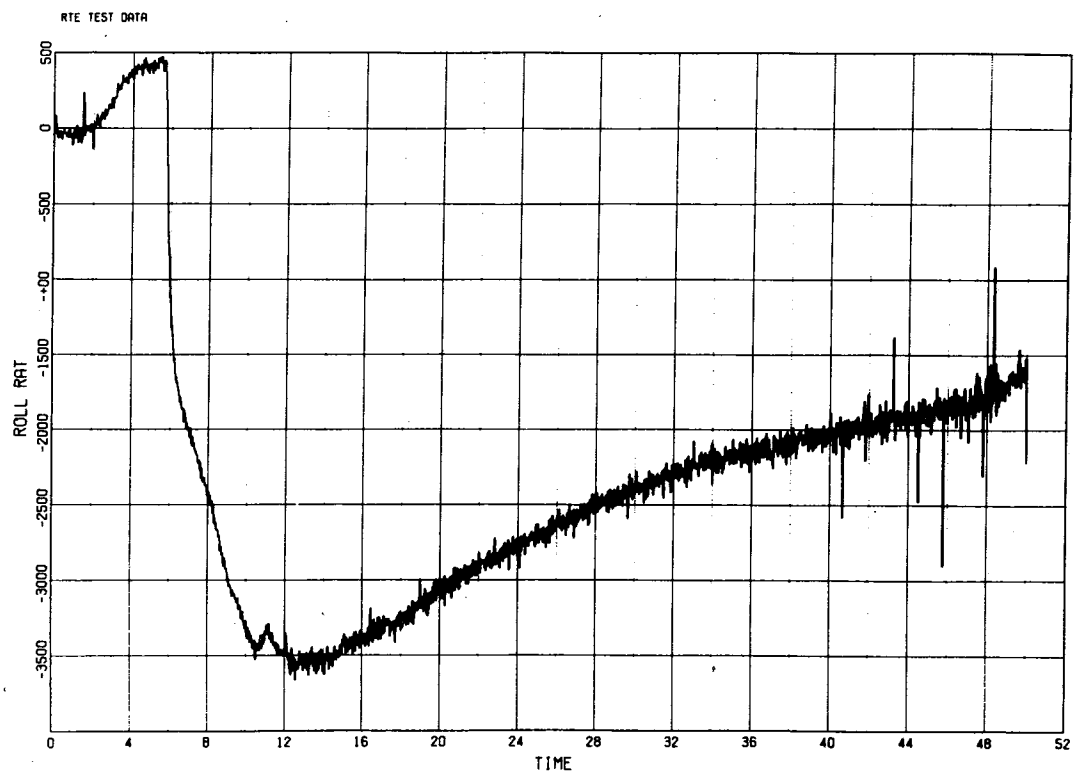

Figure 18. Rolling Velocity Versus Time

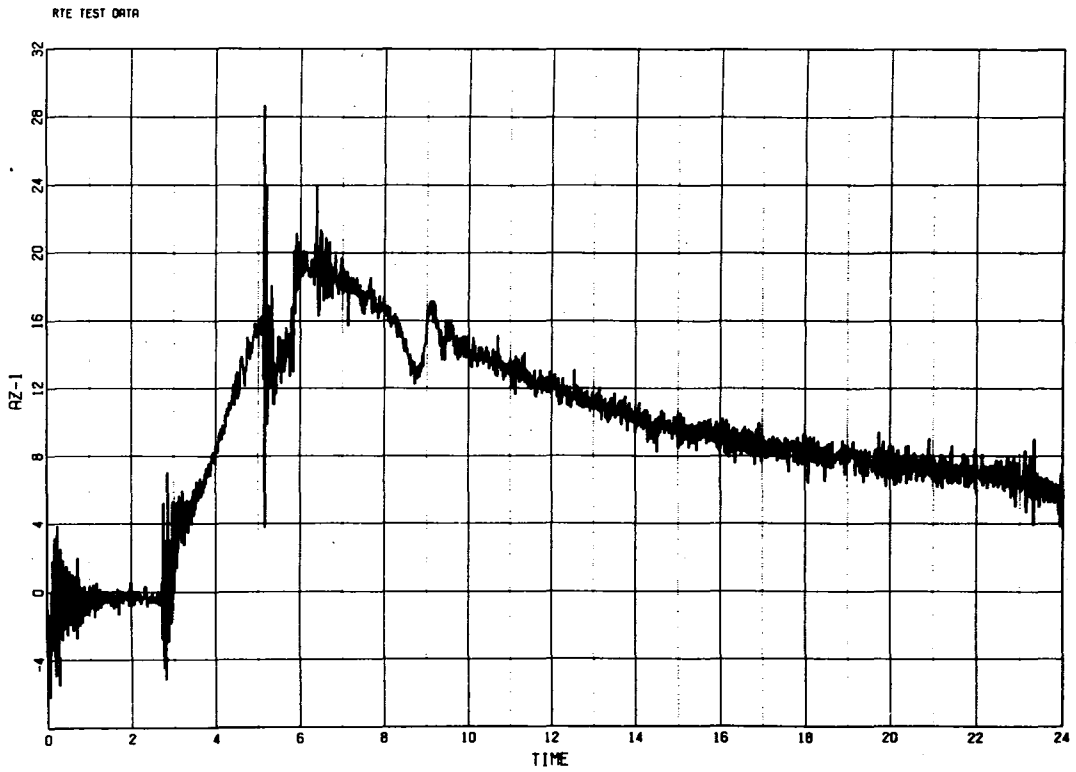

Figure 19. Lateral Acceleration History (Body Z-Axis AZ-1)

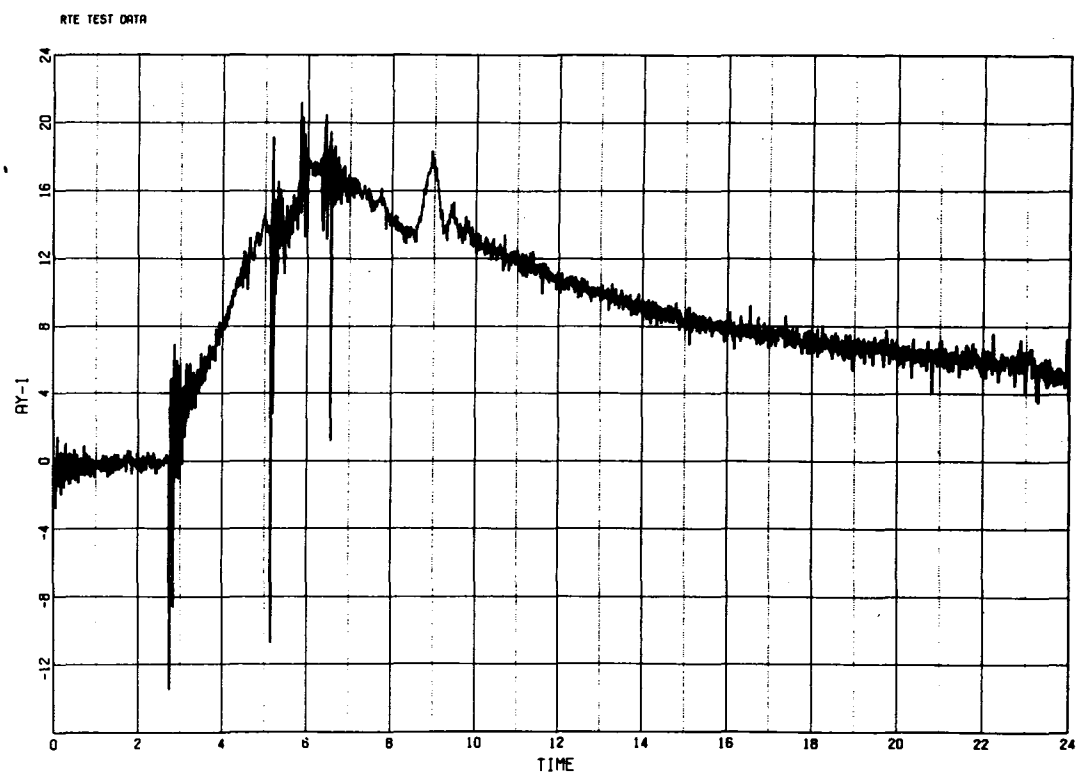

Figure 20. Lateral Acceleration History (Body Y-Axis AY-1)

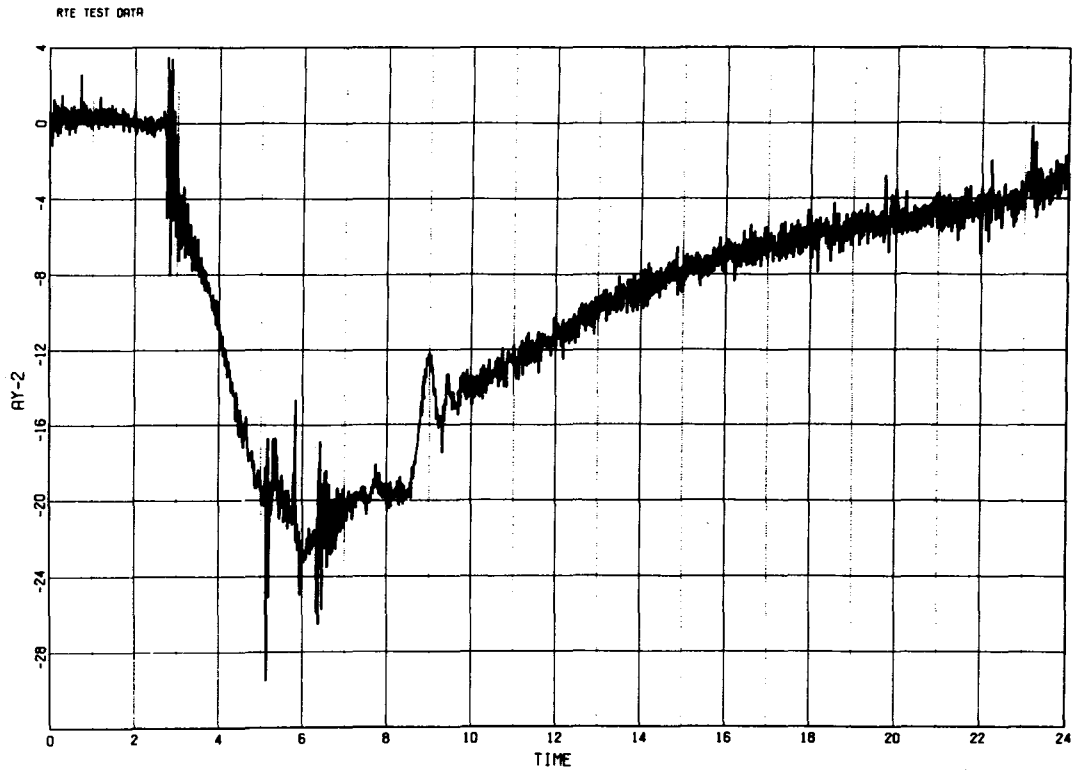

Figure 21. Lateral Acceleration History (Body Y-Axis AY-2)

Roll Dynamics Analysis

The fabrication process of the tape-wrapped carbon phenolic (TWCP) heat shield is outlined in Appendix A. As a result of this process, tape lap edges appear near the heat shield surface. It has been hypothesized that these edges, when exposed by aerothermodynamic ablation, act as small aerodynamic surfaces which induce a roll torque on the vehicle. Several theories have been formulated to describe this phenomenon (References 1, 2, 9, 10, 11). The RTE thermal shield was constructed with a positive wrap over the aft 21.5 inches, while the forward 7.44 inches had a neutral wrap. The latter was accomplished by alternating positive and negative wraps in zones of approximately 2 inches in axial length. With this wrap design, the net heat shield roll torque was expected to be positive and thus cause the spin rate to increase in the positive direction (clockwise where viewed from the rear). The flight rolling velocity history after payload separation indicates that this occurred. The total rolling moment coefficient may be obtained from the derivative of the rolling velocity history as follows

$$C_\ell = \frac{\dot{p}\, Ix}{QSd} \tag{1}$$

in which C_ℓ is the total rolling moment coefficient based on a reference

length d (base diameter), and a reference area S (base area = $\frac{\pi d^2}{4}$). The values of C_ℓ thus obtained are shown in Figure 22 as a function of time and in Figure 23 as a function of flight Mach number. At Mach 8.8 (the highest Mach number for free payload flight) C_ℓ was determined to be 0.44×10^{-5}. For the RTE flight test, C_ℓ was found to increase substantially as Mach number decreased. However, it should be pointed out that the calculated value of C_ℓ becomes more uncertain with increasing flight time as a result of both small variation in rolling velocity and small dynamic pressure.

Presented in Figure 24 is a comparison of RTE flight test rolling moment coefficient with predictions based on the theories presented in References 9, 10, and 11. The sharp cone theory developed in Reference 2 was found to greatly overpredict the flight data and is not shown. A substantial reduction in roll torque is apparently obtained in this Mach number range with blunt cones (22 percent bluntness compared with 5 percent). It should be mentioned that the theoretical predictions shown in Figure 24 are preflight predictions communicated to the author by Hall of LMSC,[9] Wells of Kaman,[10] and Wilson of Sandia[11] prior to the flight test. A more favorable comparison might be achieved if actual test parameters were used. Future effort should be given to obtaining improved theoretical estimates in view of the RTE flight data.

Aerodynamic Drag

The axial force coefficient may be found from the relation

$$C_A = \frac{-WA_x}{QS} \tag{2}$$

where A_x is the longitudinal acceleration (X axis) of the vehicle as measured by the onboard accelerometers (expressed in g's). Since two accelerometers were used to measure axial acceleration, their respective outputs (shown in Figures 6 and 7) were averaged to provide a single estimate. The axial force coefficient obtained from the calculations is shown in Figure 25 as a function of flight Mach number. Also presented for comparison are experimentally determined axial force coefficients from wind tunnel testing in References 23, 24, and 25. In the Mach range tested, flight test C_A is always greater than the wind tunnel values. The increase in drag might be attributed to the nosetip shape change due to aerothermodynamic ablation. The resulting shape (discussed later in the report) can produce greater drag in this flight regime.

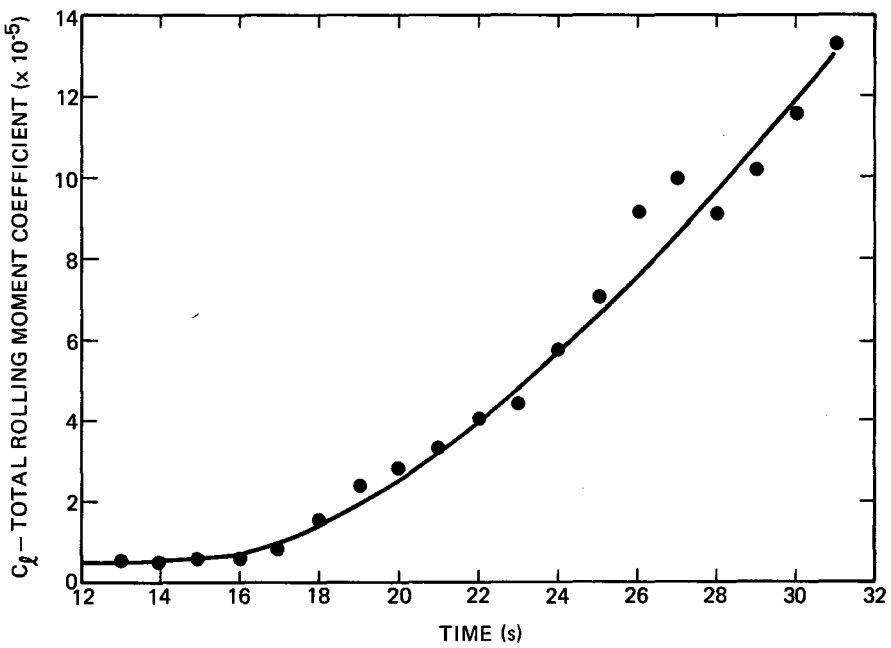

Figure 22. Total Rolling Moment Coefficient Versus Flight Time

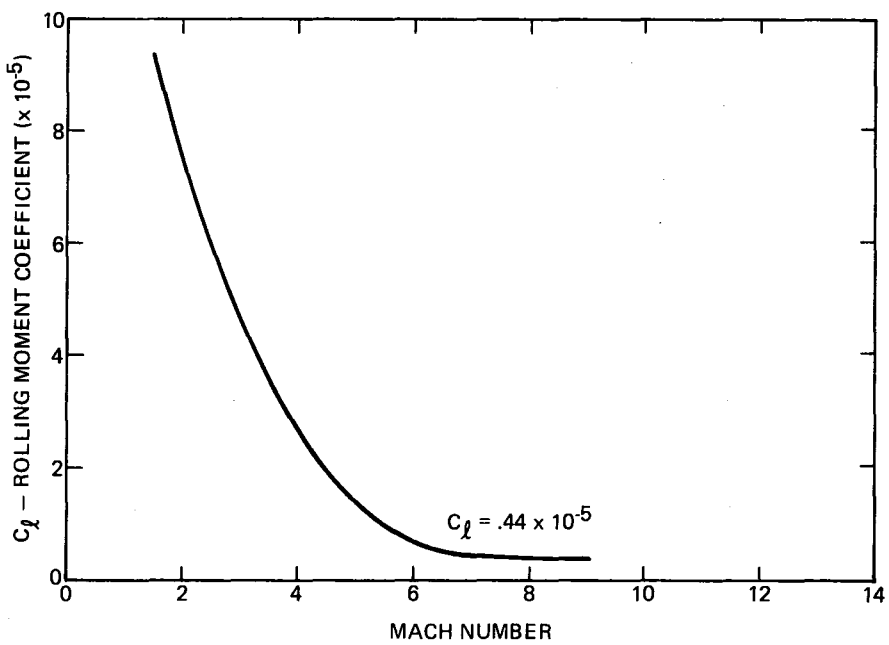

Figure 23. Total Rolling Moment Coefficient Versus Flight Mach Number

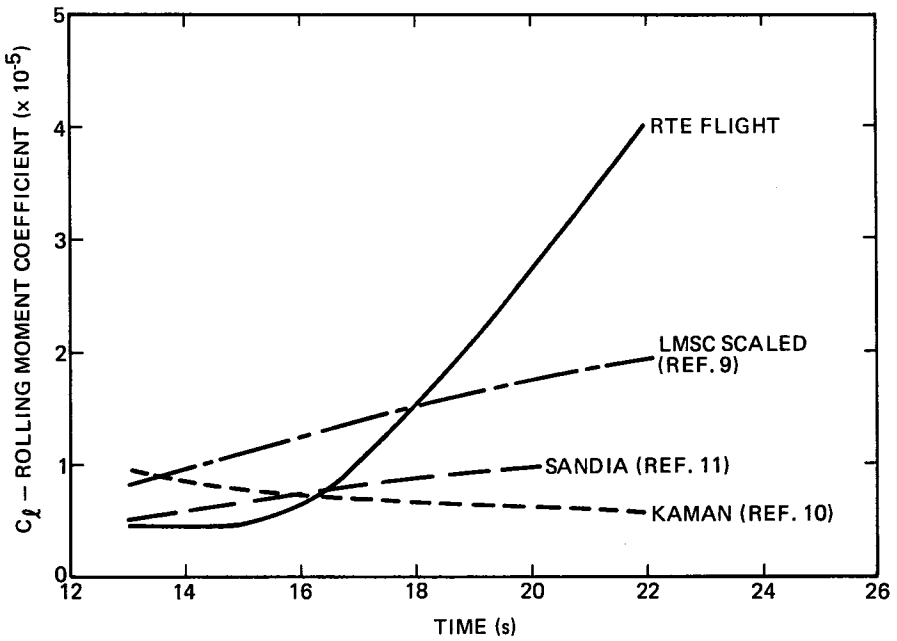

Figure 24. Comparison of RTE Total Rolling Moment Coefficient With Available Theory

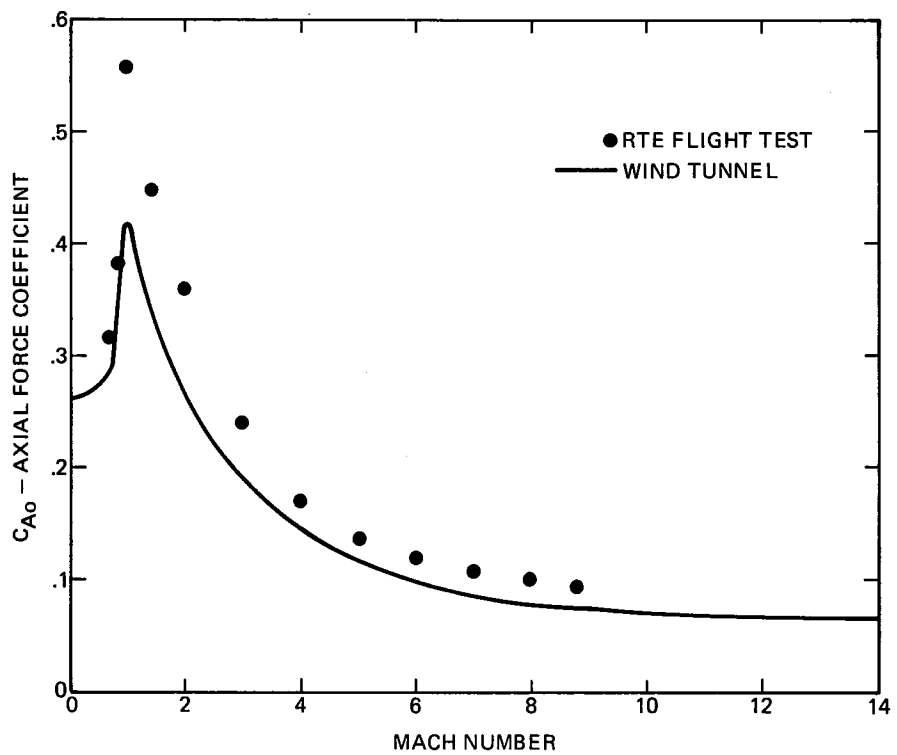

Figure 25. RTE Axial Force Coefficient (Wind Tunnel and Flight Data) Versus Mach Number

Angular Motion

The angular rate and lateral acceleration components in rolling body axes (RTE measurement system) may be used to obtain the flight vehicle angle of attack performance with the methods presented in References 26, 27, and 28. Using this approach and the existing flight data, the angle of attack and the angle of sideslip were computed. These and the total angle of attack and the aerodynamic roll angle (windward meridian orientation) are given respectively by the following:

$$\alpha_{tot} = \sqrt{\alpha^2 + \beta^2} \tag{3a}$$

$$\phi_A = \tan^{-1} (\beta / \alpha) \tag{3b}$$

are shown in Figures 26 through 29.

An initial angle of attack of approximately 2.6 degrees due to booster/payload separation is seen to exhibit good damping. An angular divergence to approximately 1.8 degrees beginning at T = 17 seconds is attributed to a momentary roll resonance at T = 18.5 seconds. At this time the roll rate becomes equal to the vehicle natural pitch frequency, and a trim-angle-of-attack amplification takes place. The passage through resonance is nominal and sustained roll resonance is avoided. The angle of attack subsequently exhibits good static and dynamic stability and converges to small values by T = 23 seconds.

An investigation of the pitching and yawing velocities of Figures 16 and 17 indicates that after convergence of the angular disturbance which occurs at T = 18.0 seconds, a pitching rate offset of approximately 8 deg/s with essentially no yawing rate offset is present. Assuming this offset is due to trim, a trim angle of approximately 0.2 degrees was calculated as being present.

Static Stability

In order to analyze the stability characteristics of the RTE flight data, a differential corrections curve fit was made to the angular rate data. From References 26, 27, and 28, the equation

$$\vec{q} = K_1 e^{\phi_{N_B} t} + K_2 e^{\phi_{P_B} t} + K_3 \tag{4a}$$

where $\vec{q} = q + ir$ is the complex pitching velocity with q and r being the body pitching and yawing velocities as measured by the rate gyros, may be fit to

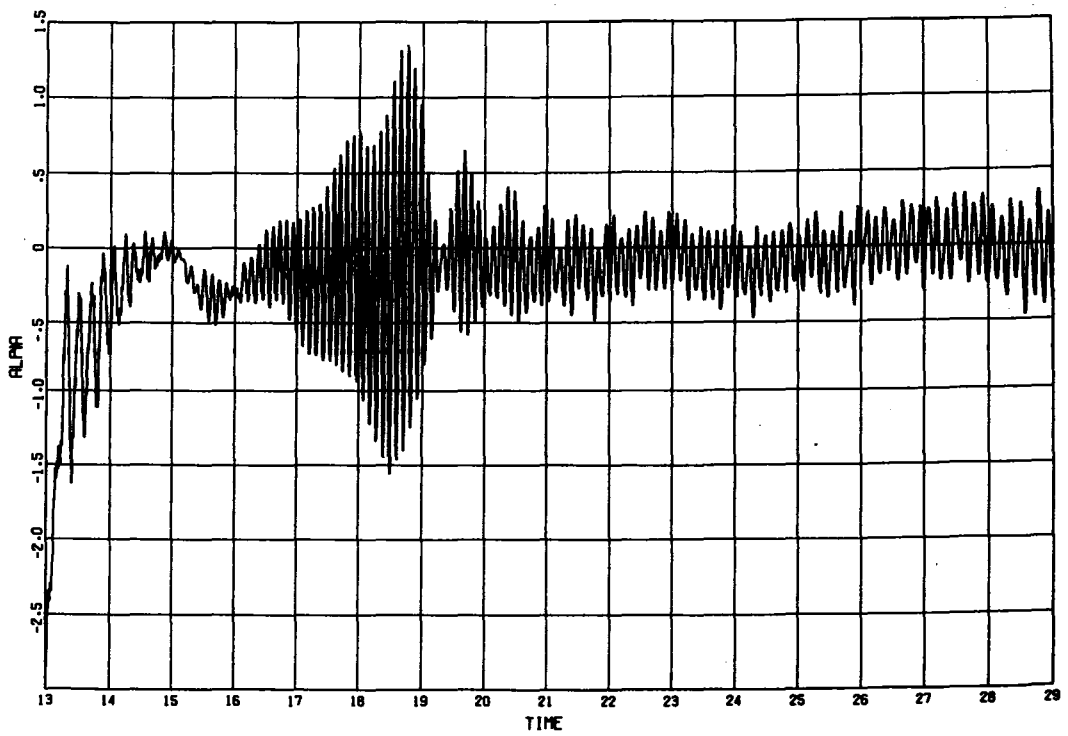

Figure 26. Angle-of-Attack History (Computed From Flight Data)

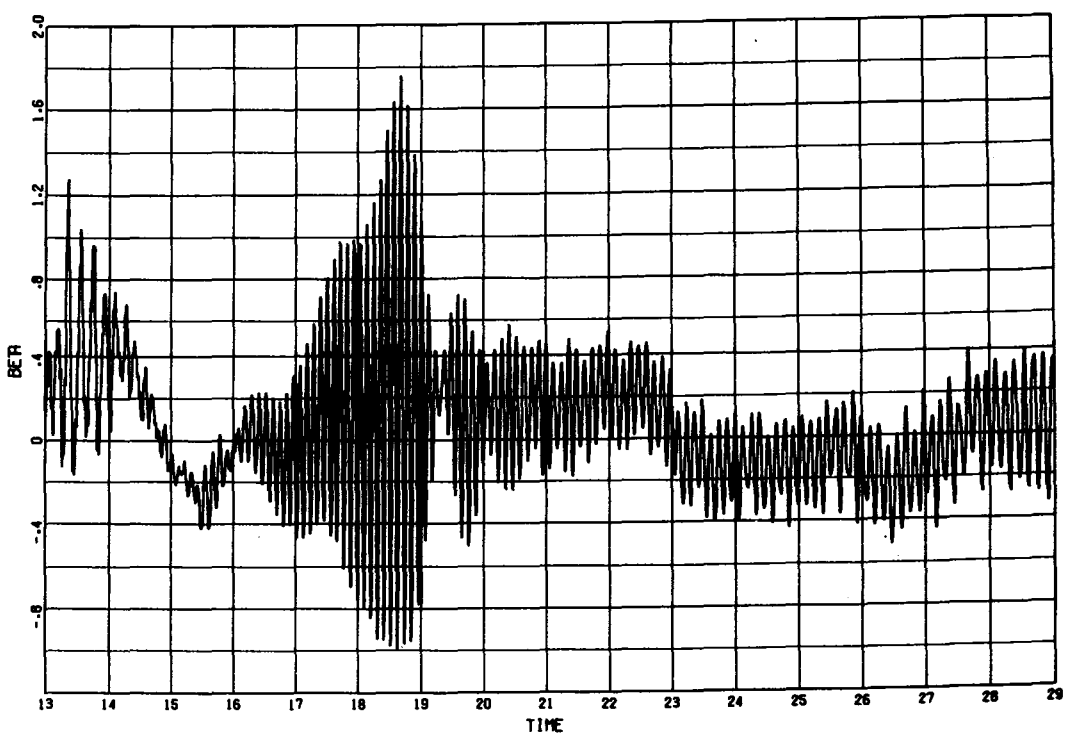

Figure 27. Angle-of-Sideslip History (Computed From Flight Data)

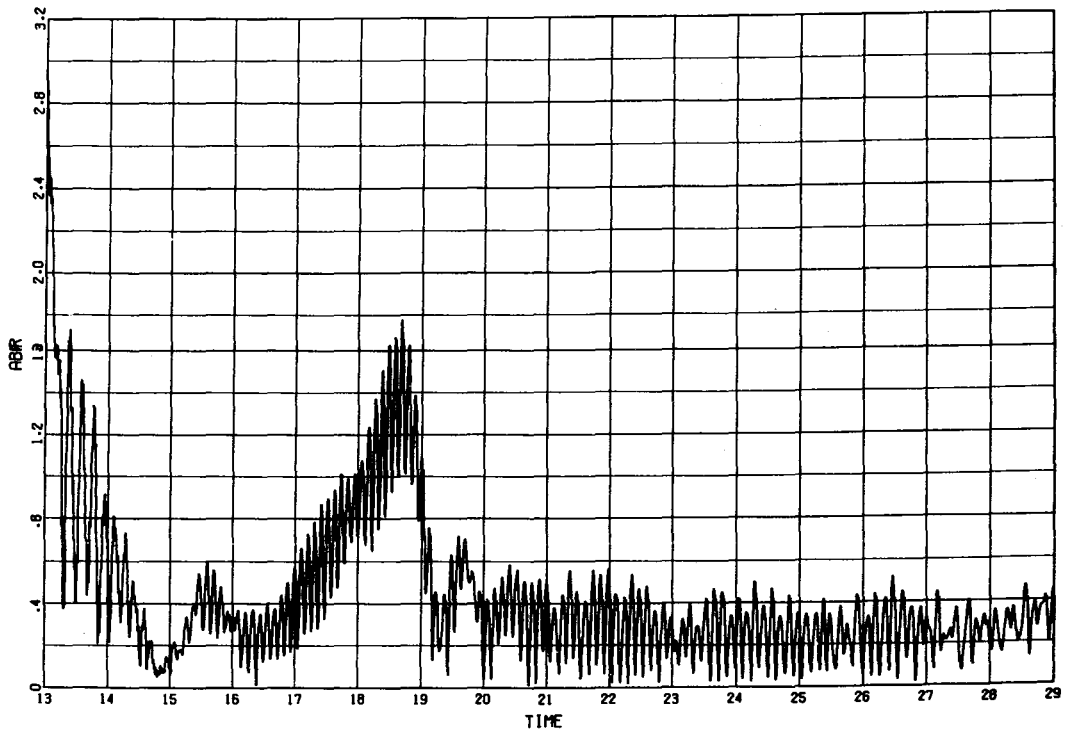

Figure 28. Total Angle-of-Attack History (Computed From Flight Data)

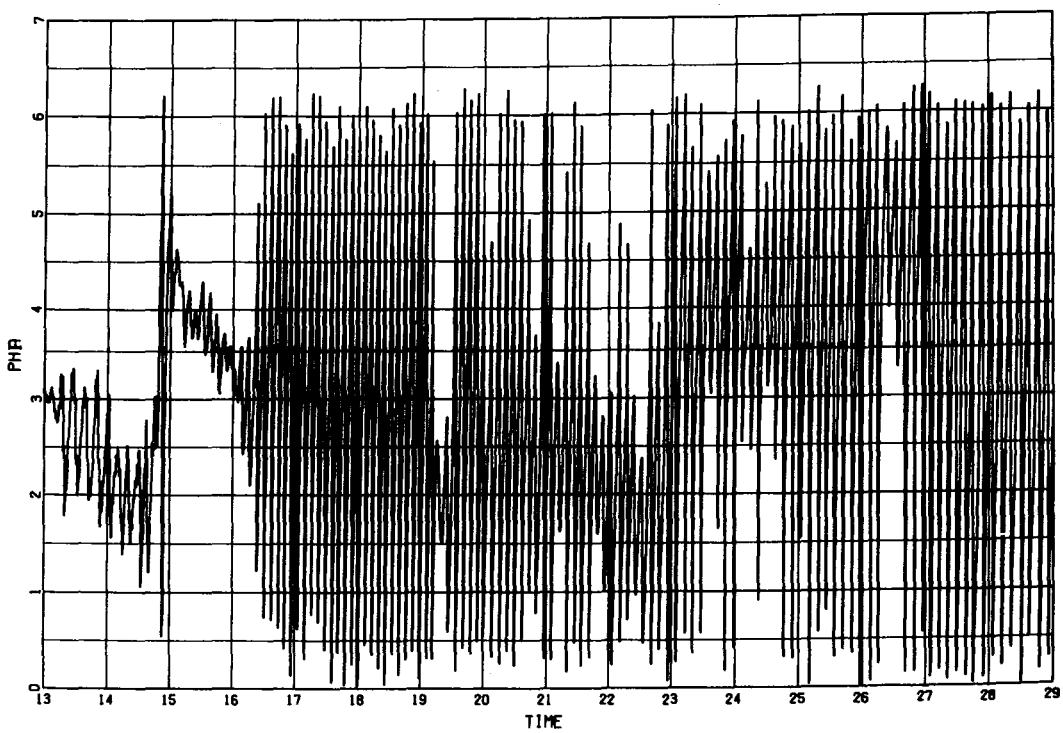

Figure 29. Aerodynamic Roll Angle History (Computed From Flight Data)

the flight data. From this fit, the static stability coefficient

$$C_{m_\alpha} = \partial C_m / \partial \alpha \tag{4b}$$

may be computed from the motion frequencies. The C_{m_α} resulting from this process is presented in Figure 30 as a function of flight Mach number. Also shown are wind tunnel measured values of C_{m_α} from References 23, 24, and 25. The wind tunnel measurements are found to be in good agreement with the theoretical methods for static stability determination given in References 29, 30, and 31. Flight test values of C_{m_α} are seen to be lower (thus indicating less stability) than wind tunnel values.

A more meaningful measurement of the RTE static stability may be expressed in terms of the aerodynamics center of pressure X_{cp}. This can be expressed in terms of C_{m_α} and the normal force coefficient derivative C_{n_α}, as follows:

$$C_{m_\alpha} = C_{n_\alpha} (X_{cp} - X_{cg})/d \tag{5}$$

The normal force coefficient, determined from the wind tunnel data (References 23, 24, and 25), is given in Figure 31. The aerodynamic center of pressure resulting from Equation (5) is shown in Figure 32 as a function of flight Mach number. For convenience in determining the static margin, the center of gravity is also shown. Both X_{cp} and X_{cg} are expressed as a percentage of body length from the actual nose. Since the angle of attack converged to very small values at certain times during the flight, the differential corrections curve fit to the angular rates was not possible during these times. Consequently, the flight values of C_{m_α} and X_{cp} were only determined at the Mach numbers shown in Figures 31 and 32. The test vehicle was determined to have a minimum static margin of approximately 7 percent at Mach 3. The test data indicate a reduction of 1 to 2 percent in X_{cp} at Mach 3 and Mach 8 and as much as 3 percent at Mach 6. The loss in stability, although not detrimental to test objectives, may be attributed to the erosion pattern of the nosetip.

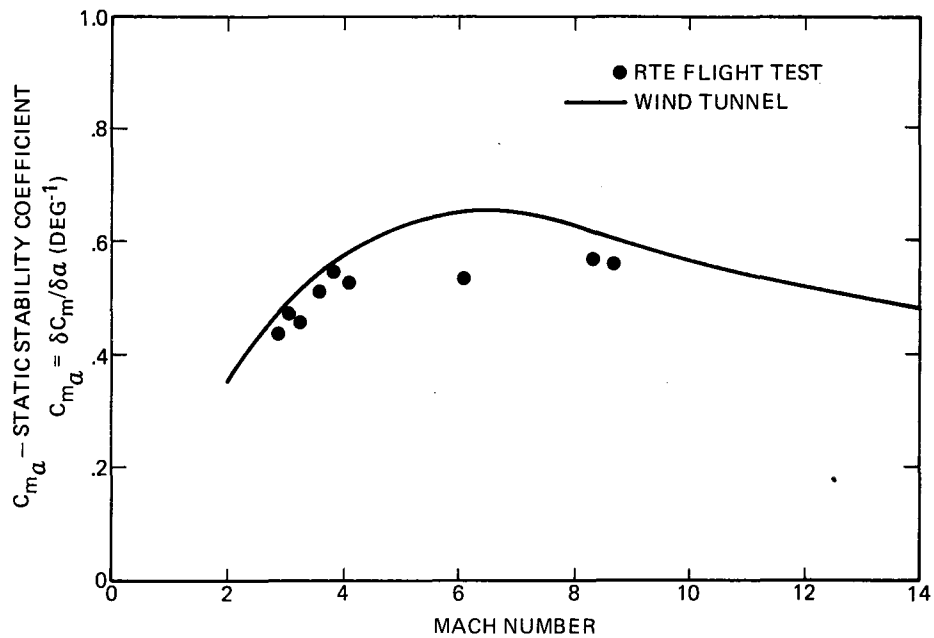

Figure 30. RTE Normal Force Coefficient Versus Mach Number (From Wind Tunnel)

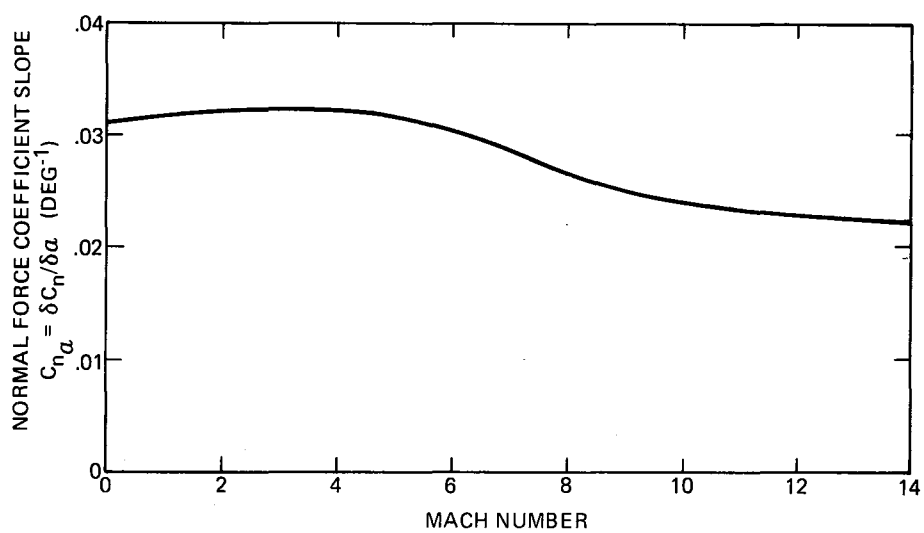

Figure 31. RTE Static Stability Coefficient (C_{m_α}) Versus Mach Number (Comparison of RTE Flight Test and Wind Tunnel Data)

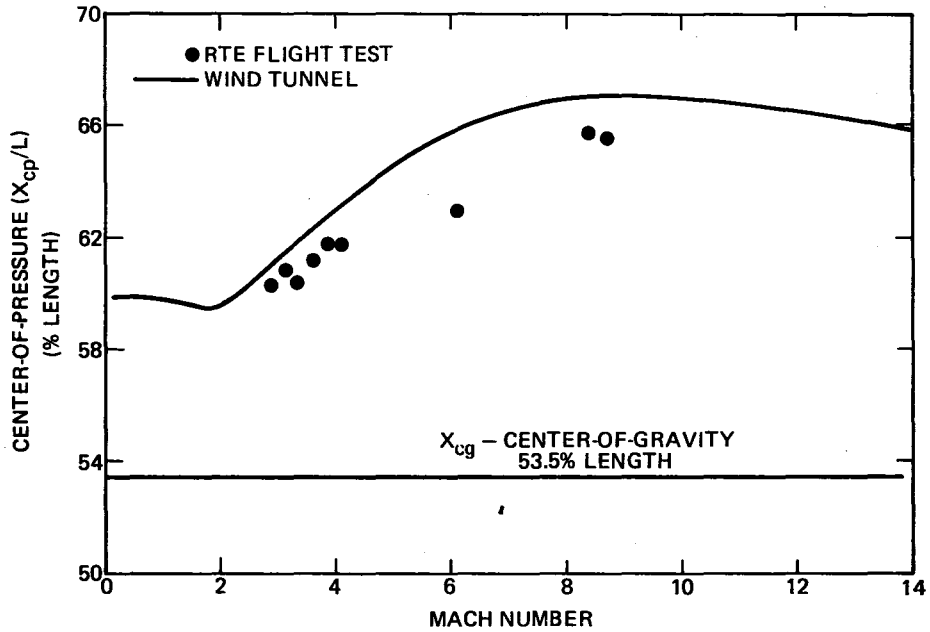

Figure 32. Center-of-Pressure (X_{cp})

Using the flight-test-derived values of C_{m_α} and the rolling moment coefficient C_ℓ (determined previously), the trajectory simulation resulted in the spin rate and natural pitch frequency (P_{crit}) histories shown in Figure 33. The resonance encountered at T = 19 seconds is clearly indicated. Other flight variables such as angle of attack were equally well determined by the trajectory simulation. A summary of these computations is presented in Appendix D.

Aerothermodynamic Analysis

Aerothermodynamic instrumentation for RTE consisted of four thermal stacks, each having three thermocouples located at depths of 0.020, 0.040, and 0.100 inch from the heat shield outer surface. These stacks were located at stations 19.0, 22.75, and 28.50. Three of the stacks were damaged during the several assemblies and disassemblies of the flight vehicle during ground testing and other preparations for flight testing; no flight data were obtained with the damaged instruments. However, the data from one full stack (three thermocouples) located at station 19.0 was obtained. A time history of the heat shield temperature at three depths from the outer surface

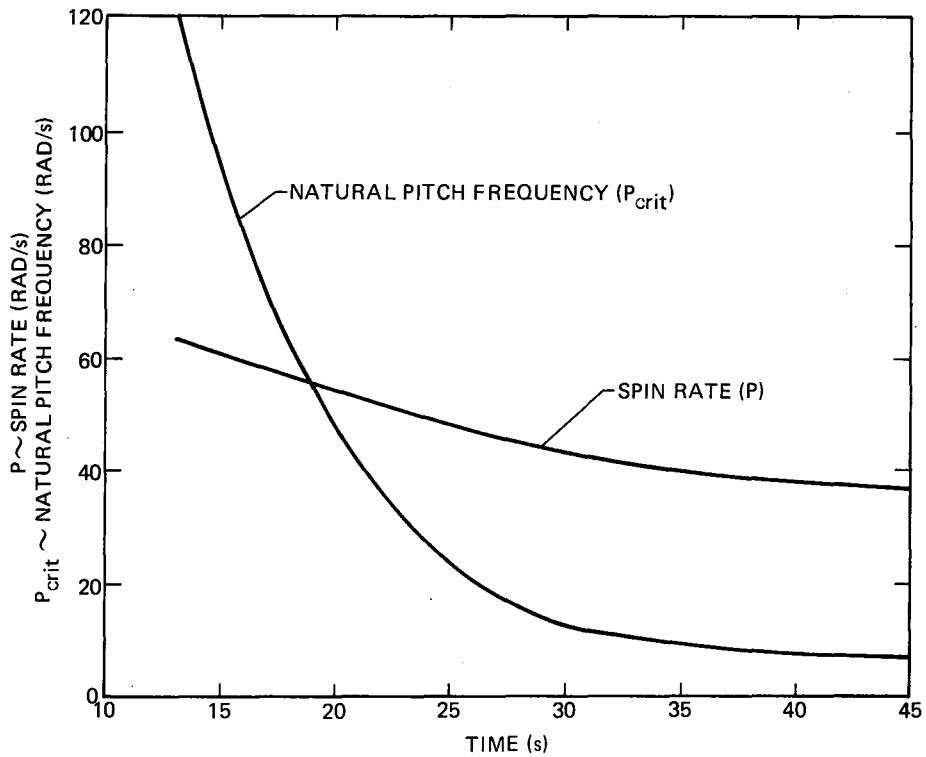

Figure 33. RTE Spin Rate and Natural Pitch Frequency History

was obtained. These data also monitored the progress of thermochemical ablation of the heat shield. In addition, one other thermocouple (located at station 28.5 at 0.10 inch from the surface) also provided temperature data during flight.

Although the thermal instrumentation was limited, it does provide sufficient information to ascertain the amount of ablation obtained, as well as to verify calculational techniques. To provide a more complete representation of the heat shield and nosetip response, the flight thermodynamic data will be augmented substantially and, where permissible, compared with analytical calculations.

Heat Shield Thermal Data

The temperature response of the heat shield at station 19 is presented in Figure 34. The three thermocouples (T-3, T-4, and T-5) were nominally located at depths of 0.020, 0.040, and 0.100 inch, respectively. At T = 12 seconds, burnthrough was detected at T-3 (0.020 inch) while T-4 (0.040 inch) was detected to burn through at T = 13 seconds (at payload separation). Ablation is therefore considered as having advanced to these heat shield depths at the times indicated. T-5 measures the temperature at 0.100 inch at the 19.0 inch station, while T-14 is also located at 0.100 inch but at the 28.50 inch station. T-5 has an upper limit of 1300°F and therefore is saturated between T = 16 and 24 seconds.

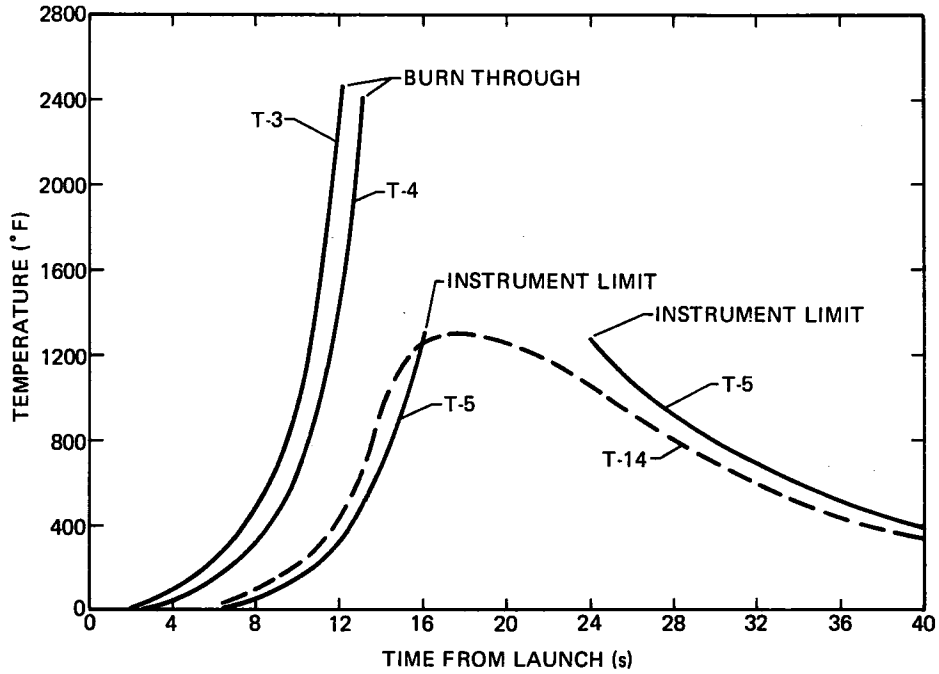

Figure 34. RTE Heat Shield Temperature Response Versus Time (Flight Data)

Theoretical Heat Shield Aerodynamic Heating

The cold wall (T_w = 537°R) nonablating aerodynamic heating rates were calculated with the SCORCH code,[32] using the nominal trajectory and assuming fully turbulent flow. Calculations were performed for the 2.0, 7.0, 12.0, 19.0, 22.75, and 28.50 inch stations, the last three stations corresponding to the location of the heat shield thermal stacks.

Figure 35 presents the cold wall heating rates as a function of time from lift-off until parachute deployment for stations 2.0 and 9.0. The 2.0-inch station is immediately aft of the graphite nosetip. Peak heating is calculated as occurring at each station at the end of the third-stage burn. A maximum heating rate of 1275 Btu/ft^2-s occurs at the forward station, while aft of the 9-inch station (the section of heat shield having full positive wrap), the peak heating is approximately 600 Btu/ft^2-s.

A peak surface pressure of 3.6 atmospheres occurs at the 2-inch station at third-stage burnout. This decreases to approximately 1.6 atmospheres at the 28.5-inch station.

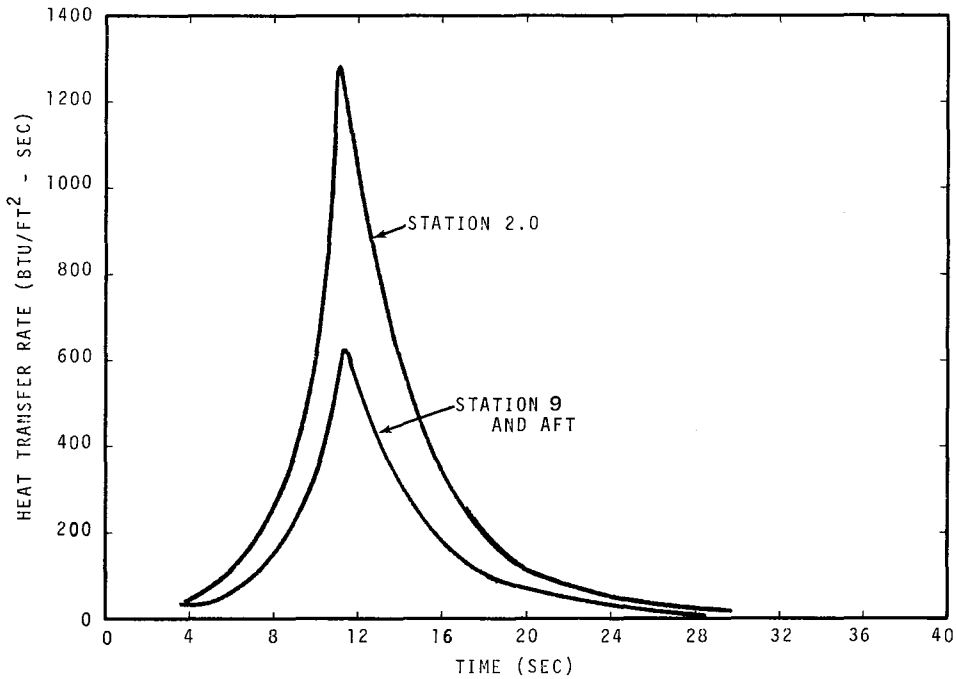

Figure 35. Cold Wall Convective Heat Transfer Rate (Station 2 and Aft of Station 9)

Heat Shield Performance

The CMA[33] computer code was used in the heat shield ablation and thermal analysis. The calculated temperature response of the thermal stacks is presented in Figure 36. A thermal stack is located at each of three body stations (stations 19.0, 22.75, and 28.5). Two stacks are at the 28.5 station. Each stack has thermocouples at depths of 0.020, 0.040, and 0.100 inch from the heat shield surface. Note that the outermost thermocouples in each stack may be used to mark the progress of heat shield ablation and that burnout for the first thermocouple of each stack is seen to occur at about payload separation (T = 13 seconds). Calculations also indicated that peak backface temperatures did not exceed 400°F for the duration of the flight.

Favorable agreement is obtained with the analytical calculations. Figure 36 may be compared with the measured values (T-3, T-4, and T-5) in Figure 34. Further comparison can be made with the innermost thermocouple T-14 and the calculation shown in Figure 36c. In each case the theoretical values are in good agreement with the flight-test measurements.

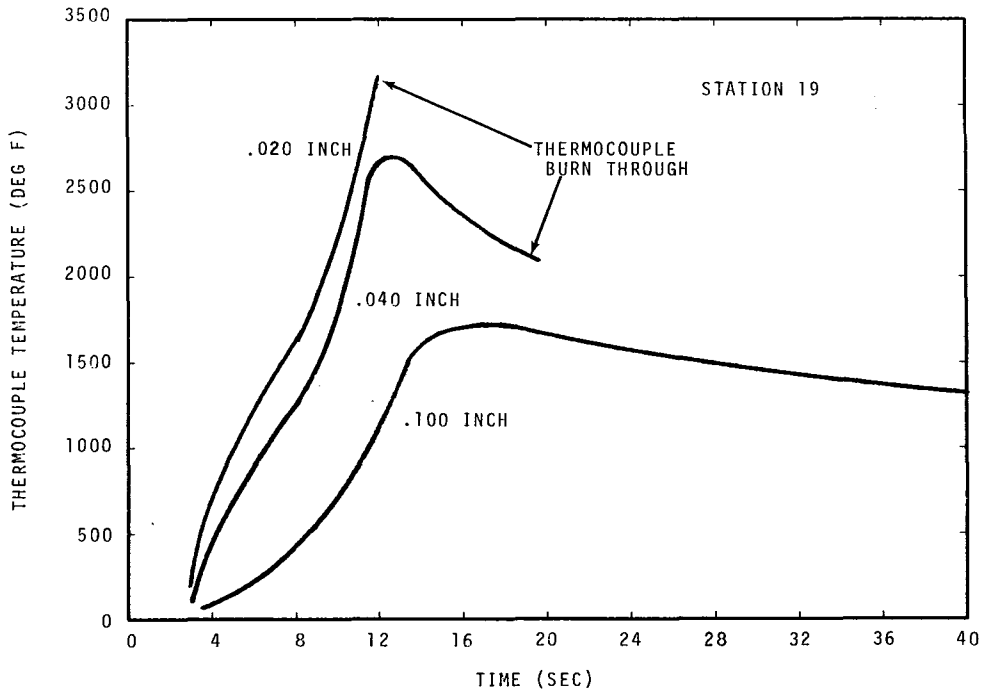

a. Calculated Temperature Response at Station 19

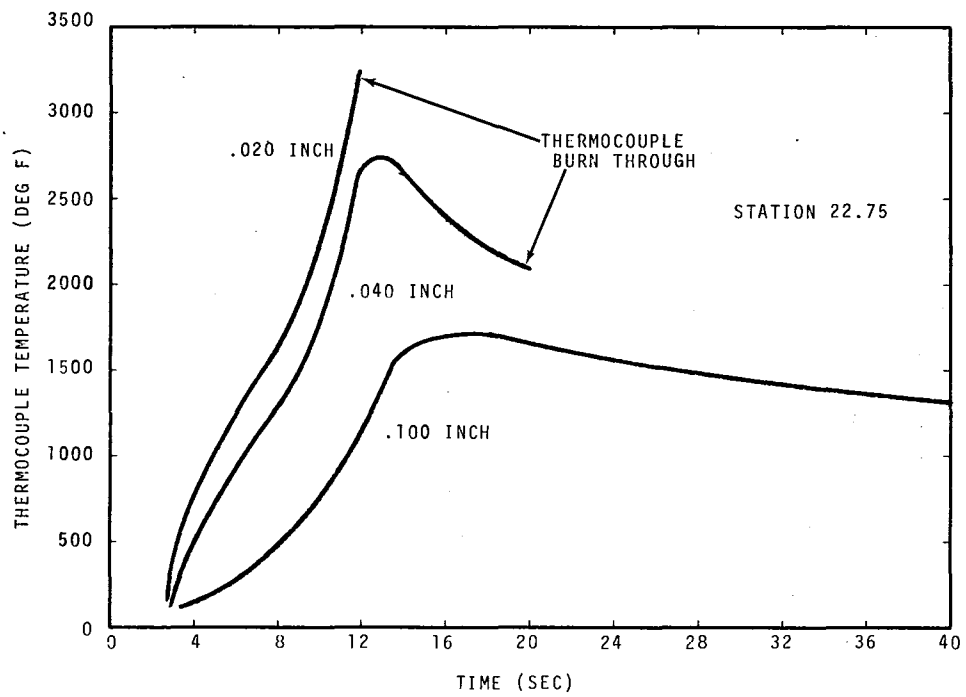

b. Calculated Temperature Response at Station 22.75

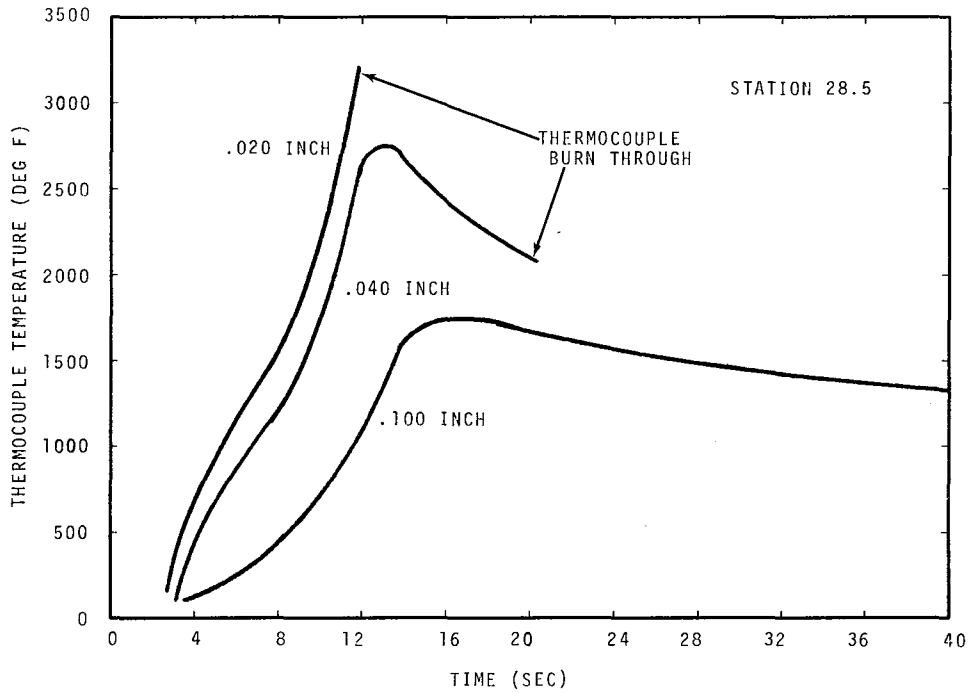

c. Calculated Temperature Response at Station 28.5

Figure 36. Thermal Stack Temperature Response (Temperature History at Depths of 0.020, 0.040, and 0.10 Inch From the Cone Surface at Stations 19.0, 22.75, and 28.5)

Figure 37 presents the calculated recessions for the 2.0-inch station and the full positive wrap section (aft of station 9). A maximum recession of 0.166 inch occurs at the 2.0-inch station and approximately 0.07 inch aft of station 9. For all stations, the recession is greater than 0.015 inch at third-stage burnout. It is important to note that this recession is of the order of the tape lap height, so that the heat shield surface perturbations are fully developed at the beginning of the free flight portion of the trajectory. The flight recession data, given by burnthrough on thermocouples T-3 and T-4, are also shown in Figure 37. The test data indicate that the ablation achieved by payload separation was sufficient to produce complete exposure of the tape laps.

Recovered RTE Heat Shield

Figures 38, 39, and 40 show the condition of the recovered RTE thermal shield. Considerable delamination was noted along the full length of the test vehicle. Close examination of the condition of the heat shield did not reveal the clear and distinctive presence of tape joints, holes, or any other obvious surfaces. An occasional lap was detected but at a much lower frequency than expected. In a few cases, the thread used to stitch the tape joints was found protruding from the surface. Some holes in the shield were also observed. No conclusive evidence in favor of any type of surface protrusion was obtained.

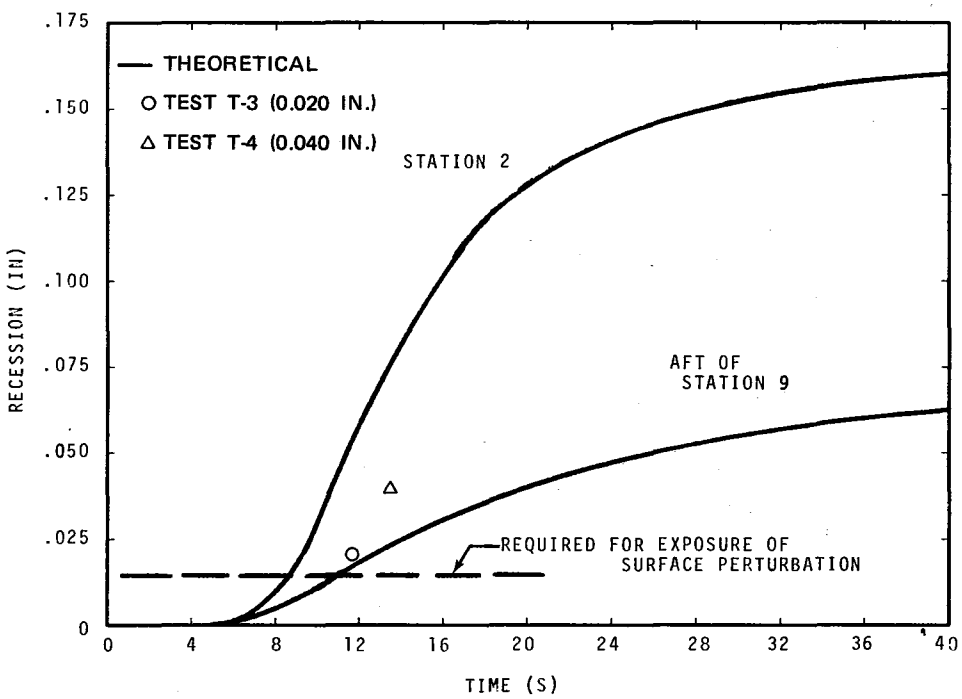

Figure 37. Theoretical and Flight Test Surface Recession for Station 2 and Aft of Station 9

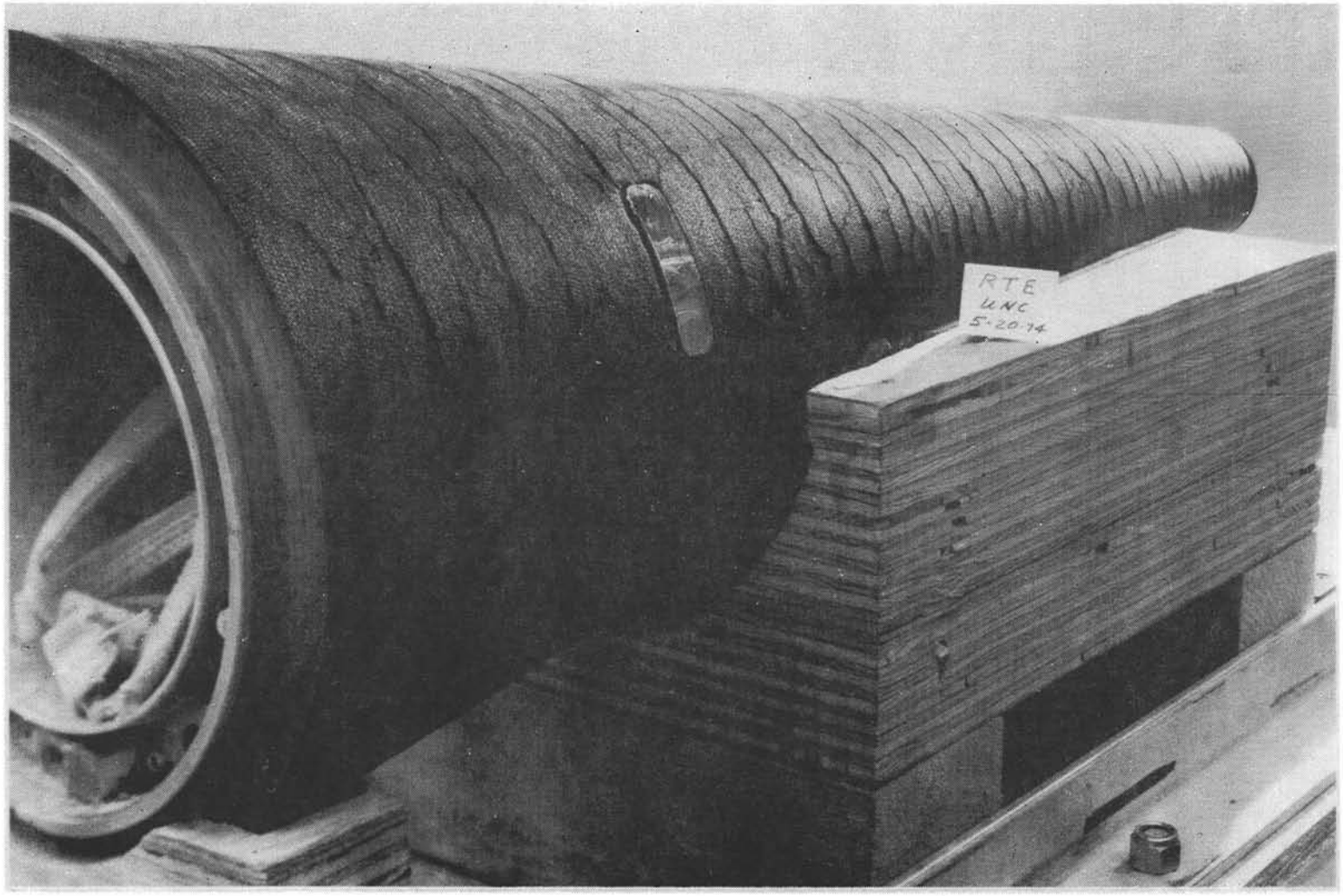

Figure 38. Recovered RTE Heat Shield

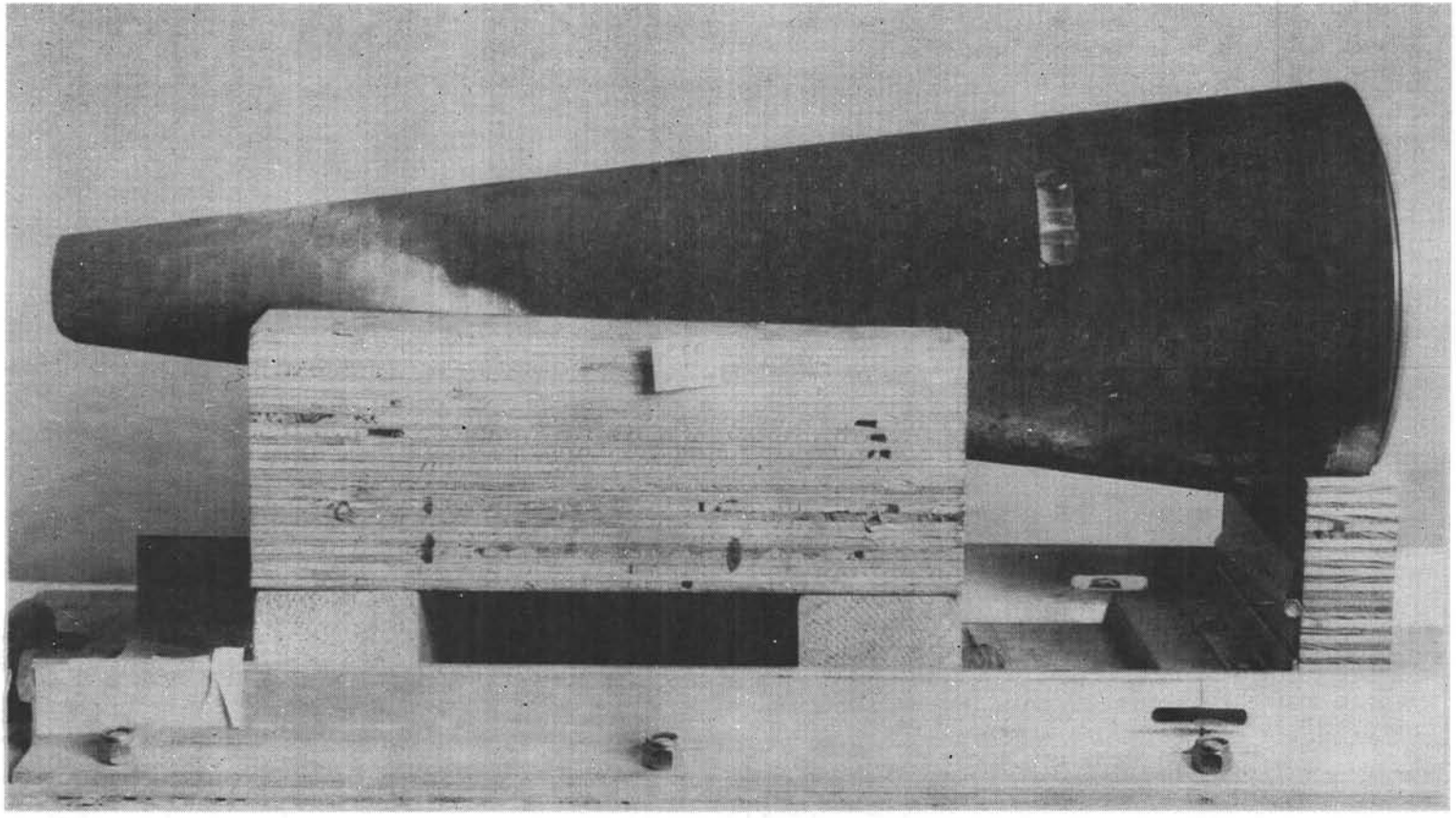

Figure 39. Recovered RTE Heat Shield

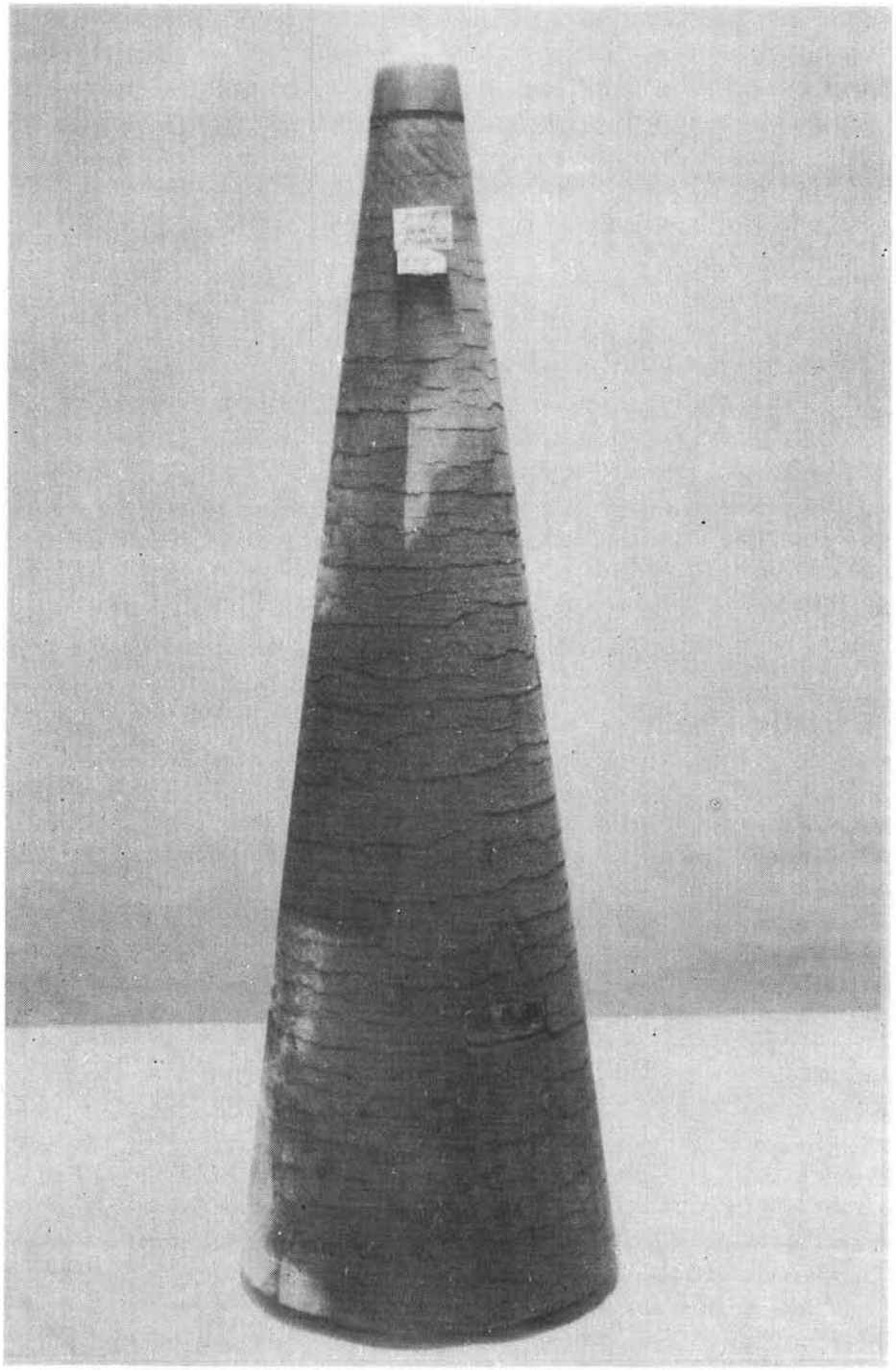

Figure 40. Recovered RTE Heat Shield

Nosetip Performance

Since there was no nosetip instrumentation used on RTE, the discussion in this and the following section is based on analytical calculations for temperature, ablation, and structural response of the nosetip. The nosetip was recovered intact and achieved a turbulent heating shape as shown in Figures 41 through 45. Figure 46 reveals the presence of small grooves along the length of the nosetip. Measurement of the stagnation point revealed approximately 0.30 inch of erosion. Sidewall erosion was small at the aft end of the tip (approximately 0.005 inch). Shoulder erosion between 30 degrees and 60 degrees from the stagnation point was severe and asymmetrical. This erosion asymmetry could account for the presence of a small trim angle which was amplified to approximately 1.8 degrees during roll resonance. The higher-than-expected drag coefficient may also be attributed to the nosetip shape change. The amount of erosion may be compared with the preflight nosetip profile in Figure 47.

The SCORCH[32] computer code was used to calculate flowfield characteristics and aerodynamic heating. Figure 48 illustrates the pressure and cold wall heat flux at the stagnation point, and Figure 49 shows the cold wall heat flux at a surface 0.75 inch downstream of the stagnation point for both laminar and turbulent flow. The heating computations were carried out for a number of possible situations. These included (1) fully turbulent flow over the entire nosetip; (2) laminar flow to the "tangency-point" and turbulent flow from there on; (3) fully laminar flow for the first 11 seconds of flight, then complete and instantaneous transition to turbulent flow. The third situation is included in the analysis, since it is assumed to represent a worst case from the thermal stress viewpoint.

The material ablation, surface recession, and in-depth heat conduction were calculated using the ASTHMA[34] code. The time interval considered in the computations included the first 34 seconds of the flight. After this time the heat transfer and recession rates are at least an order of magnitude less than their peak values. Figures 50 through 52 illustrate the predicted nosetip profiles at various times during the flight for the three situations considered. Both the fully turbulent and transition calculations predict similar "final" nosetip profiles which result from 0.15 inch and 0.30 inch of recession at the stagnation point and 0.100 inch downstream, respectively. The recession for fully turbulent flow was also calculated using the Sandia model[35] for enhanced recession due to particulate removal. This resulted in about a 50 percent increase in recession. Figures 53 through 55 show the temperature distributions along the nosetip centerline for the three cases considered. The fully turbulent case results in the highest temperatures; the transition case gives the steepest gradients; and the laminar-to-tangency point case is the least severe.

Figure 41. Recovered RTE Nosetip (0° Orientation)

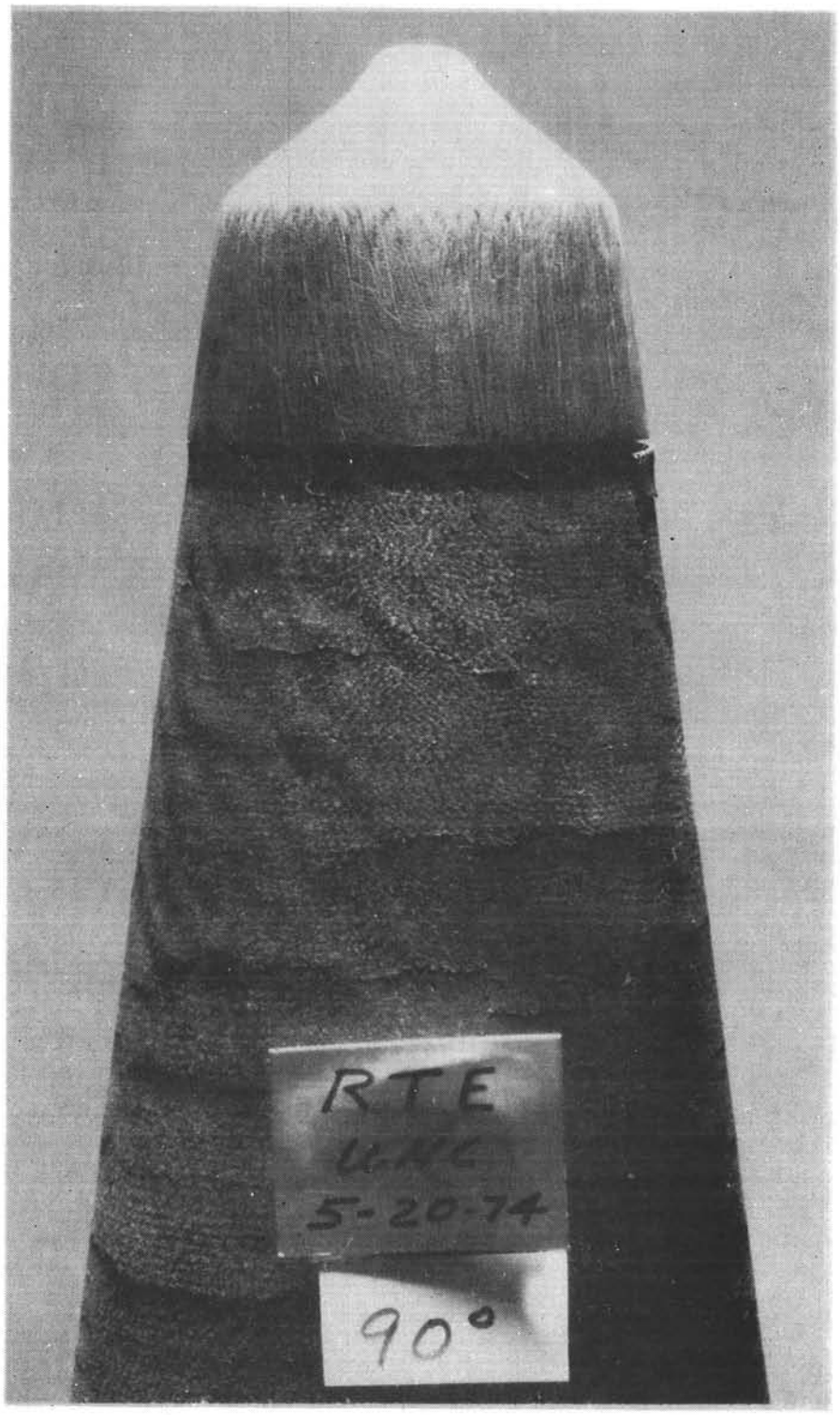

Figure 42. Recovered RTE Nosetip (90° Orientation)

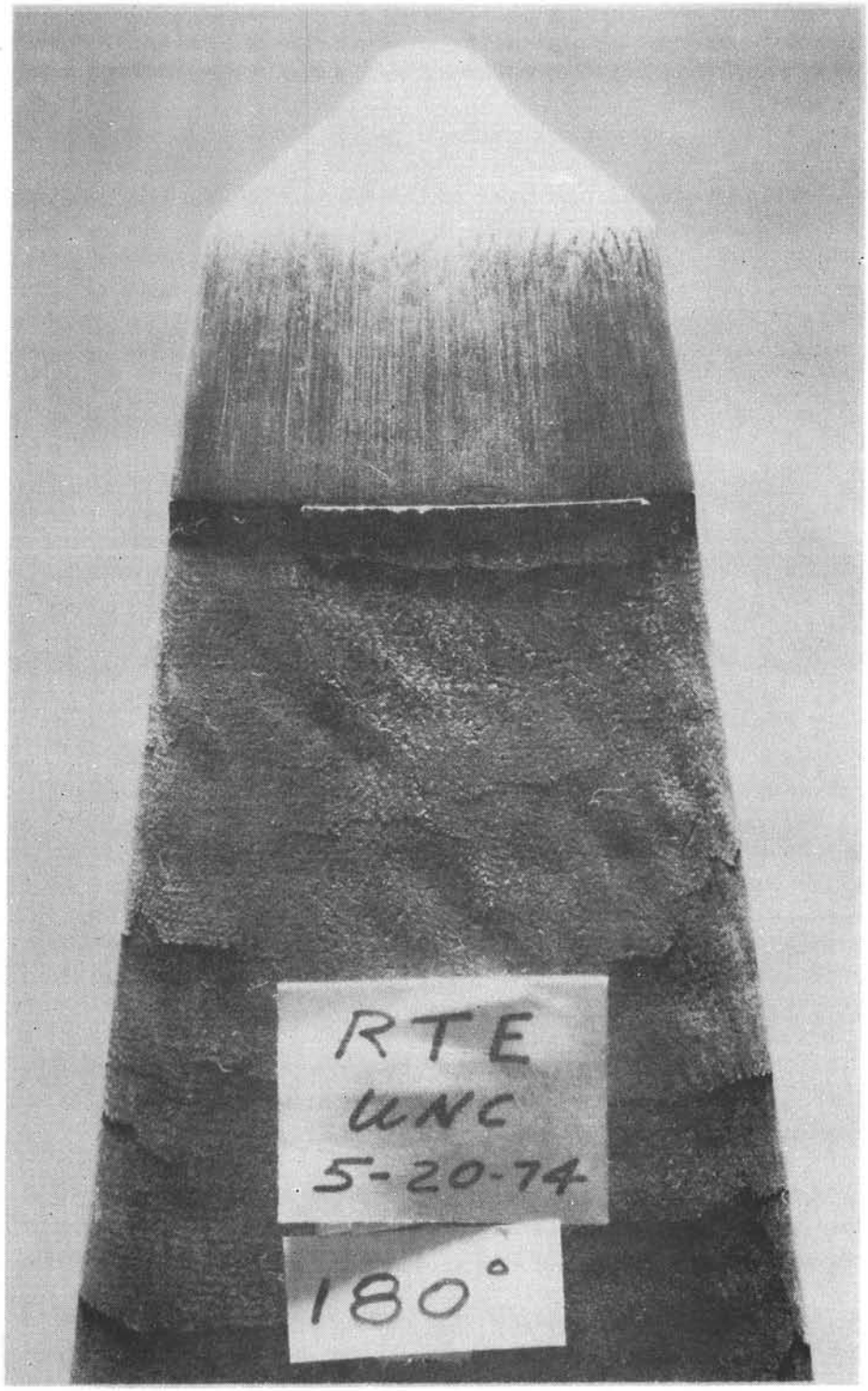

Figure 43. Recovered RTE Nosetip (180° Orientation)

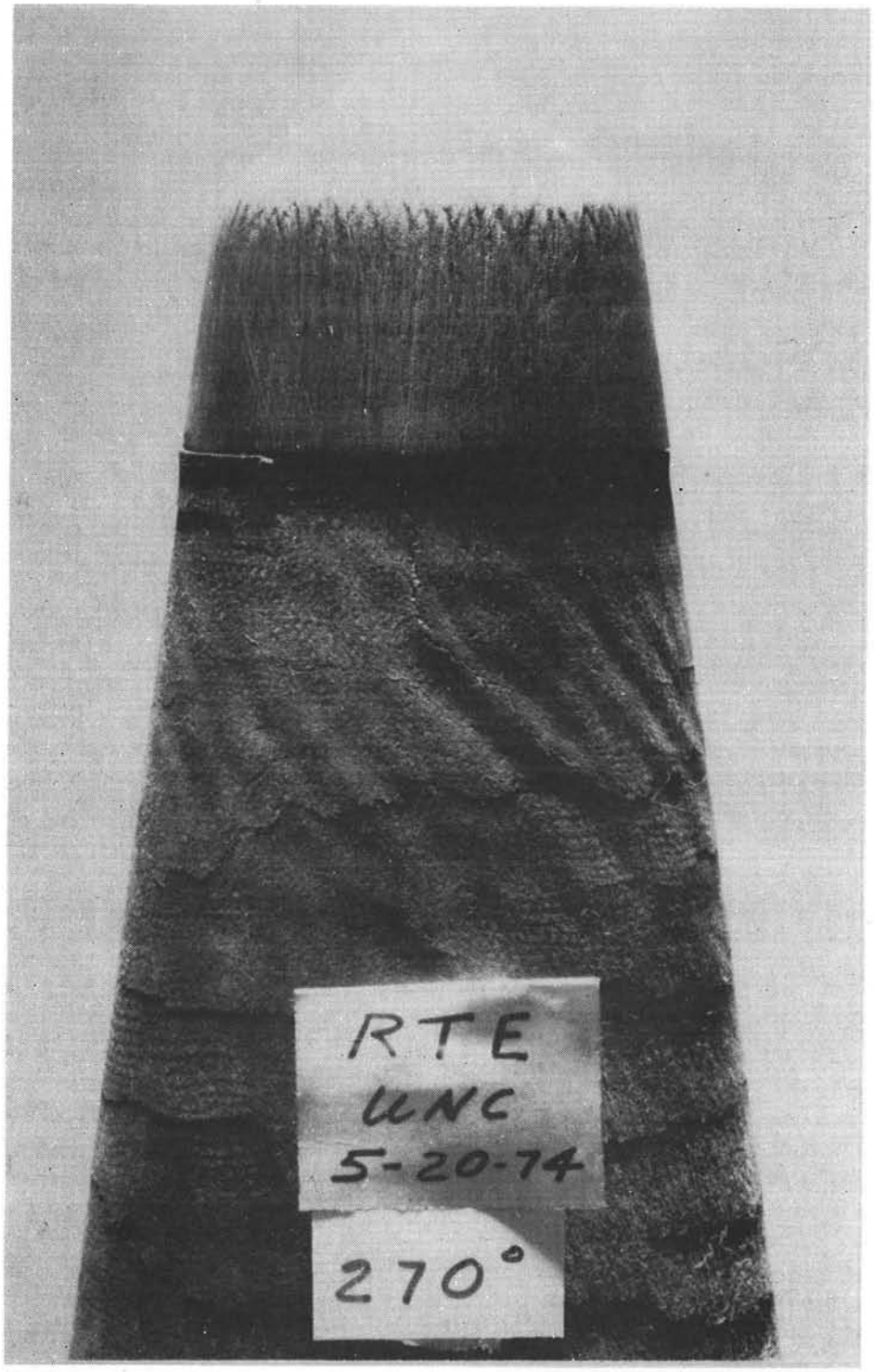

Figure 44. Recovered RTE Nosetip (270° Orientation)

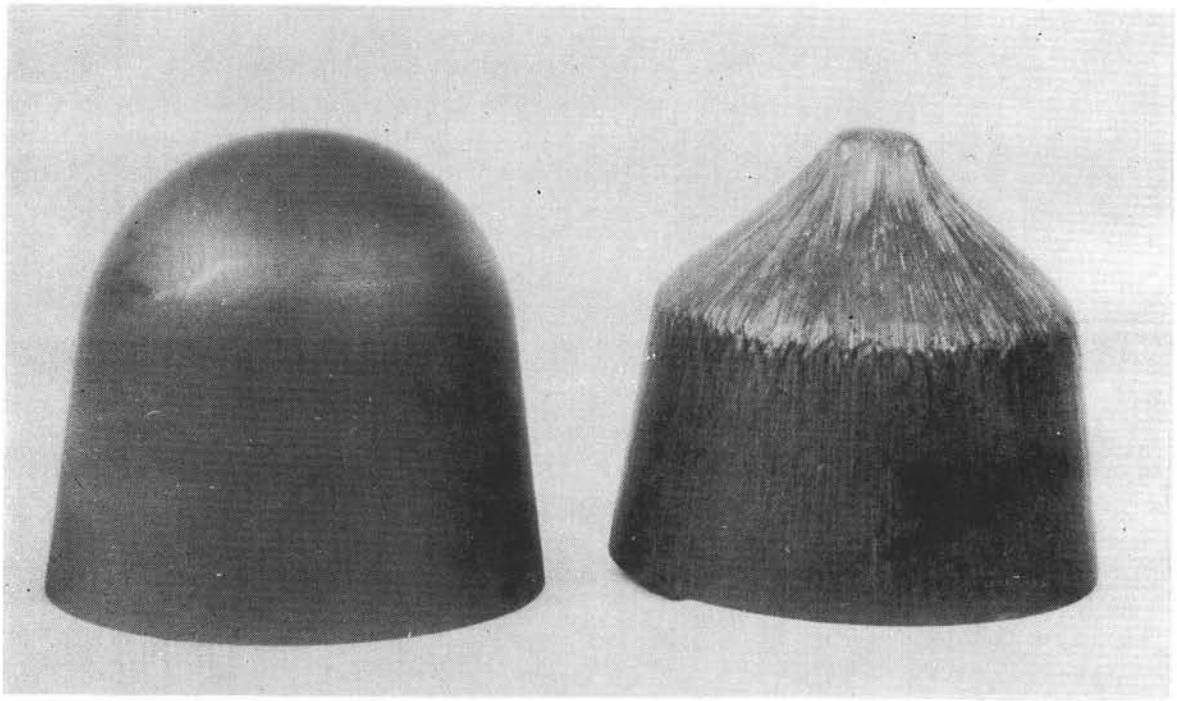

Figure 45. Comparison of Preflight and Postflight Nosetip

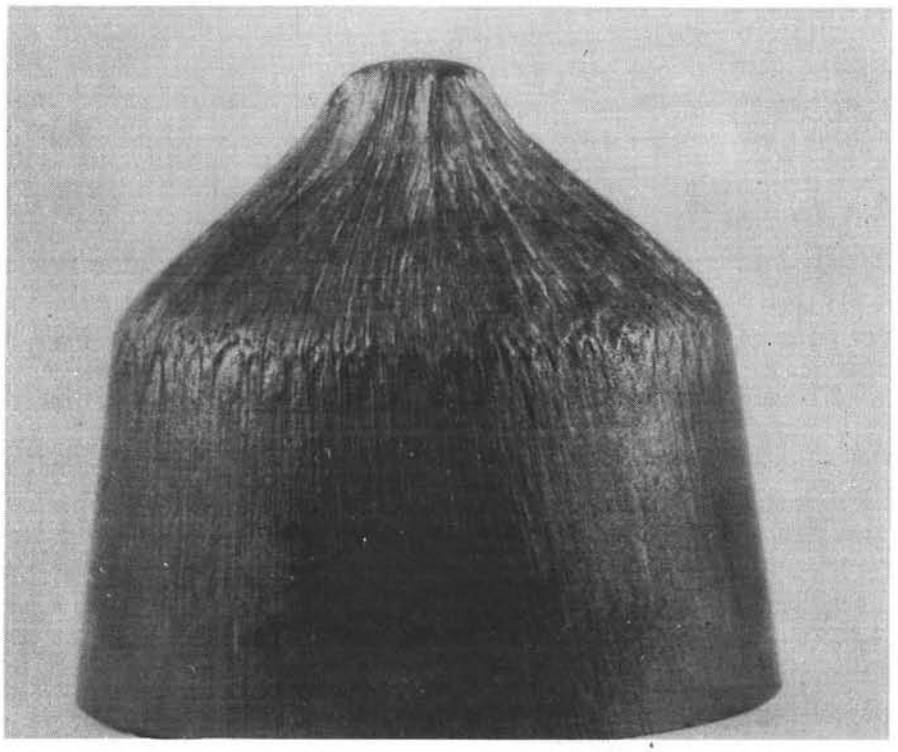

Figure 46. RTE Recovered Nosetip Showing Longitudinal Groove Patterns

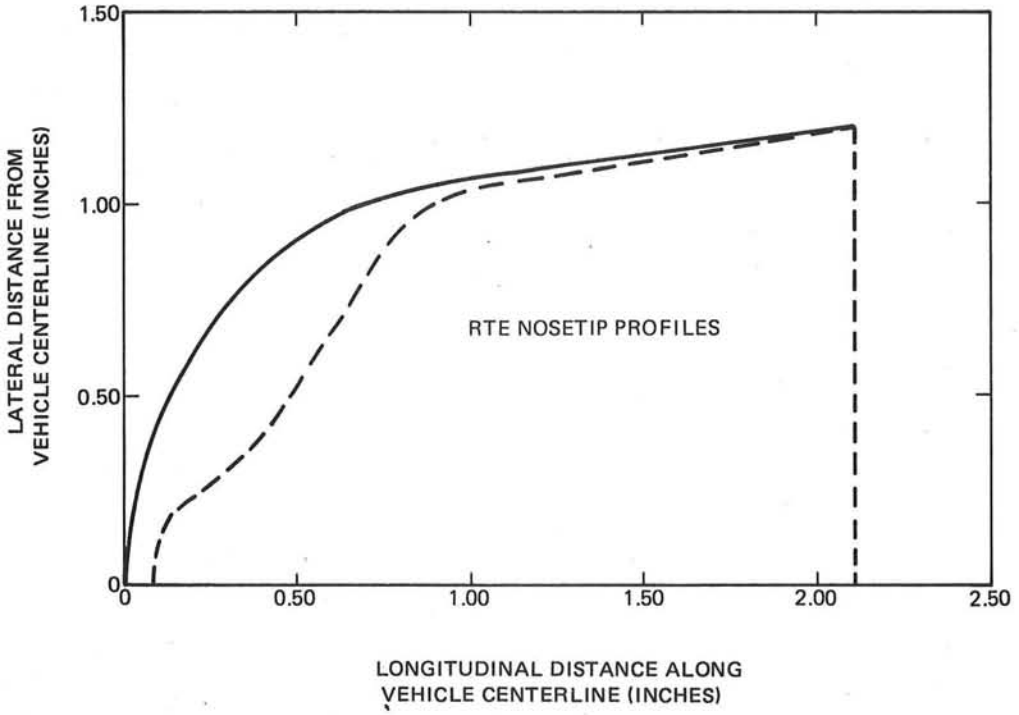

Figure 47. Preflight and Postflight Nosetip Profiles

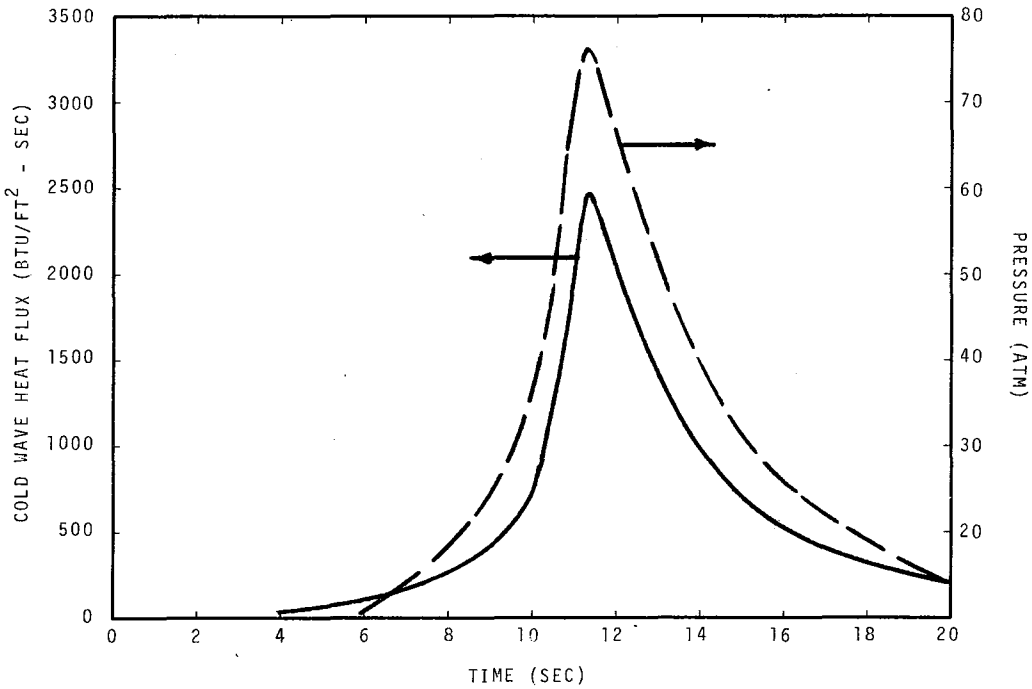

Figure 48. Stagnation Point Pressure and Cold Wall Heat Transfer

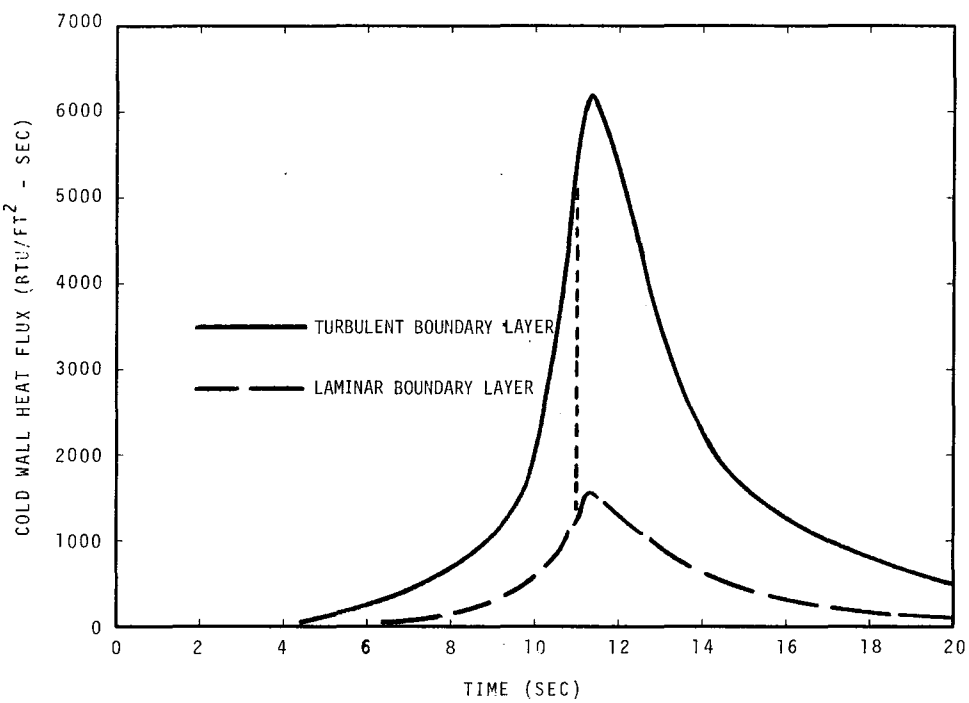

Figure 49. Laminar and Turbulent Cold Wall Heat Flux (0.75 Inch Downstream of Stagnation Point)

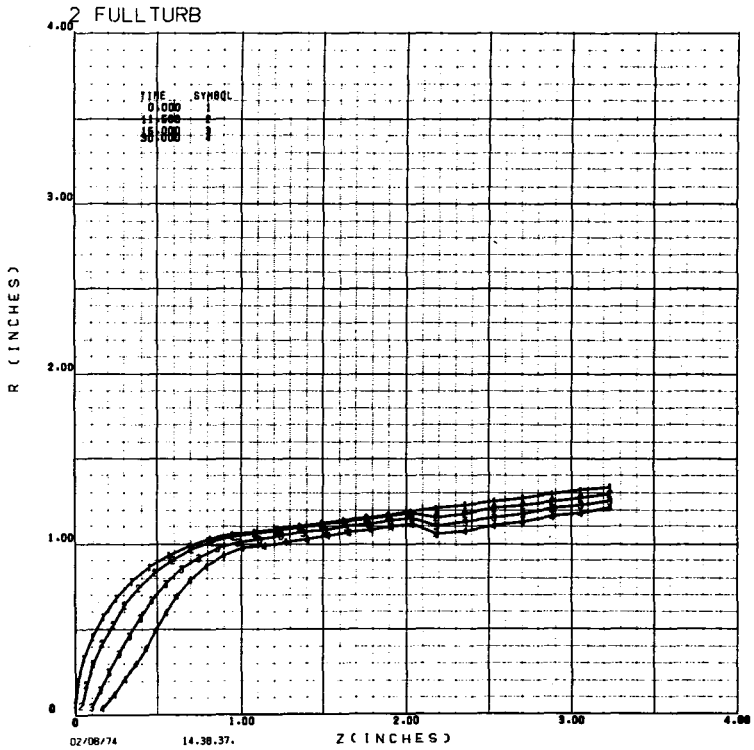

Figure 50. Calculated Nosetip Surface Profiles for Fully Turbulent Flow

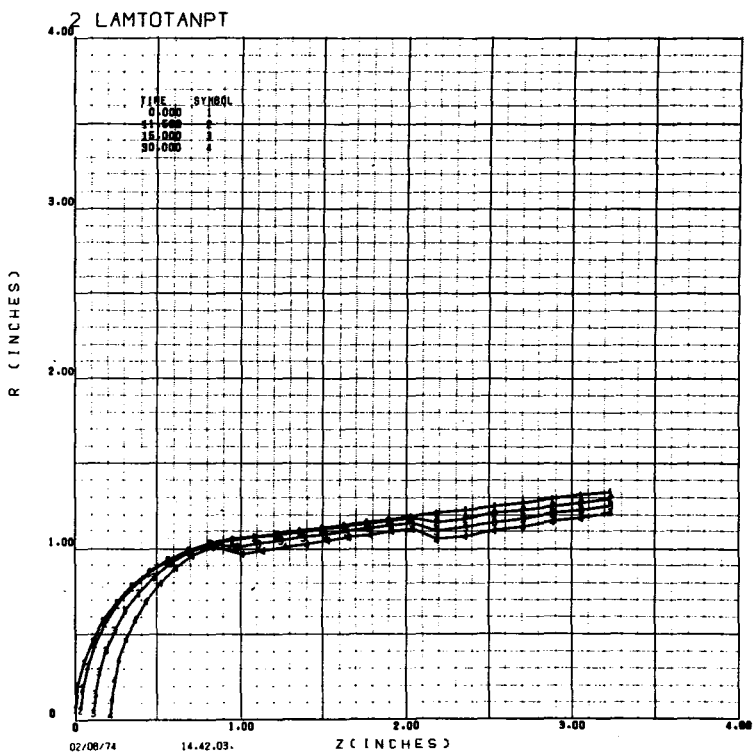

Figure 51. Calculated Nosetip Surface Profile for Case of Laminar Flow to the Tangency Point and Turbulent Flow Aft of the Tangency Point

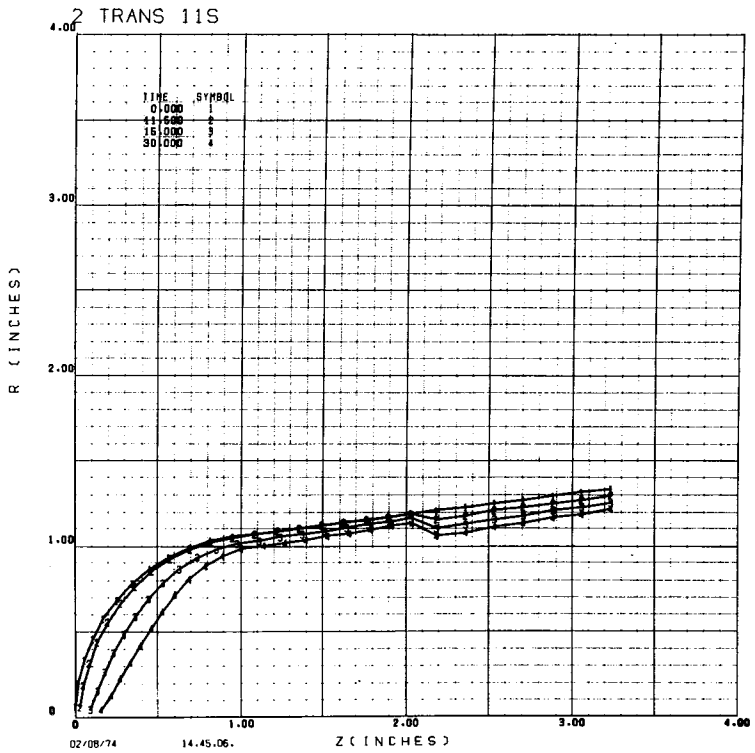

Figure 52. Calculated Nosetip Surface Profile for Case of Delayed Boundary Layer Transition (Transition from Fully Laminar to Fully Turbulent Flow at T≈11 Seconds From Launch)

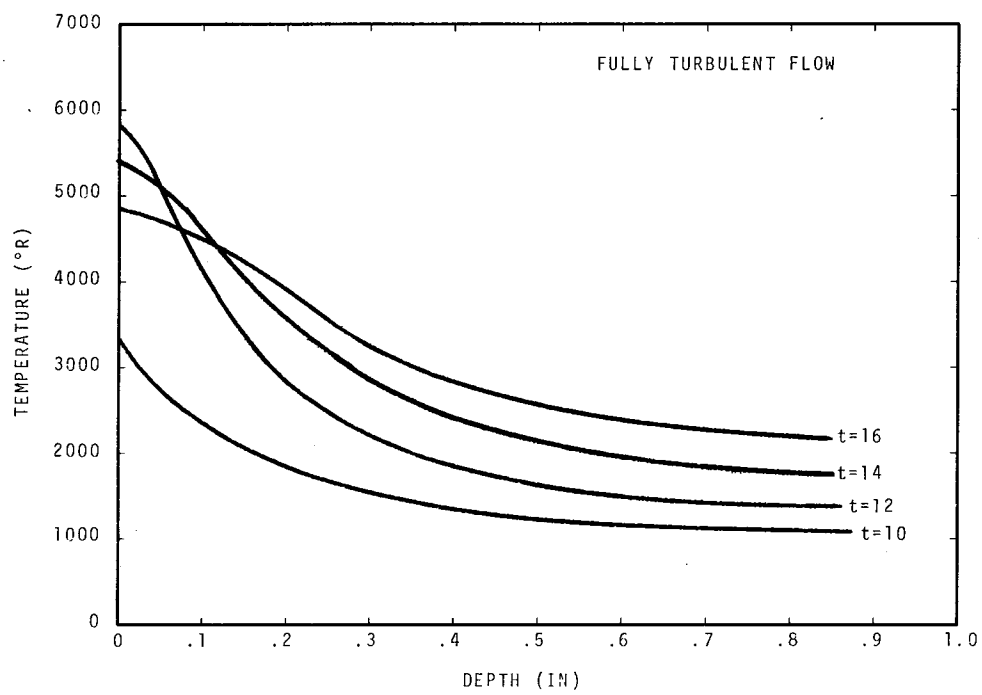

Figure 53. Temperature Distribution Along Nosetip Centerline for Fully Turbulent Flow

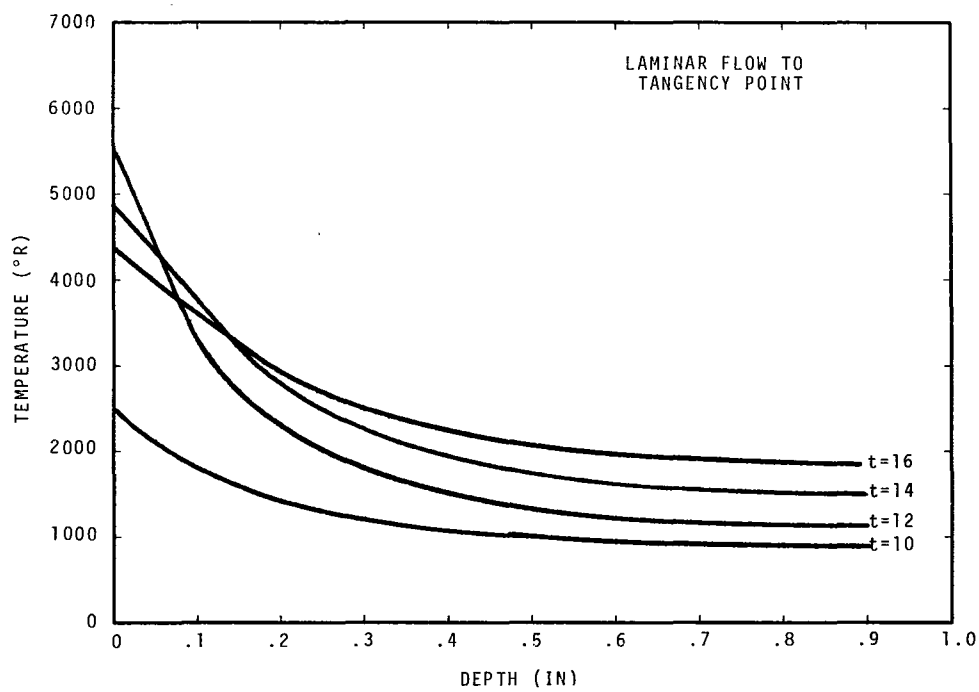

Figure 54. Temperature Distribution Along Nosetip Centerline for Case of Laminar Flow to the Tangency Point and Turbulent Flow Aft of the Tangency Point

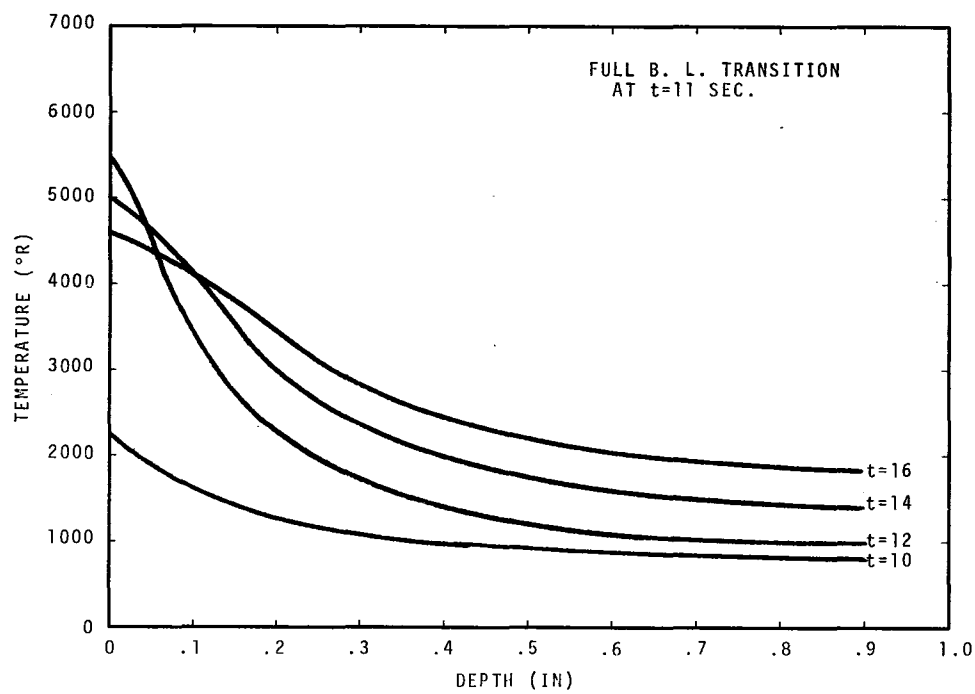

Figure 55. Temperature Distribution Along Nosetip Centerline for Delayed Boundary Layer Transition (Transition from Fully Laminar to Fully Turbulent Flow at T=11 Seconds From Launch)

As a check on the ASTHMA in-depth conduction calculation, the COUPLE[36] code was used to reevaluate the nosetip in-depth thermal response. COUPLE, a finite-element conduction code, cannot account for ablation, so the surface temperature histories determined in the ASTHMA calculations were used as boundary conditions and the surface recession was neglected. The results of the COUPLE calculations (summarized in Reference 37) were used for the thermal stress analysis, since it is believed that the more sophisticated nature of the COUPLE conduction analysis results in a more reliable estimate of the internal thermal response.

Nosetip Thermal Stress Analysis

The analysis of the RTE plug nosetip used thermal data from the three different trajectories calculated in the previous section (fully turbulent, initially laminar with transition to turbulent at 11 seconds, and continuously laminar on the forward radius changing to turbulent at the tangency point). The detailed analysis is presented in Reference 38. Only the final results are given here.

Using a straightforward maximum stress failure approach, the fully turbulent trajectory (the worst case analyzed) with the temperature distribution shown in Figure 56 gives a peak stress of 4553 psi (circumferential) and 3777 psi (axial) at a point 0.74 inch from the front surface, as seen in Figure 57, with a temperature of 1731°F, 13.5 seconds after launch. While this level is above room temperature failure stress levels, the higher temperatures increase the ultimate stress, and a linear interpolation between 2σ values at 1500°F and at 2000°F (Reference 39) gives an ultimate tensile strength value at 1731°F of 4636 psi (circumferential) and 4079 psi (axial). The desired margin of safety was thus provided.

While this thermal stress failure analysis may appear sufficient, it may not prove adequate in a strain-driven problem. A strain failure analysis for temperature lower than 2500°F gives, for the fully turbulent trajectory at 13.5 seconds after launch, a peak strain state of 0.24 percent in the axial direction and 0.18 percent in the radial direction at 0.93 inch from the front surface, with a temperature of 1456°F as seen in Figure 58. This condition is well within a 95 percent probability of triaxial tension failure criteria.

While peak strains were being considered, an interesting biaxial state of strain was found. For the trajectory which turns from laminar to turbulent at 11 seconds (immediate jump to peak heating rate) at a temperature of 3556°F, there exists a biaxial state of strain in a ring section about 0.15 inch behind the front surface at a radius of 0.43 inch. This state consists of 0.30 percent strain normal to the surface and a compressive strain of about -0.39 percent parallel to the surface. Little is known about failure in this type of strain state, but as the plug gets hotter, the strain state improves.

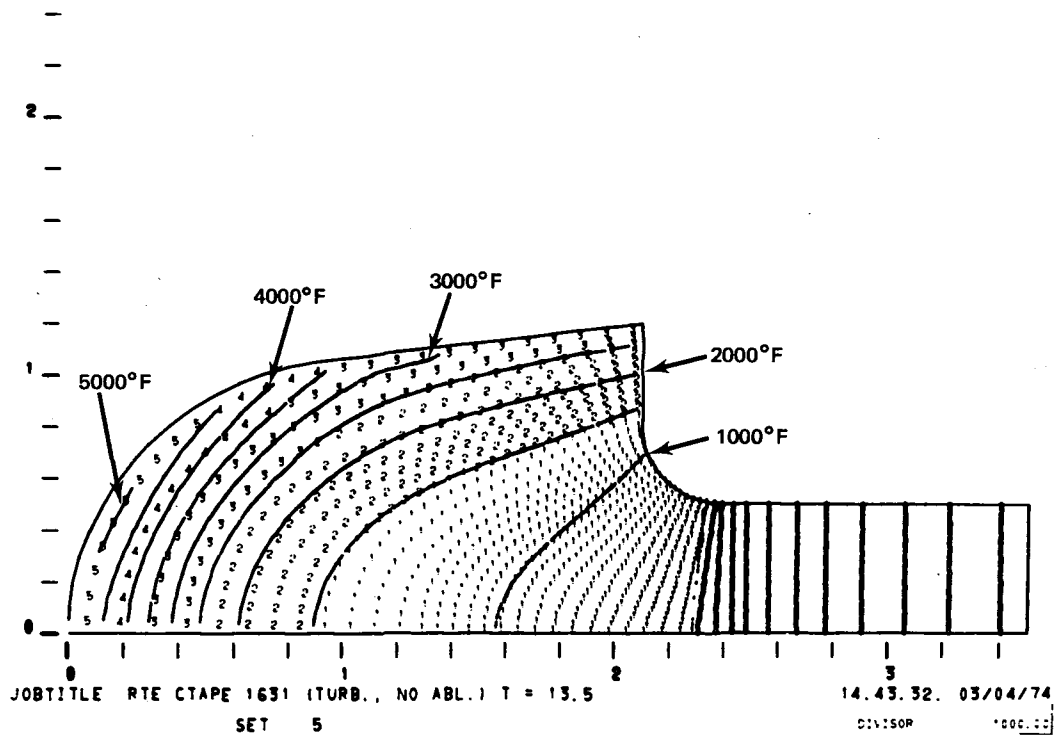

Figure 56. RTE Nosetip Temperature Profile

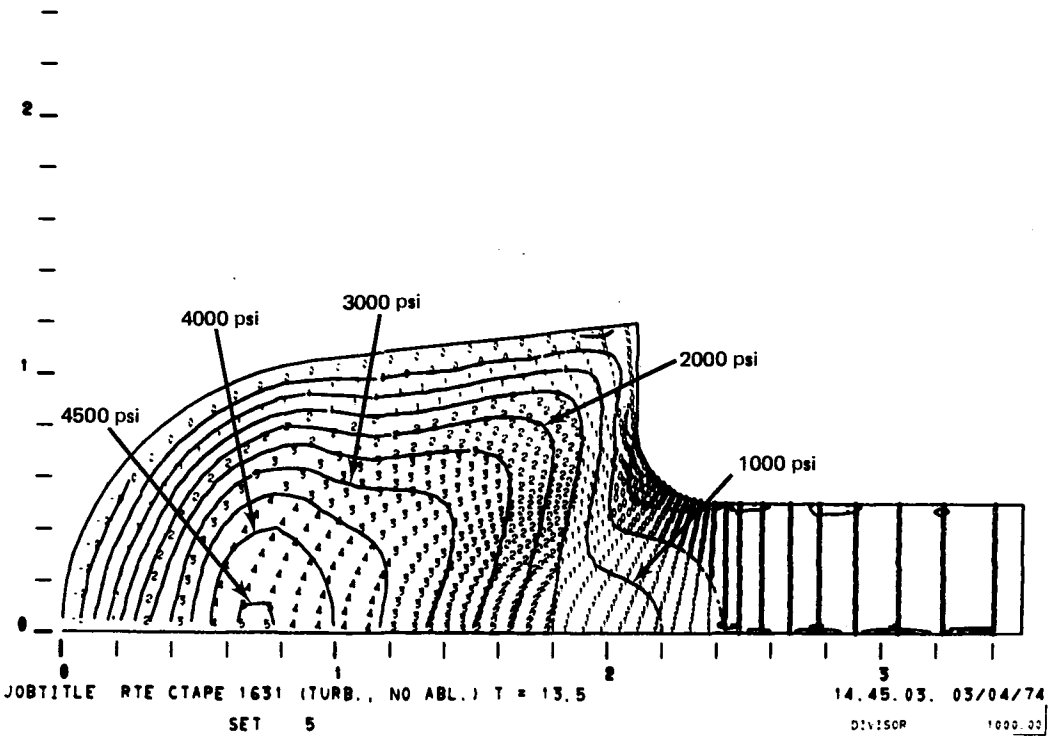

Figure 57. RTE Nosetip Stress Profile

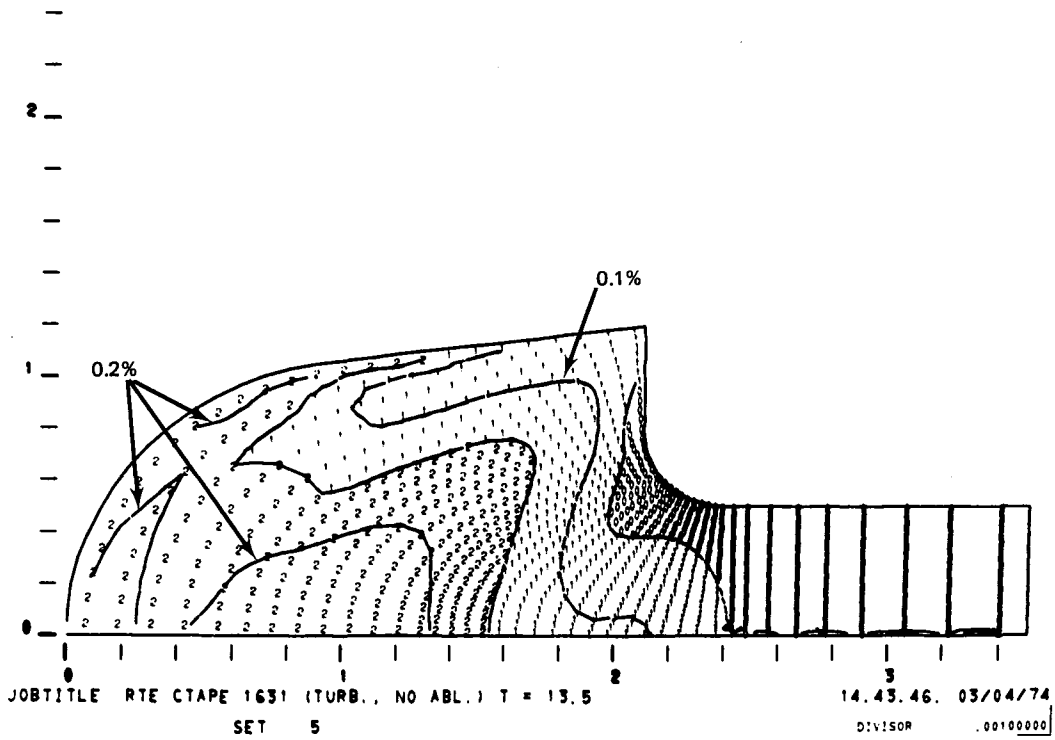

Figure 58. RTE Nosetip Strain Profile

REFERENCES

1. R. Larmour, "Heatshield Tape Lap Effects on Roll Rate Performance," Chapter 13 of Proceedings of the Symposium on Ballistic Re-Entry Vehicle Roll Control, Aerospace Corp. Report TOR-0074 (4450-15)-2, August 1973.

2. J. K. Kryvoruka and T. T. Bramlette, Heatshield Tape Lap Effects on Re-Entry Vehicle Spin Rate, Sandia Laboratories, SLL-73-0277, August 1973.

3. A. H. Nayfeh and G. G. Wilson, "Impact Point Dispersion Due to Spin Reversal," AIAA Journal of Spacecraft and Rockets, Vol. 7, No. 6, June 1970.

4. D. H. Platus, "A Note on Re-Entry Vehicle Roll Resonance," AIAA Journal, Vol. 5, No. 7, July 1967.

5. C. H. Murphy, "Response of an Asymmetric Missile to Spin Varying Through Resonance," AIAA Paper No. 71-46, AIAA 9th Aerospace Sciences Meeting, New York, January 1971.

6. M. Tobak, "Hypothesis for the Origin of Cross-Hatching," AIAA Journal, Vol. 8, No. 2, February 1970.

7. J. B. McDevitt, "An Exploratory Study of the Roll Behavior of Ablating Cones," AIAA Paper No. 70-562, AIAA Atmospheric Flight Mechanics Conference, Tullahoma, Tennessee, May 1970.

8. E. P. Williams, "Experimental Studies of Ablation Surface Patterns and Resulting Roll Torques," AIAA Paper No. 69-180, AIAA Aerospace Sciences Meeting, New York, January 1969.

9. Communication from L. Hull, Lockheed Missiles and Space Corporation, Sunnyvale, CA (to be published).

10. P. B. Wells and D. W. Prather, Surface Induced Roll Torques from TWCP Heatshields, Kaman Sciences Corporation, Colorado Springs, Colorado, K-73-678, November 1973 (and private communication).

11. R. B. Pope and G. G. Wilson, Surface Anomalies at the Tape Laps of Ablated Carbon Phenolic, Sandia Laboratories, Albuquerque, SLA-73-0992, December 1973 (and private communication).

12. J. K. Cole, H. W. Church, B. W. Marshall and L. R. Rollstin, Test Report for SAMS Rain-Erosion Flights 3, 4, and 5, Sandia Laboratories, Albuquerque, SLA-73-0565, October 1973.

13. Internal Communication from I. Auerback, 5628, "Nosetip Selection and Nondestructive Evaluation of Graphite Stock for the RTE Vehicle," November 20, 1973.

14. H. D. Sorenson, "RTE Telemetry System Development Report," Sandia Laboratories, Livermore, March 1974.

15. A. J. Korbe, Tonopah Test Range Facilities and Operating Procedures, Sandia Laboratories, SC-M-64-581, July 1964.

16. Internal Communication from L. R. Myers, 8412, "Sandia Range Instrumentation Order for the RTE/TATER Test Vehicle (Test No. SLL-5896-6 and R-423480)," February 1, 1974.

17. L. R. Myers, "Hazards Information and Applicable SOP's for RTE/TATER Test (SLA R-42380, SLL-5896-6)," Sandia Laboratories, March 1974.

18. Internal Communication from L. R. Rollstin, 5624, "RTE-TATER Trajectory," January 10, 1974.

19. Internal Communication from L. R. Rollstin, 5624, "RTE Postflight Trajectory (R-36 Radar)," May 1974.

20. Data Reduction Report (Trajectory) Sandia Test R423480, Sandia Laboratories, Albuquerque, May 1974.

21. J. K. Kryvoruka, A Formulation of the Equations of Motion for Flight Vehicles with Semi-Passive Roll Control Systems, Sandia Laboratories, SCL-RR-720007, April 1972.

22. J. K. Kryvoruka, SPINFIN: A Computer Program for Trajectory Simulation of Flight Vehicles with Semi-Passive Roll Control Systems, Sandia Laboratories, SCL-DR-720025, January 1972.

23. An Investigation of the Static and Dynamic Stability of Several Re-entry Body Shapes, Lockheed Missiles and Space Company, TM 55-21-78, January 1966.

24. R. V. Owens, Aerodynamic Characteristics of Spherically Blunted Cones at Mach Numbers from 0.5 to 5.0, NASA TND-3088, December 1965.

25. E. L. Clark and R. E. Tate, Static and Dynamic Wind Tunnel Tests of Halbred Configurations at Mach Numbers of 2 to 11, Sandia Laboratories, SC-DR-66-634, October 1966.

26. J. K. Kryvoruka, Analysis of the Motion of Free-Flight Missiles from Body Fixed Sensors, Sandia Laboratories, Livermore, SCL-RR-70-41, May 1970.

27. R. S. Eikenberry, Analysis of the Angular Motion of Missiles, Sandia Laboratories, Albuquerque, SC-CR-70-6051, April 1970.

28. J. D. Nicolaides, Missile Flight and Astrodynamics, BUWEPS TN-100A, Bureau of Naval Weapons, 1961.

29. G. T. Chrusciel and L. D. Hull, "Theoretical Method for Calculating Aerodynamic Characteristics of Spherically Blunted Cones," AIAA Paper No. 68-674, AIAA Fluid and Plasma Dynamics Conference, June 24-26, 1968.

30. E. F. Blick and J. E. Francis, "Spherically Blunted Cone Pressure Distribution," AIAA Journal, Vol. 4, No. 3, March 1966, pp. 547-549.

31. W. T. Ashurst, HANDY--A Computer Program for Predicting Supersonic Aerodynamic Characteristics of Sphere-Cone and Sphere-Cone-Cylinder-Flare Axisymmetric Bodies at Small Angles-of-Attack, Sandia Laboratories, SCL-DR-70-25, March 1970.

32. E. C. Lemmon, T. T. Bramlette, and H. W. Coleman, SCORCH--A Computer Code for Calculating Aerodynamic Heating on Reentry Vehicles and Control Surfaces, Sandia Laboratories, SLL-73-0248, July 1973.

33. F. U. Bolek and D. F. McVey, Operating Instructions for Charring Material Ablation Code, SC-M-66-377, Sandia Laboratories, Albuquerque, August 1966.

34. C. B. Moyer, B. F. Blackwell, and P. C. Kaestner, A Users Manual for the Two-Dimensional Axisymmetric Transient Heat Conduction Material Ablation Computer Program, Sandia Laboratories, SC-DR-70-150, December 1970.

35. G. F. Wright, Jr., Preflight Thermal Analysis of the Graphite Nosetip for the TATER Rocket System, Sandia Laboratories, SLA-73-0621, September 1973.

36. E. C. Lemmon, COUPLE--A Pseudo Finite Element Conduction Code for the Transient Thermal Response of Axisymmetric or Plane Anisotropic Materials, Sandia Laboratories, SCL-RR-720324, December 1972.

37. R. M. Green, RTE Nosetip Thermal Analysis, Sandia Laboratories, Livermore, to be published.

38. L. E. Voelker, RTE Nosetip Thermal Stress Analysis, Sandia Laboratories, Livermore (to be published).

APPENDIX A--RTE HEAT SHIELD CONSTRUCTION

The thermal shield was constructed of tape-wrapped carbon phenolic (TWCP). The steps used in manufacture of the tape are illustrated in Figure A-1. In this process, the heat shield material is made from phenolic-impregnated carbon cloth. The material is cut on a 45-degree bias in order to maximize the stretch capability of the cloth. The resulting trapezoidal sheets are overlapped and sewn together as illustrated, thus forming rolls which are approximately 40 yards long and 32 inches wide. These have diagonal laps which run at an angle of 45 degrees to the tape and appear every 44 inches. The rolls are then run through slitting machines to produce two-inch-wide tapes which are used to construct the heat shield in the manner shown in Figure A-2. The cloth is wrapped around a conical mandrel to produce the 20-degree layup shown. Note that the overlapping seams (tape joints) have a 45-degree orientation relative to a longitudinal ray along the RV surface. The wrapped shield is illustrated schematically in Figure A-3. Although not true to scale, the schematic does show the presence of the small tape lap edges resulting from the process. These edges, when exposed, act as small aerodynamic surfaces to produce roll torques.

Tape laps exist throughout the heat shield and have been observed in ultrasonic C-scans of the material. To complete the reentry vehicle construction, the wrapped heat shield is cured and machined. In the curing process, the tape is normally compressed from 0.020 in. to approximately 0.014 in. The resulting outer surface is smooth, with the cavities shown in Figure A-3 being filled in with phenolic. For this case both inner and outer surfaces of the heat shield were machined. With the occurrence of boundary layer transition in the reentry trajectory, the aerodynamic heating becomes sufficient to produce phenolic removal and exposure of the tape lap surfaces. This postulate is consistent with flight test observations which indicate the initiation of roll torque at boundary layer transition.

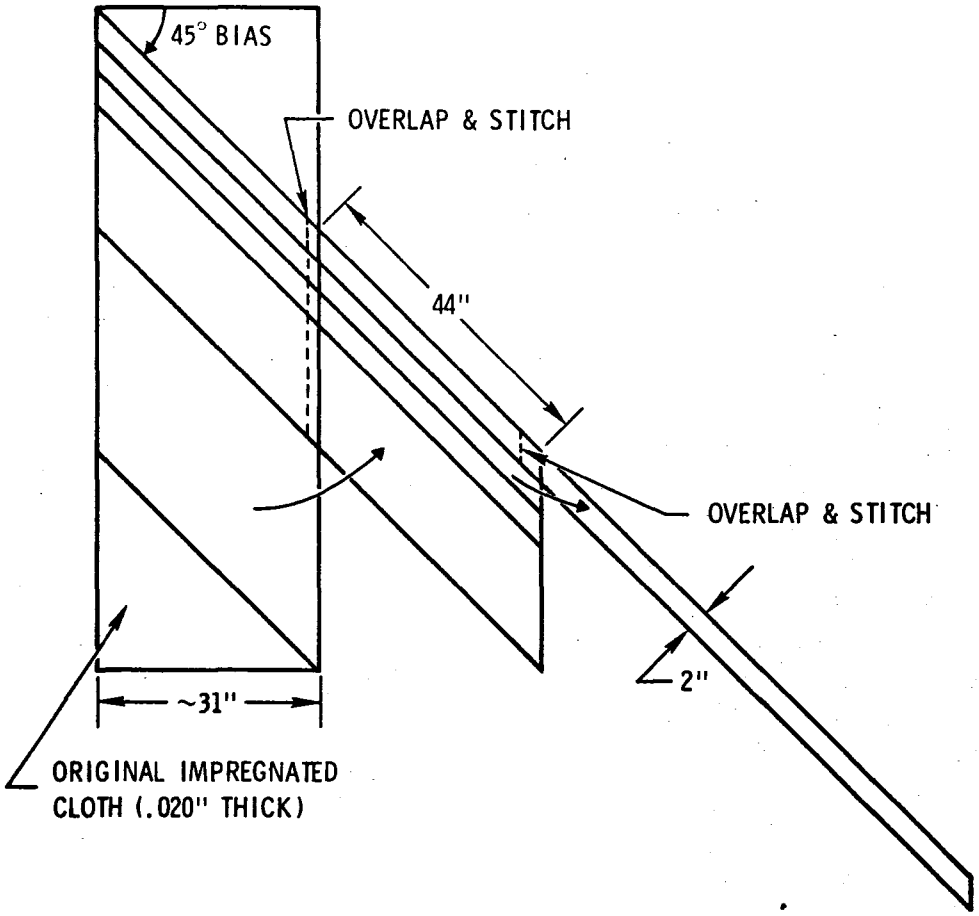

Figure A-1. Construction of Carbon Phenolic Tape

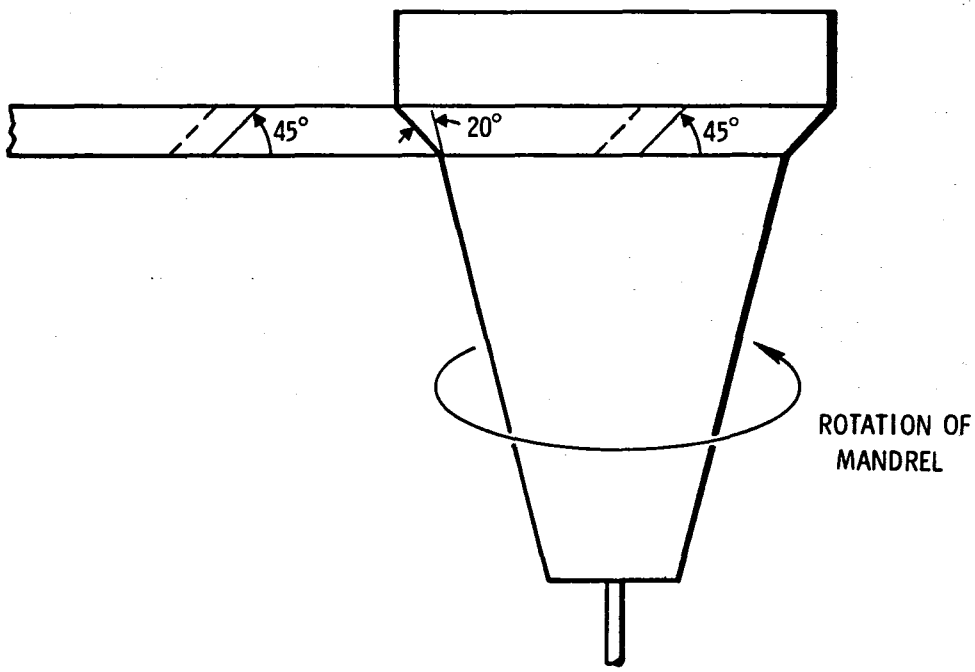

Figure A-2. Heat Shield Wrap Method

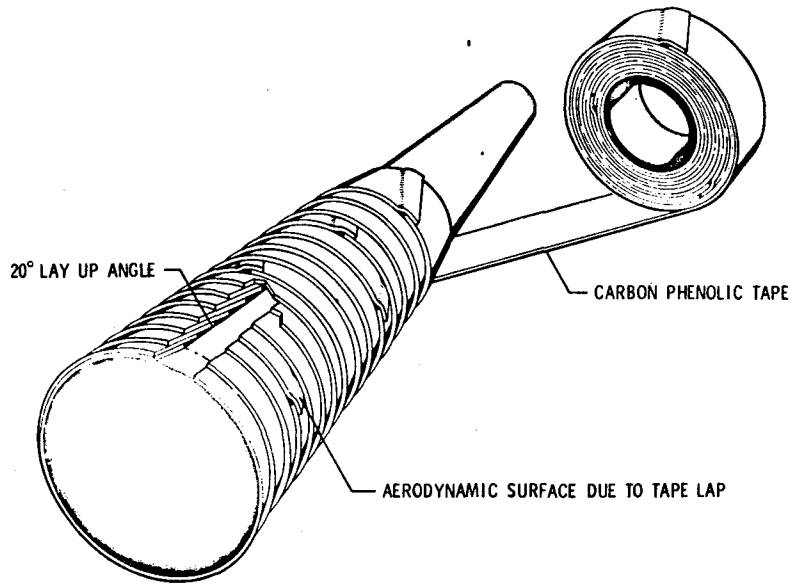

Figure A-3. Schematic of Tape Wrapped Carbon Phenolic (TWCP) Heat Shield Showing Tape Laps

APPENDIX B--RTE TELEMETRY SYSTEM DESCRIPTION

The RTE telemetry was designed to perform (1) as a data acquisition system to monitor and transmit the payload flight dynamic and thermodynamic data and (2) as a fire circuit to provide the proper timing and sequencing for the rocket motors, separation system, and parachute deployment initiators.

Telemetry and Instrumentation

The telemetry system for the RTE flight test program was comprised of a PAM/FM/FM S-band system employed to transmit environmental and aerodynamic data on the reentry body from launch to impact. The telemetry system incorporated two pulse amplitude modulation (PAM) systems, twelve constant bandwidth (CBW) subcarrier oscillators, one 2-watt S-band transmitter, a C-band transponder, a silver zinc battery, and the S- and C-band antenna system. The telemetry system also had the timing and firing circuits necessary for activation of the TATER rocket system and deployment and recovery of the reentry vehicle. The assembled telemetry system is shown in Figure B-1. Figure B-2 is a system block diagram and Figure B-3 is the telemetry system schematic diagram. Interface of the telemetry system with the payload is shown in Figure B-4.

Total data capacity of the PAM systems consists of 43 0-to-5 Vdc channels at 30 SPS and 30 0-to-5 MVdc channels at 30 SPS rate. The VCOs provide 0-to-5 Vdc continuous data channels, 7 of which are capable of 1 kHz response and 5 of which are capable of 2 kHz response. The PAM and VCO channel assignments for the telemetry system are shown in the instrumentation schedule in Table B-I.

The S-band transmitter had a nominal two-watt output with a preset center frequency of 2225.5 MHz and was power-divided into a phased array of three S-band slot antennas located on the aft periphery of the reentry vehicle. The C-band transponder was incorporated into the system for precision radar tracking of the TATER vehicle. This transponder was a pulse type and was preset to receive double pulse interrogations and transmit a double pulse reply in the same frequency band. The transponder frequencies are set to 5690 MHz for receiving and to 5765 MHz for transmitting.

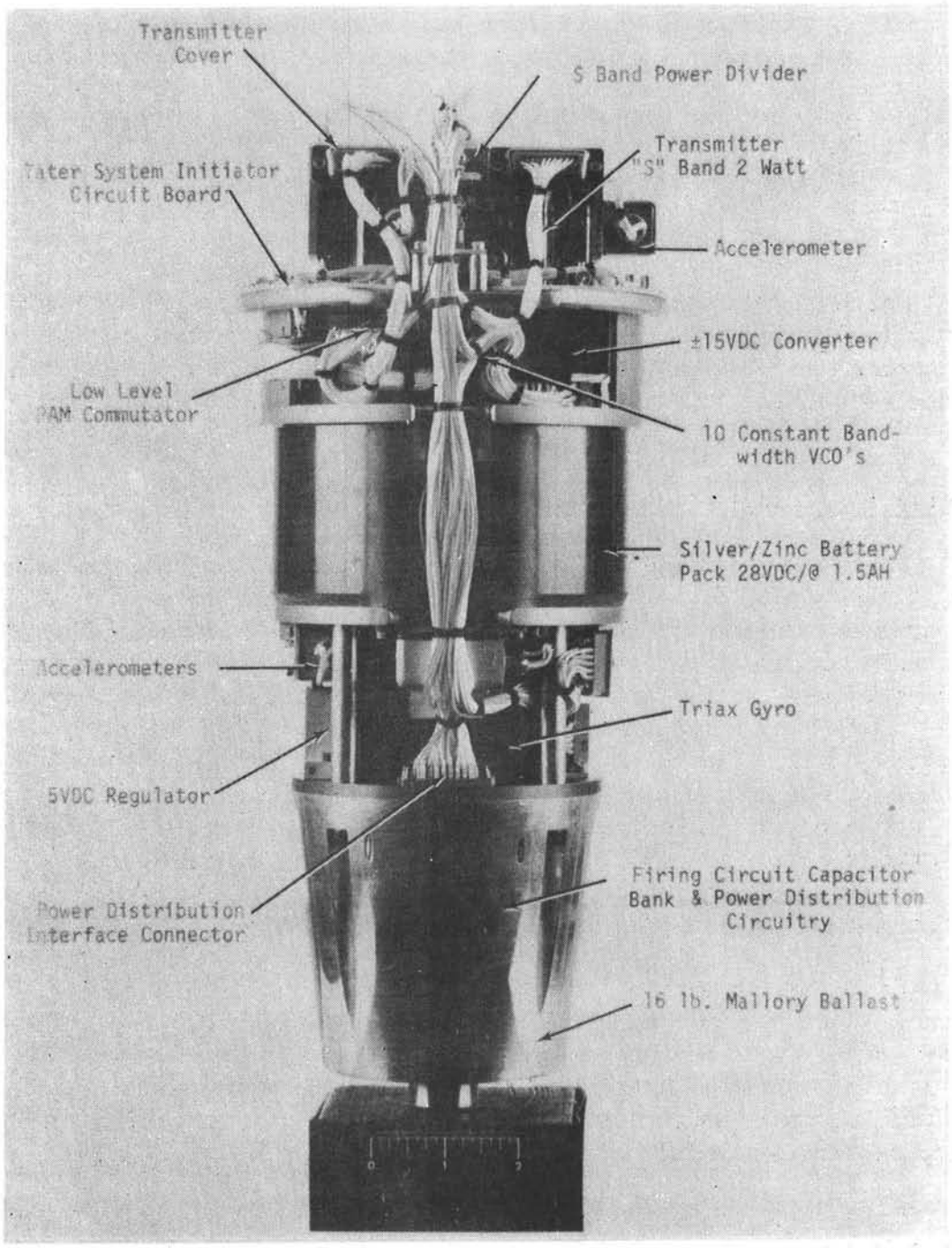

Figure B-1. RTE Telemetry System

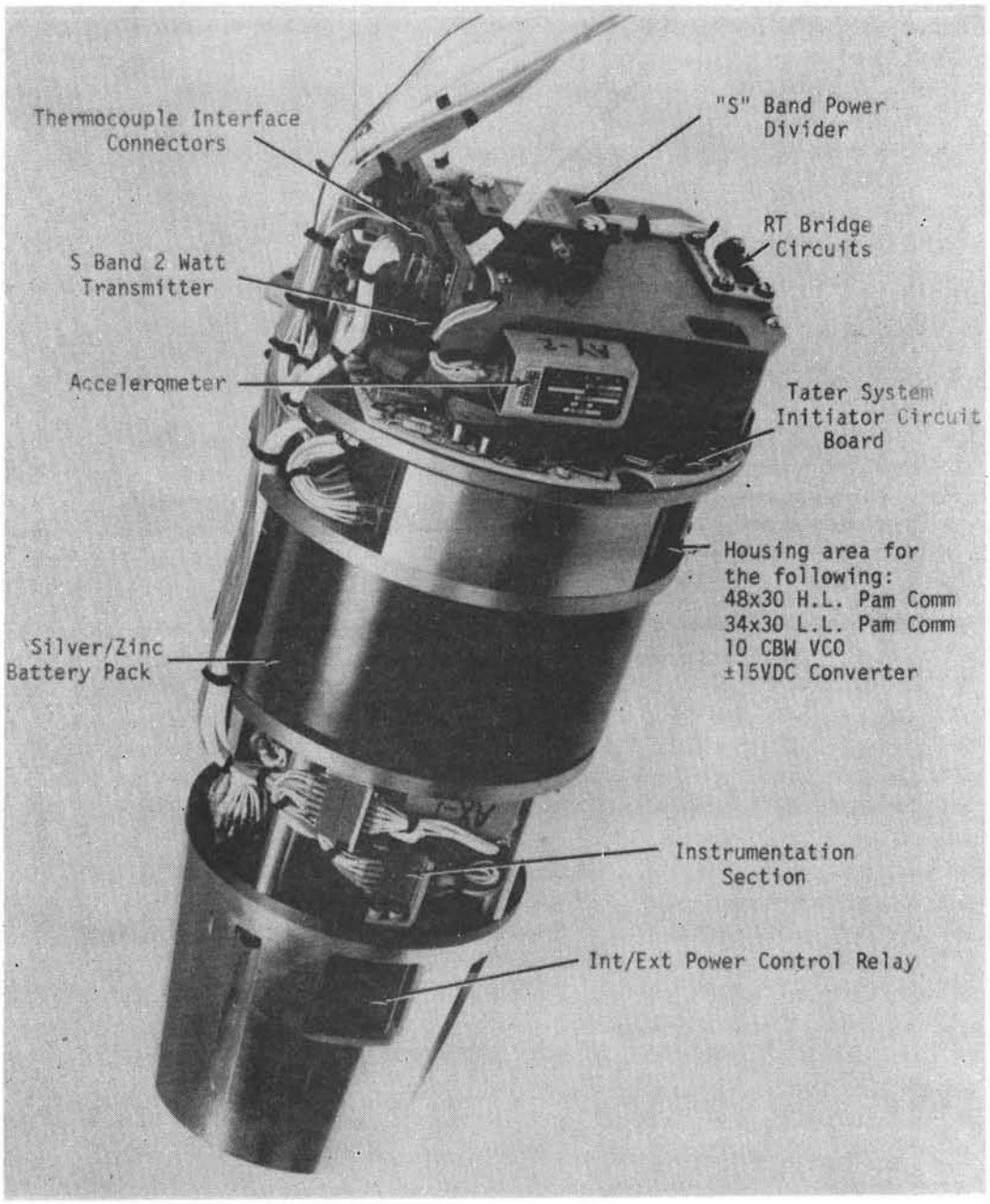

Figure B-1. (continued)

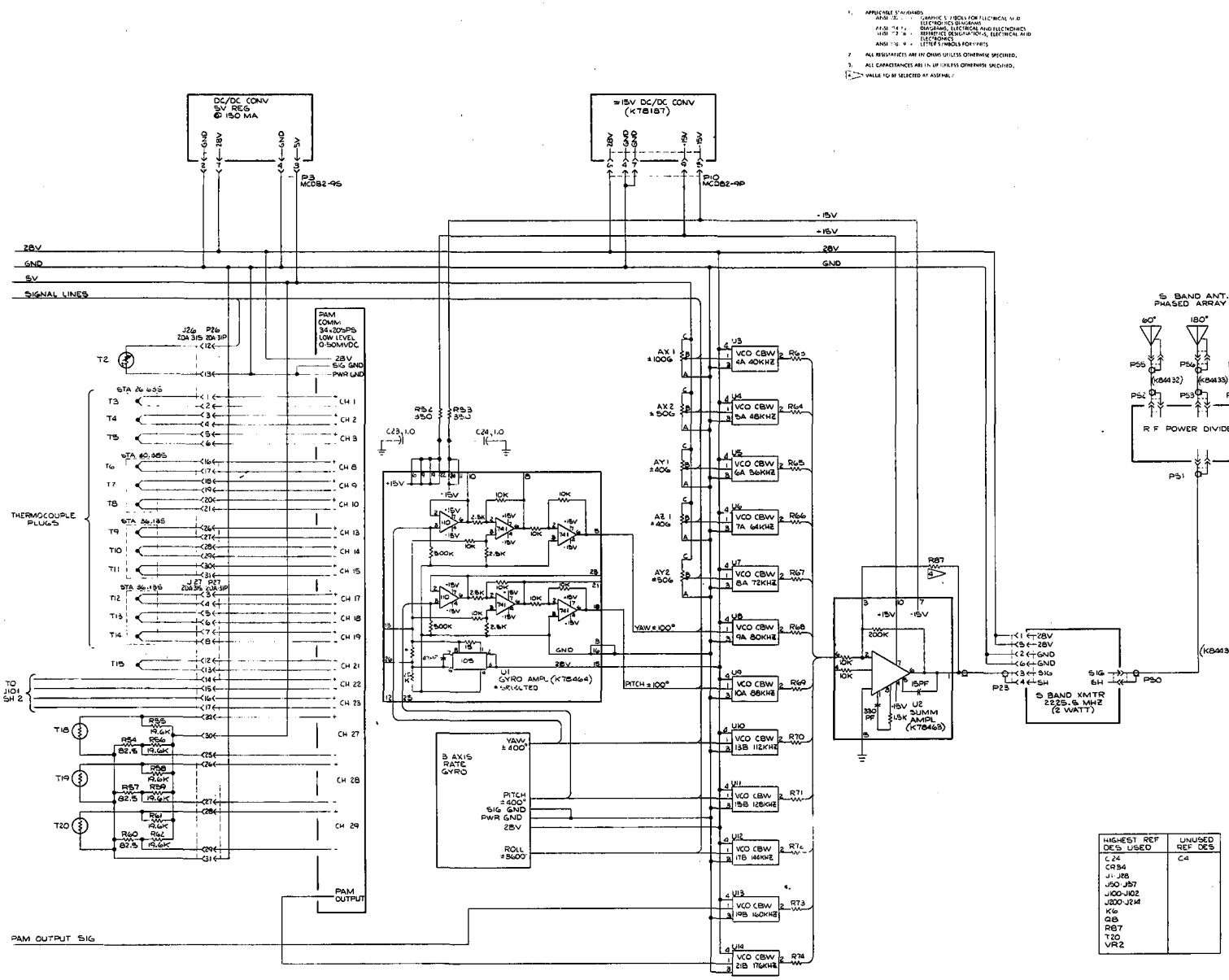

HIGHEST REF DES USED	UNUSED REF DES
C 24	C4
CR34	
J1-J28	
J50-J57	
J100-J102	
J200-J214	
K6	
Q8	
R87	
T20	
VR2	

Figure B-2. RTE Telemetry System Block Diagram

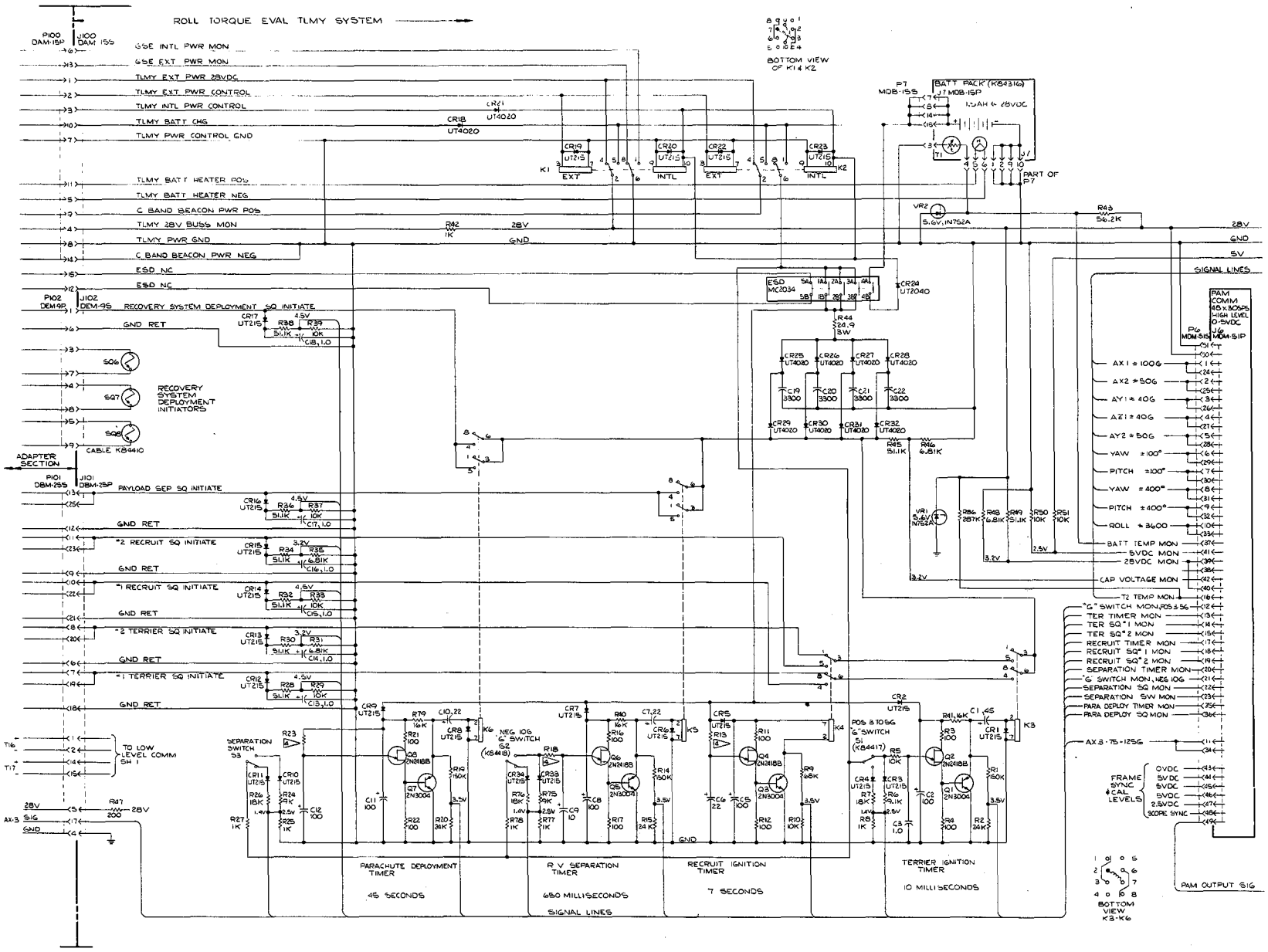

Figure B-2. (continued)

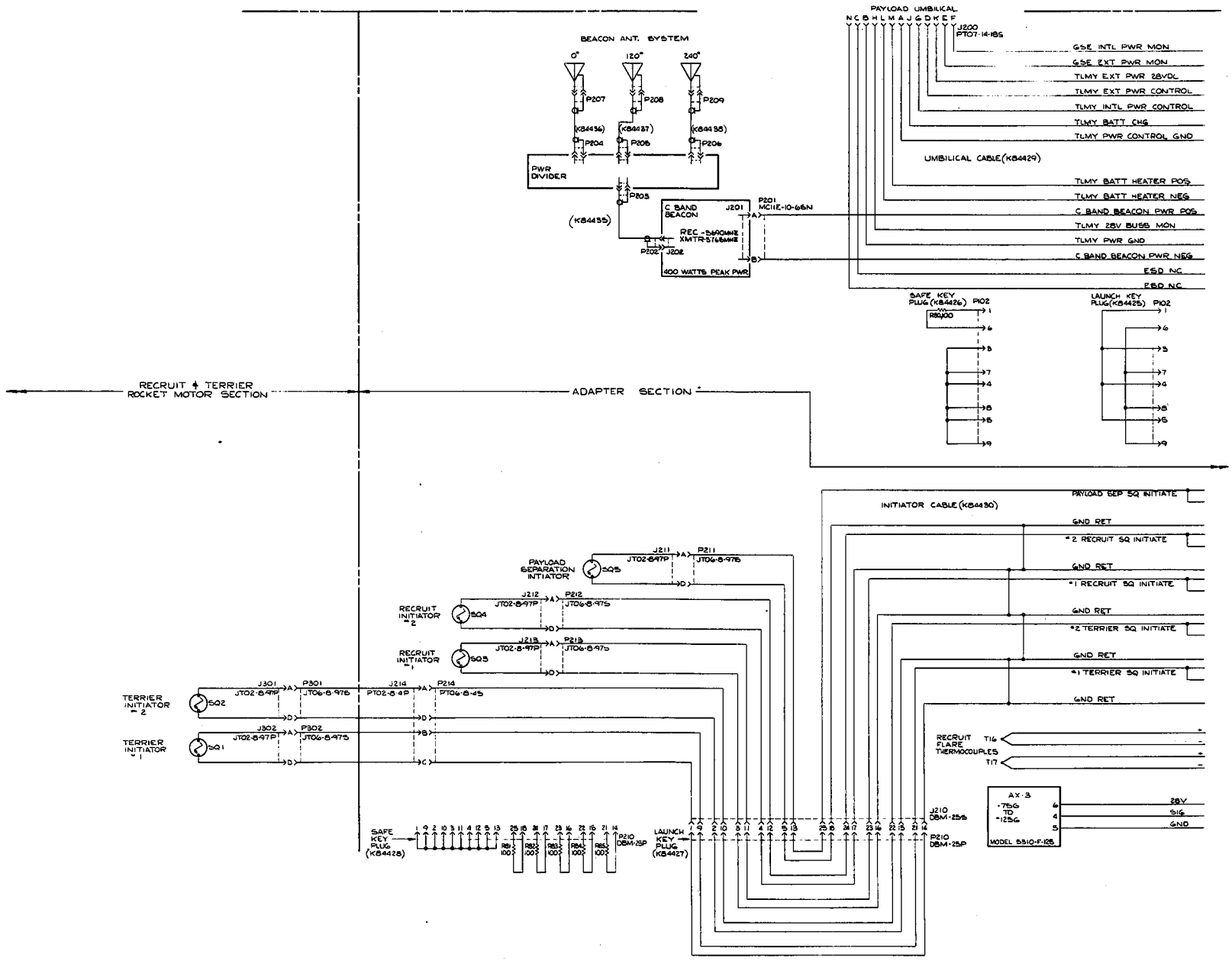

Figure B-2. (continued)

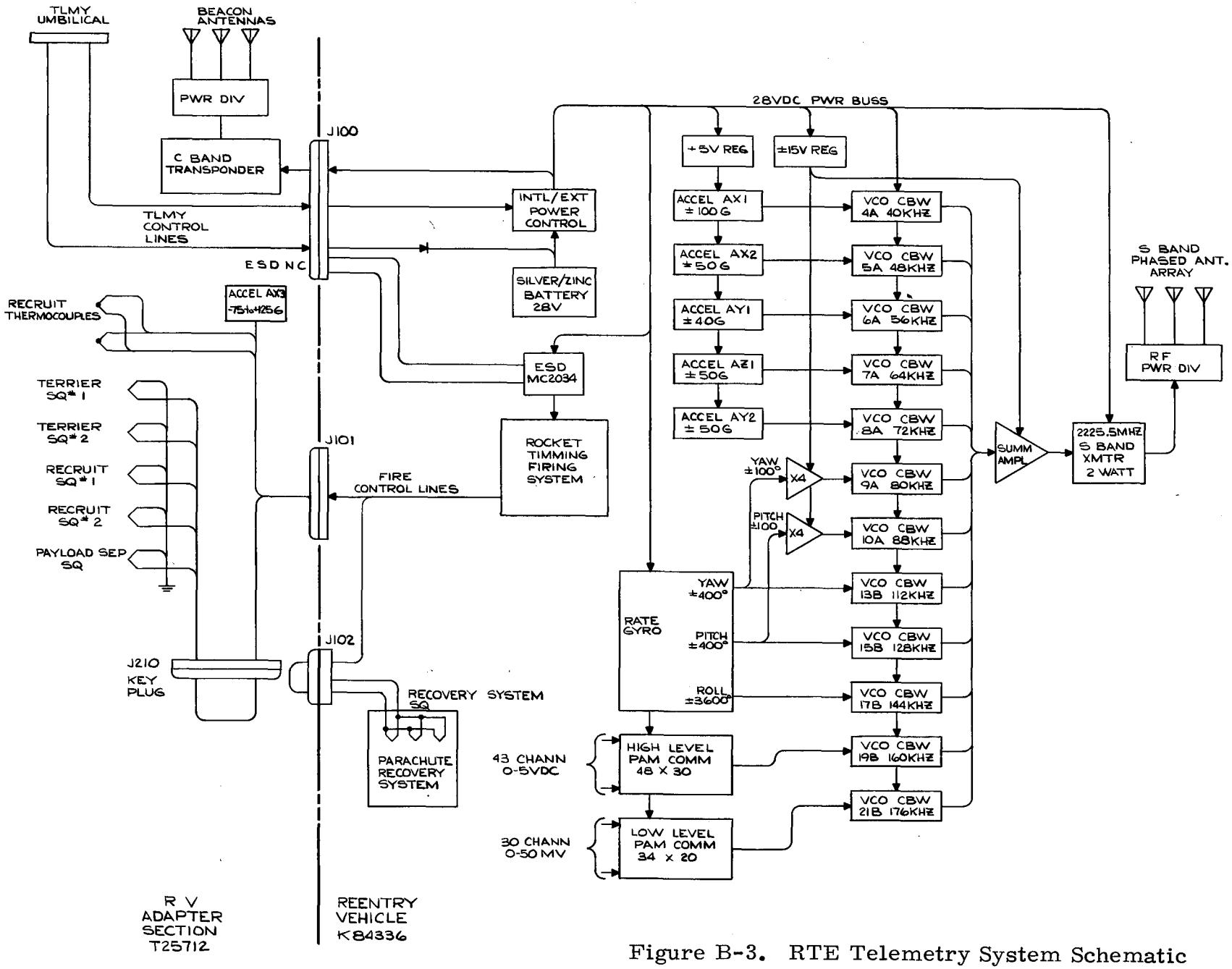

Figure B-3. RTE Telemetry System Schematic

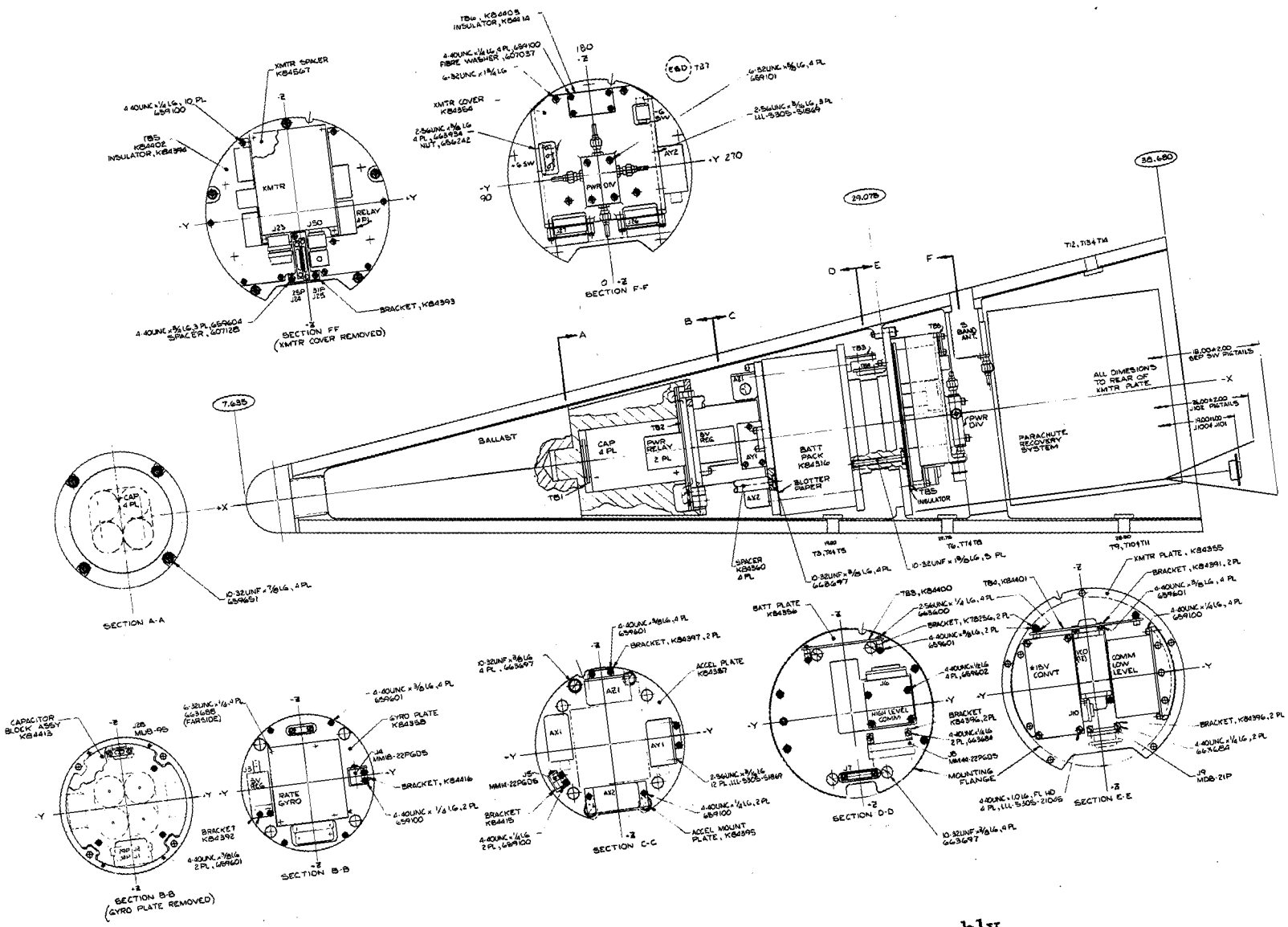

Figure B-4. RTE Telemetry System Assembly

TABLE B-I

RTE INSTRUMENTATION SCHEDULE

TELEMETRY DATA LIST PROPOSAL — 1/23/74

H. D. SORENSEN - 8183 — ROLL TORQUE EVALUATION UNIT (RTEU) — 1 of 3

RTE DATA LIST								TELEMETRY CHANNEL ASSIGNMENT				
ITEM	SYMBOL	MONITOR DESCRIPTION	TEST POINT LOCATION	AGENCY	REQUIRED MEASUREMENT	REQUIRED ACCURACY	REQ. RESP.	VCO CH.	VCO FREQ	PAM CH.	RESPONSE	ACCURACY
1	GYR-1	Roll Rate	STA 15.88	8362	± 3600°/sec	5%	CONT.	17 B	144 kHz	10,33	2 kHz	5%
2	GYP-1	Pitch Rate	STA 15.88		± 400°/sec			15 B	128 kHz	9,32	2 kHz	
3	GYY-1	Yaw Rate	STA 15.88		± 400°/sec			13 B	112 kHz	8,31	2 kHz	
4	GYP-2	Pitch Rate	STA 15.88		± 100°/sec			10 A	88 kHz	7,30	1 kHz	
5	GYY-2	Yaw Rate	STA 15.88		± 100°/sec			9 A	80 kHz	6,29	1 kHz	
6	AX-1	Accel X	STA 16.5		± 100 g			4 A	40 kHz	1,24	1 kHz	
7	AX-2	Accel X	STA 16.5		± 50 g			5 A	48 kHz	2,25	1 kHz	
8	AX-3	Accel X	Adapter		+ 125 - 75 g		60 SPS	19 B	160 kHz	11,34	60 SPS	
9	AY-1	Accel Y	STA 16.5		± 40 g		CONT.	6 A	56 kHz	3,26	1 kHz	
10	AY-2	Accel Y (Offset)	STA 22.75		± 50 g			8 A	72 kHz	5,28	1 kHz	
11	AZ-1	Accel Z	STA 16.5		± 50 g 12/10/73			7 A	64 kHz	4,27	1 kHz	
12	S-1	Pos "G" SW	TLM SYS		2.88 to 1.5v T+1sec		30 SPS	19 B	160 kHz	12	30 SPS	
13	TER T	TER TIMER			3.5v to 0 T+4.7sec		30 SPS			13	30 SPS	
14	TER SQ	TER SQ1 FIRE			0 to 4.5v T+4.7sec		30 SPS			14	30 SPS	
15	TER SQ	TER SQ2 FIRE			0 to 3.2v T+4.7sec		30 SPS			15	30 SPS	
16	REC T	REC TIMER			3.5v to 0 T+7.6sec		30 SPS			17	30 SPS	
17	REC SQ	REC SQ1 FIRE			0 to 4.5v T+9.6sec		30 SPS			18	30 SPS	

TABLE B-I (continued)

TELEMETRY DATA LIST PROPOSAL

1/23/74

H. D. Sorensen - 8183

ROLL TORQUE EVALUATION UNIT (RTEU)

RTE DATA LIST								TELEMETRY CHANNEL ASSIGNMENT				
ITEM	SYMBOL	MONITOR DESCRIPTION	TEST POINT LOCATION	AGENCY	REQUIRED MEASUREMENT	REQUIRED ACCURACY	REQ. RESP.	VCO CH.	VCO FREQ.	PAM CH.	RESPONSE	ACCURACY
18	REC SQ	REC SQ2 FIRE	TLM SYS	8362	0 to 3.2v T + 9.6sec	5%	30 SPS	19B	160 kHz	19	30 SPS	5%
19	SEP T	SEP TIMER			3.5v to 0 T + 12.1sec		30 SPS			20	30 SPS	
20	SEP S2	NEG "G" SW			1.5 to 2.5v T + 115sec		30 SPS			21	30 SPS	
21	SEP SQ	SEP SQ FIRE			0 to 4.5v T + 12.1sec		30 SPS			22	30 SPS	
22	SEP S3	SEP SW MON			1.5 to 2.5v T+12.1sec		30 SPS			23	30 SPS	
23	RV T	RV TIMER			3.5v to 0 T + 45sec		30 SPS			35	30 SPS	
24	RV SQ	RV SQ FIRE			0 to 4.5v T + 45sec		30 SPS			36	30 SPS	
25	BATT.	28v MON		8183	0 To 32 VDC		30 SPS			39,40	30 SPS	
26	5 VDC	5v REG.		8183	0 To 5 VDC		30 SPS			41	30 SPS	
27	CAP	CAP BANK		8183	0 To 32 VDC		30 SPS			42	30 SPS	
28	T-1	BATT. TEMP.		8183	38° To 165°F		30 SPS			37	30 SPS	
29	T-3	THERMOCOUPLE	STA 19.00	8362	MAX TEMP 2295°F		20 SPS	21 B	176 kHz	1	20 SPS	
30	T-4				2295°F		20 SPS			2	20 SPS	
31	T-5				1295°F		20 SPS			3	20 SPS	
32	T-6		STA 22.75		2295°F		20 SPS			8	20 SPS	
33	T-7				2295°F		20 SPS			9	20 SPS	
34	T-8				1295°F		20 SPS			10	20 SPS	

TABLE B-I (continued)

TELEMETRY DATA LIST PROPOSAL

1/23/74

H. D. Sorensen - 8183

ROLL TORQUE EVALUATION UNIT (RTEU)

RTE DATA LIST								TELEMETRY CHANNEL ASSIGNMENT				
ITEM	SYMBOL	MONITOR DESCRIPTION	TEST POINT LOCATION	AGENCY	REQUIRED MEASUREMENT	REQUIRED ACCURACY	REQ RESP.	VCO CH.	VCO FREQ	PAM CH.	RESPONSE	ACCURACY
35	T-9	THERMOCOUPLE	0° STA 28.50	8362	Max. Temp 2295°F	5%	20 SPS	21 B	176 kHz	13	20 SPS	5%
36	T-10				2295°F					14		
37	T-11				1295°F					15		
38	T-12		180° STA 2850		2295°F					17		
39	T-13				2295°F					18		
40	T-14				1295°F					19		
41	T-15				1295°F					21		
42	T-16		Recruit fl		1295°F					22		
43	T-17		" "		1295°F					23		
44	T-18	Res Therm	-----		Max. Temp 300°F					27		
45	T-19		-----		480°F					28		
46	T-20		-----		480°F					29		
47	T-2	Thermistor	STA 0;22.75	8183	30° to 150°F					16		
48												
49												
50												
51												

The beacon operates into a phased three-antenna array through a power divider and has a peak power output of 400 watts. The transponder, power divider, and antenna system were located in the adapter section between the reentry vehicle and the recruit rocket. At the time of RV deployment from the rocket motor, the beacon ceased to function, at which time the radar systems attempted to skin track the RV.

The telemetry system internal power source consisted of 20 silver/zinc battery cells molded into a single pack. This battery is capable of delivering 3.5 amperes at 28.5 V for 30 minutes.

Measurements made by this system included a three-axis rate gyro (roll, yaw, and pitch), 5 accelerometers, 15 thermocouples, and 3 resistance thermometers (RTs). Also, there were several circuits monitoring the firing circuit timers and events.

Firing Circuit Description

The firing circuits were designed to provide signals for:

a. Second-stage ignition (Terrier)

b. Third-stage ignition (Recruit)

c. Payload separation

d. Payload recovery parachute deployment

The TATER system and RV deployment and recovery firing circuits are packaged as an entity of the telemetry system and can be seen in Figure B-2.

The primary power source for the firing circuits is the telemetry battery (28 Vdc at 1.5 Ah silver zinc cells). The initiation energy for the explosive devices was obtained from the discharge of a capacitor bank (4 3300 μF - 35 V aluminum computer grade electrolytic capacitors connected in parallel through UT4020 diodes for charging and discharging). Arming of the firing module consists of charging the capacitor bank. Arming is enabled, first, by operating a latching-power control relay to the internal position, and, second, by closing the normally open contact sets of an integrating acceleration (IA) switch. The IA switch (MC2034) operates upon experiencing an approximate 12 g-second product (velocity change), and, in flight, is designed to close at about 0.5 second from lift-off. The charge time constants are such that the capacitors are fully charged in 1.5 seconds after application of voltage.

Firing signals are delivered to initiators by the operation of electronic time-delay contacts. Time delays are activated by the IA switch closure (recruit rocket and parachute deployment) and the positive and negative G-switch sensing device (Terrier rocket and RV deployment). An arming key plug is provided to complete the firing circuits to bridgewires when mated to the payload adapter section.

At approximately two hours prior to launch, the second- and third-stage arming key plug was installed. At approximately two minutes prior to launch, the payload telemetry was turned to internal power; this enables the electrical arming of the firing circuits. After launch, the Talos (first stage) booster acceleration closes an acceleration-time interlock provided by the MC2034 IA switch. The firing energy source (capacitor bank) then starts charging. The IA switch operation time is approximately 0.5 second after launch.

At launch a positive G-switch closes until decay of Talos (first stage) thrust. When the G-switch opens, a timer is started, 0.01 seconds later igniting the second-stage motor (Terrier). At Terrier (second stage) ignition the G-switch closes again and remains closed until the decay of Terrier thrust. When the IA switch closes, a time delay of 6.6 ± 0.1 seconds is started to switch the output of the G-switch timer from the Terrier initiator to the Recruit initiator. When the G-switch opens again at Terrier decay, the timer is restarted, 0.01 second later igniting the third-stage motor (Recruit). When the third stage is spent, a negative G-switch is sensed at -20g for 600 milliseconds to separate the payload and recovery system from third stage. The parachute deployment timer is preset to operate in 45 seconds after IA switch closure for RV recovery operation.

APPENDIX C--SUMMARY OF BALLISTIC COMPUTATIONS AND RANGE SAFETY

The preflight ballistic computations, performed by L. R. Rollstin, Division 5624, and presented in References 18 and 19, are summarized in Table C-I. A complete analysis of the system impact footprint is presented in Figure C-1. This shows both the expected nominal and anomalous (3σ) impact dispersion for the three booster motors and the RTE payload.

TABLE C-I

SUMMARY OF TATER/RTE BALLISTIC COMPUTATIONS

1. TATER - RTE Payload Separation Conditions

Time	12.1 s
Altitude	12,400 ft MSL
Velocity	9290 ft/s
Mach No.	8.8
Dyn Press	70,900 lb/ft^2
Range	49,500 ft
γ	7.0 deg

2. Separation Acceleration (Payload and Booster) = 5 g

3. Recovery System Deployment Conditions

Time	47.1 s
Altitude	14,900 ft MSL
Velocity	890 ft/s
Range	148,400 ft
γ	- 27.1 deg

4. Apogee Conditions

Time	28.1 s
Altitude	19,030 ft MSL
Velocity	2230 ft/s
Range	123,850 ft

Summary of Recovery System Operation TATER/RTE

@ Pilot Deploy

	t = 47.1			
η = 14,900 ft	v = 890 ft/s	q = 610 lb/ft^2	γ = -27.1 deg	R = 148,400 ft

@Main Deploy

	t = 57.1			
η = 12,100 ft	v = 300 ft/s	q $\cong$ 70 lb/ft^2	γ = -58.4 deg	R = 151,500 ft

@Impact

	t = 163.1 s			
η = 5100 ft	v = 63 ft/s	q = 4 lb/ft^2	γ = -90 deg	R = 151,700 ft

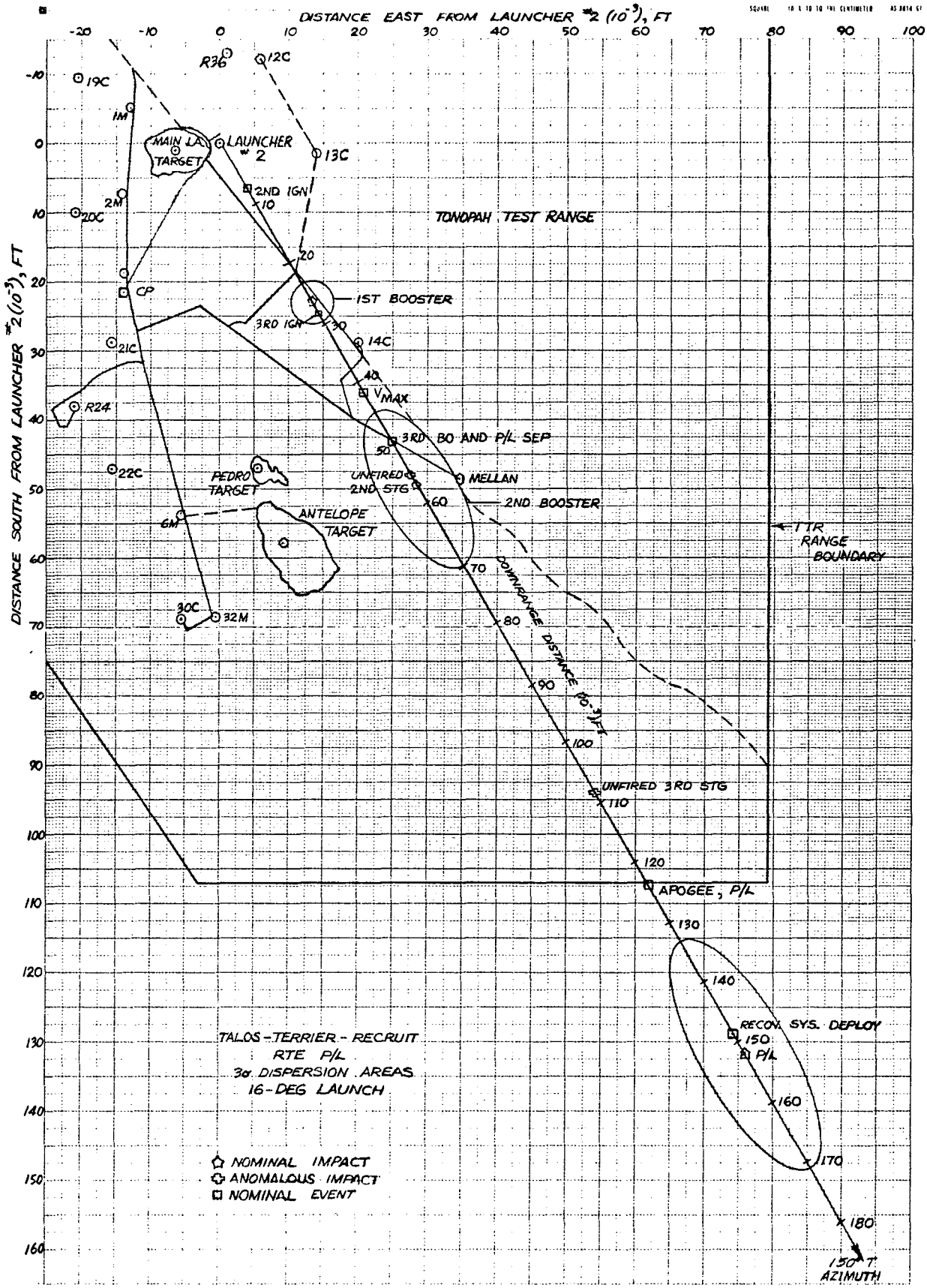

Figure C-1. RTE/TATER Dispersion Areas

APPENDIX D--RTE POSTFLIGHT TRAJECTORY SIMULATION

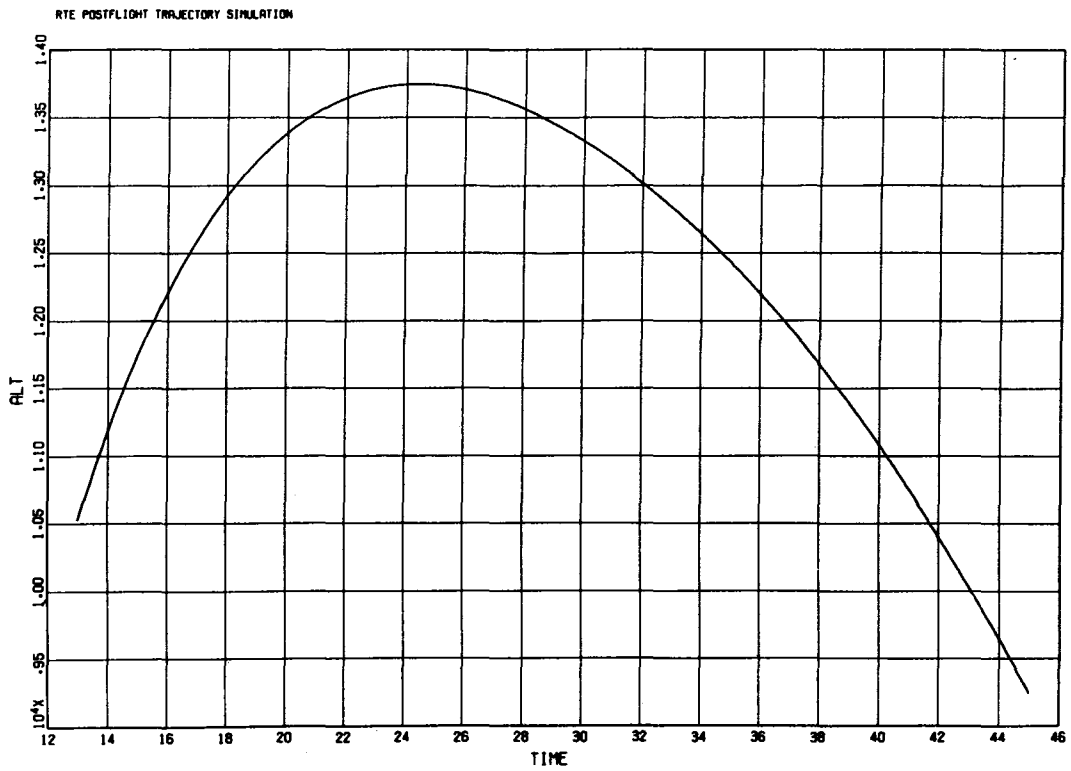

Figure D-1. RTE Altitude History From Postflight Simulation

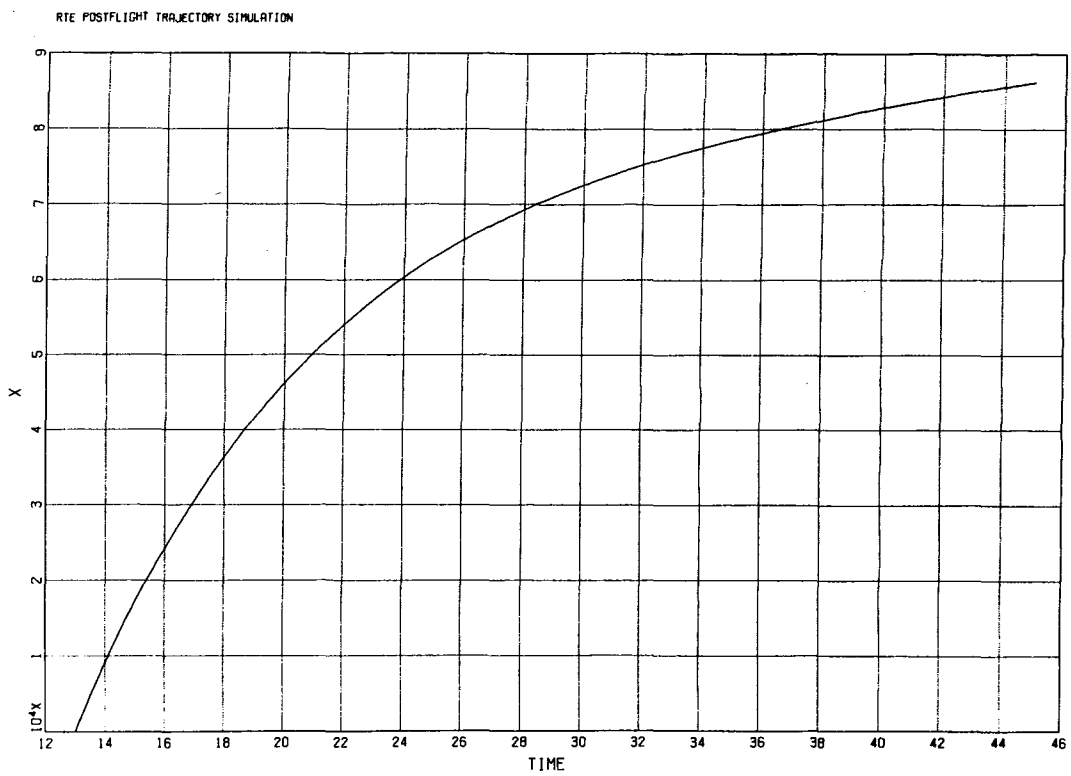

Figure D-2. Range

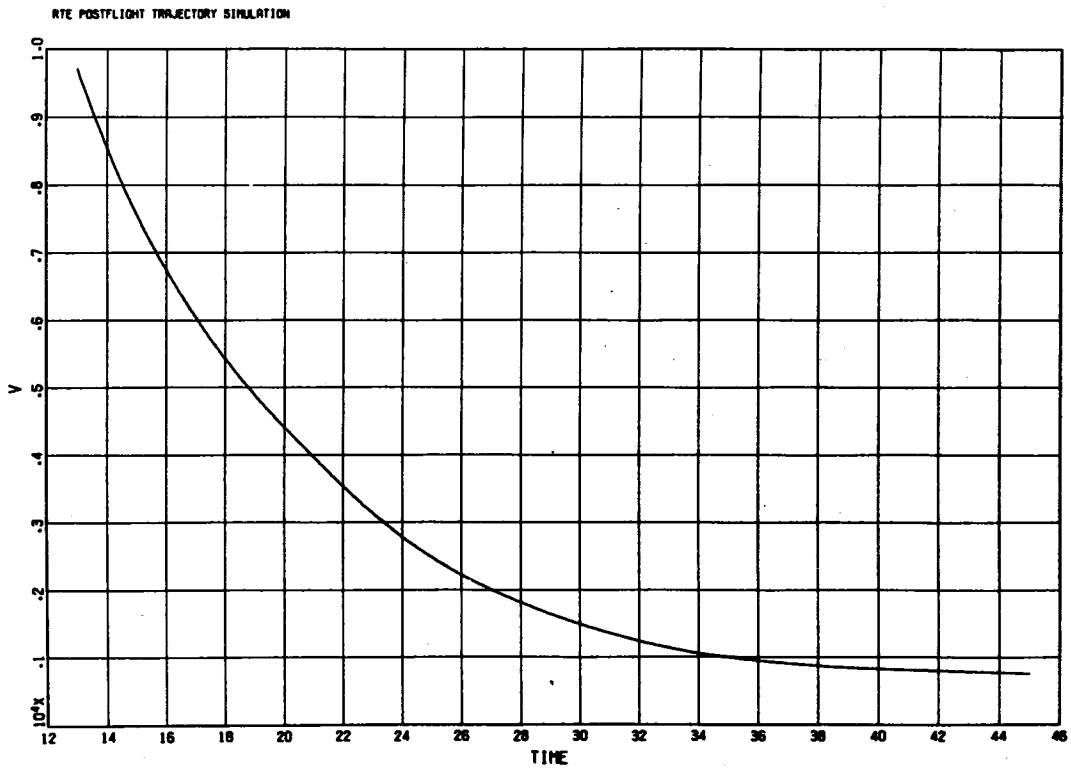

Figure D-3. Velocity

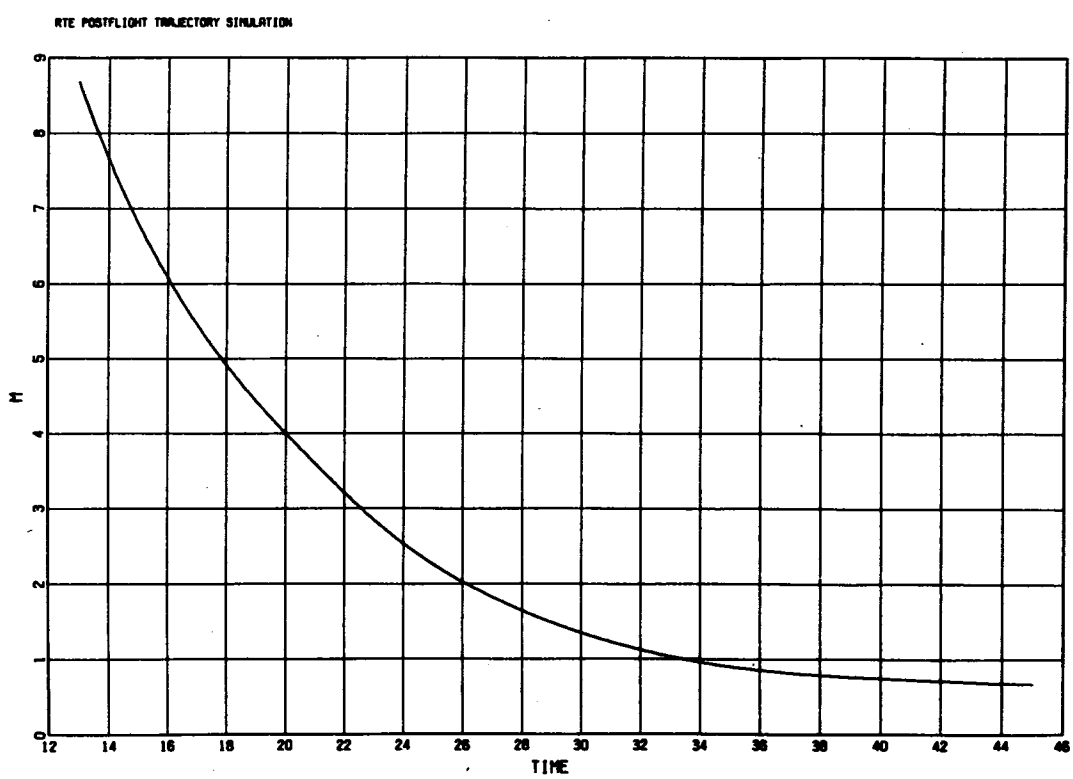

Figure D-4. Mach Number

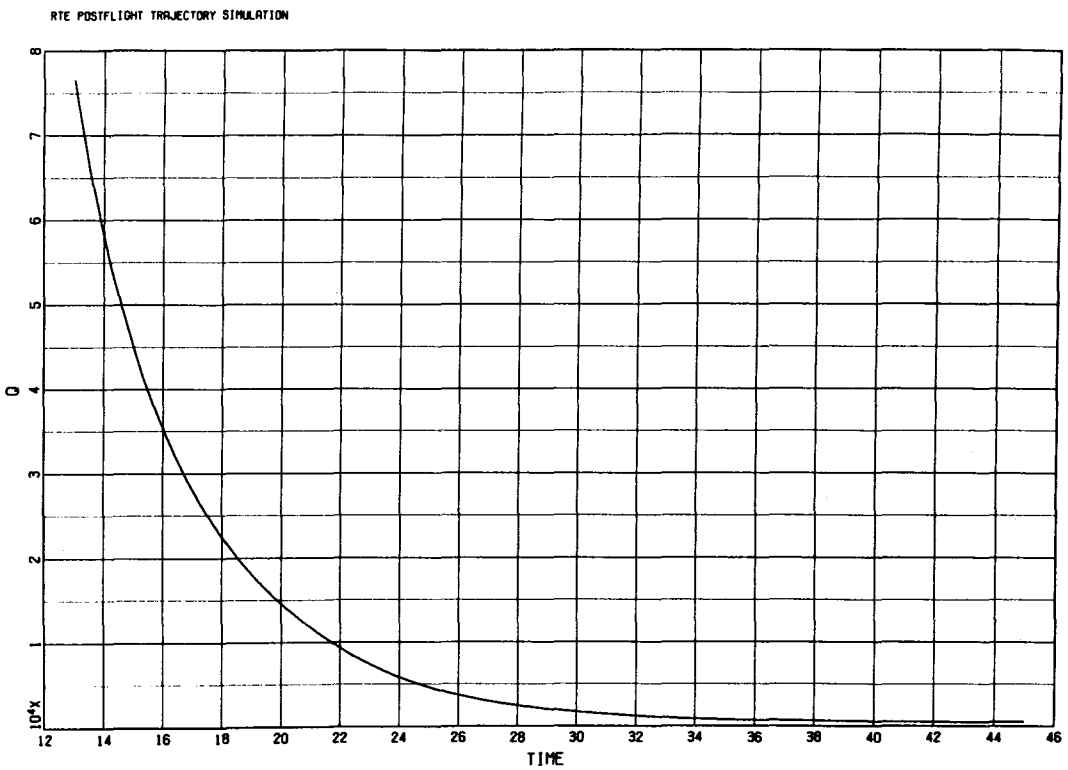

Figure D-5. Dynamic Pressure

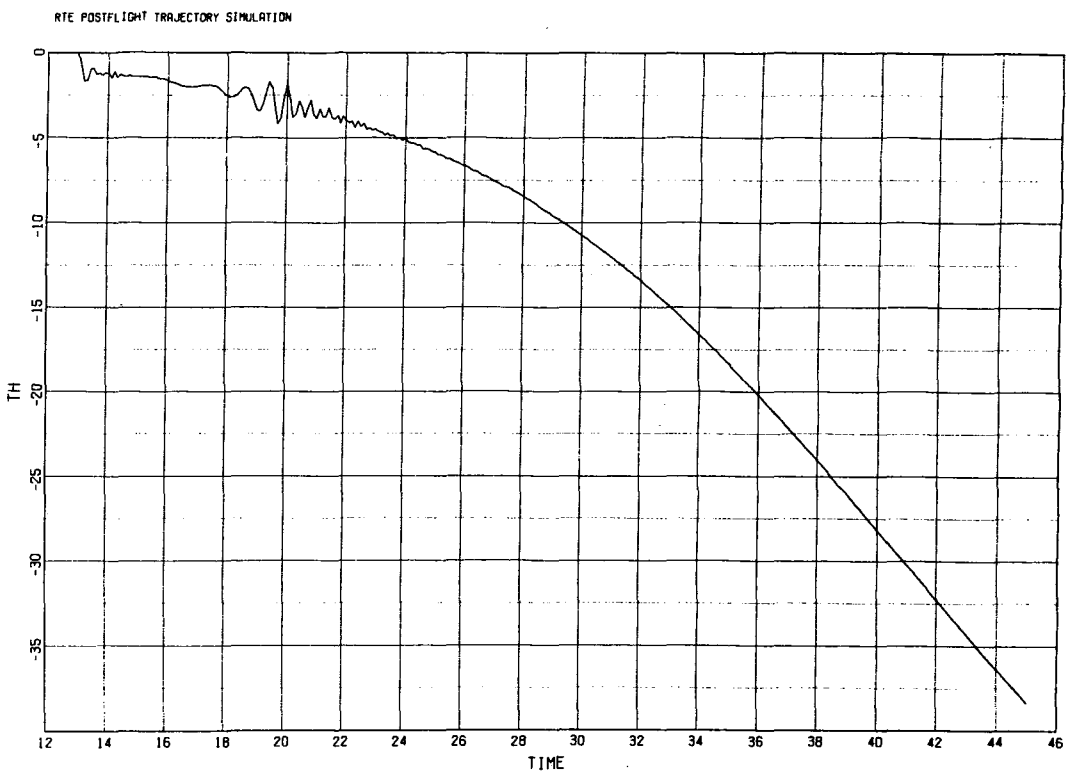

Figure D-6. Pitch Angle

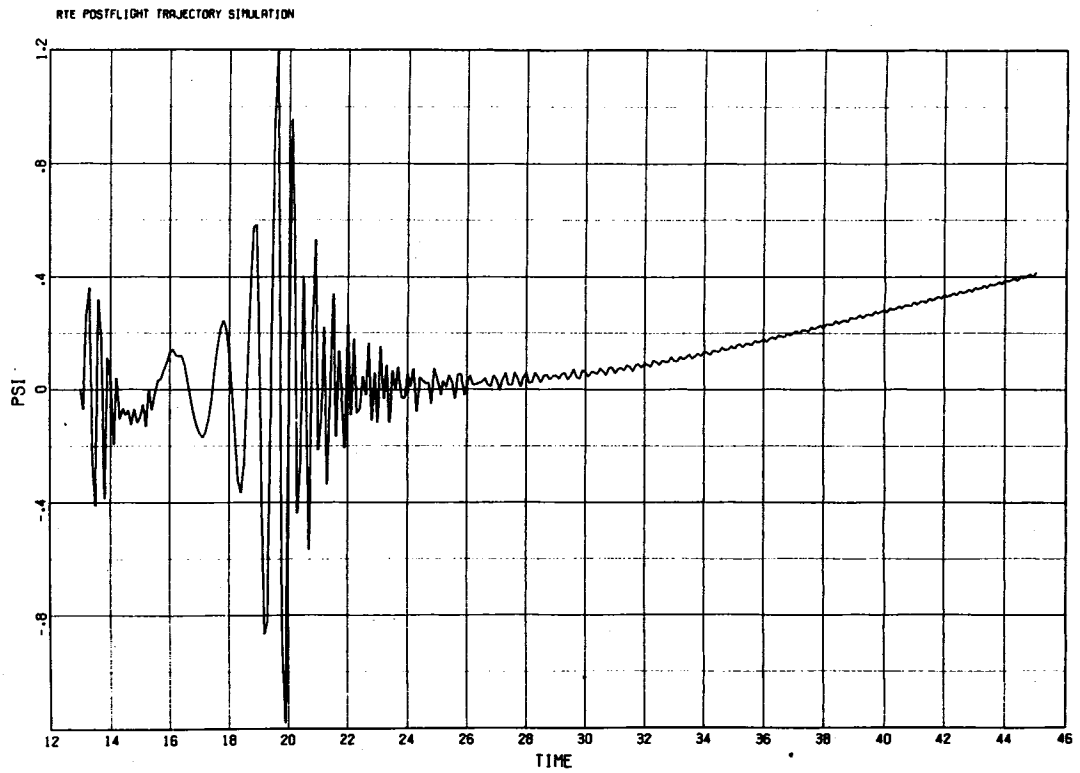

Figure D-7. Yaw Angle

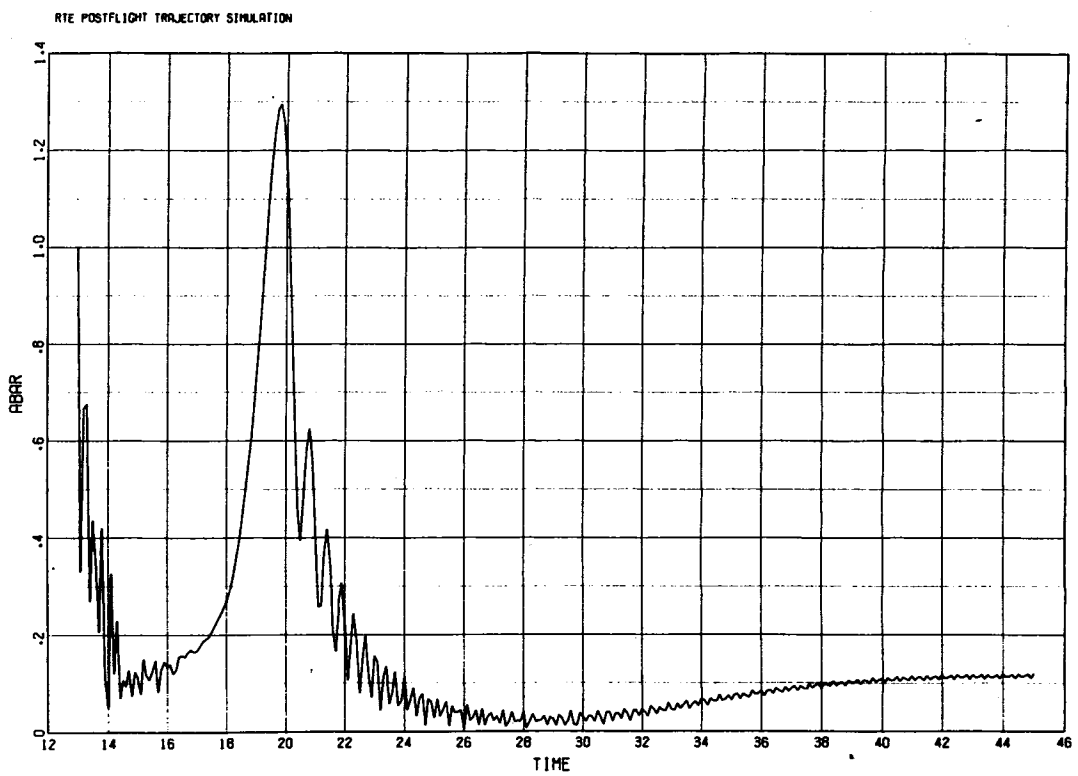

Figure D-8. Total Angle of Attack

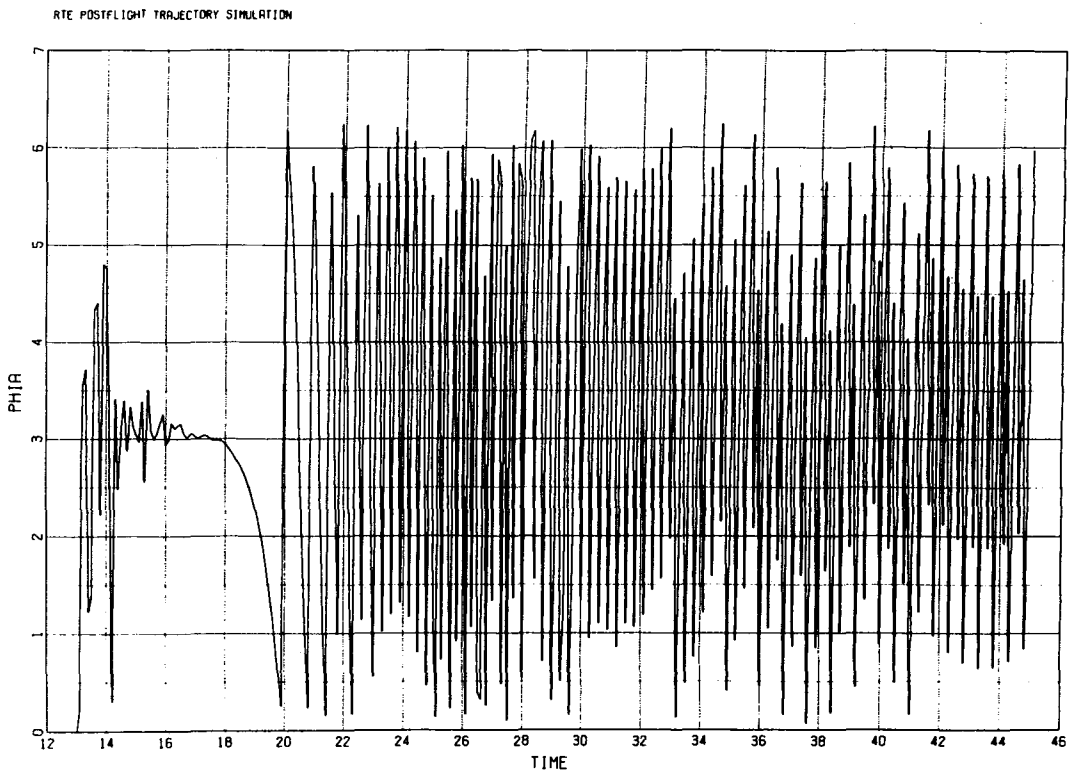

Figure D-9. Aerodynamic Roll Angle

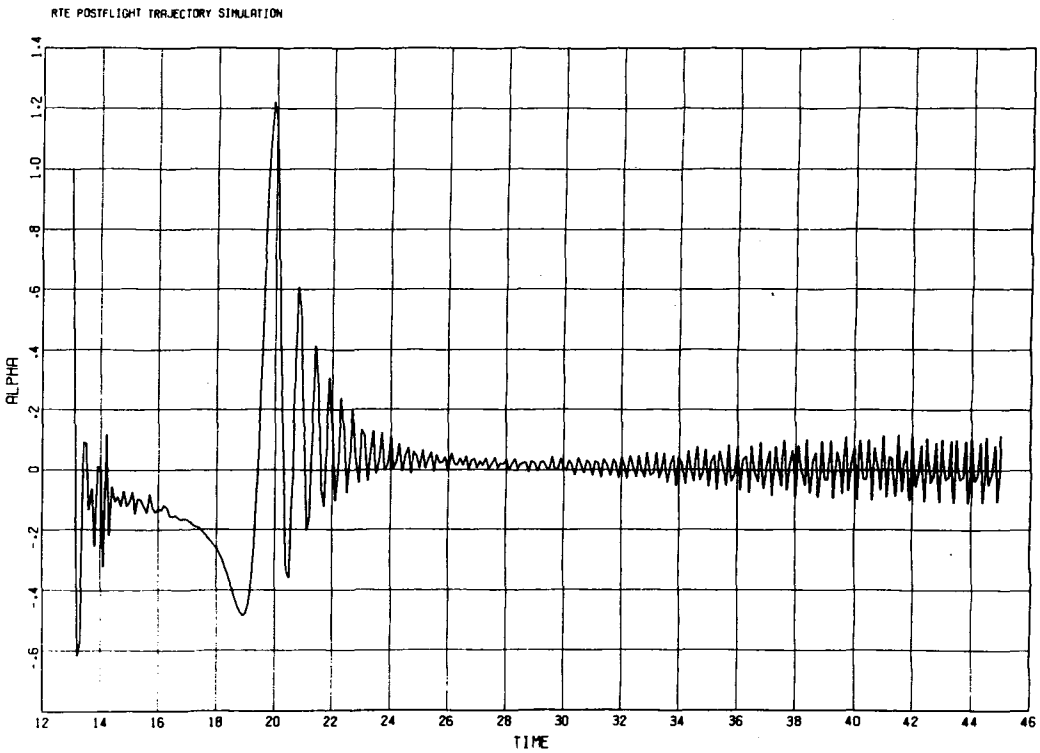

Figure D-10. Angle of Attack

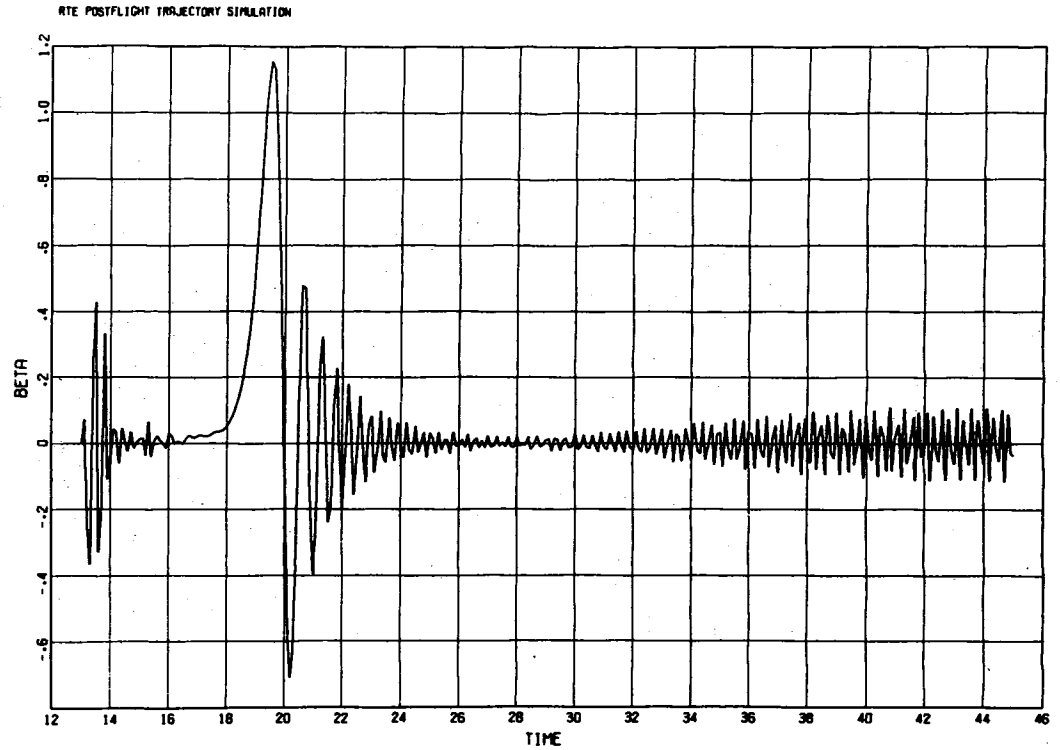

Figure D-11. Angle of Sideslip

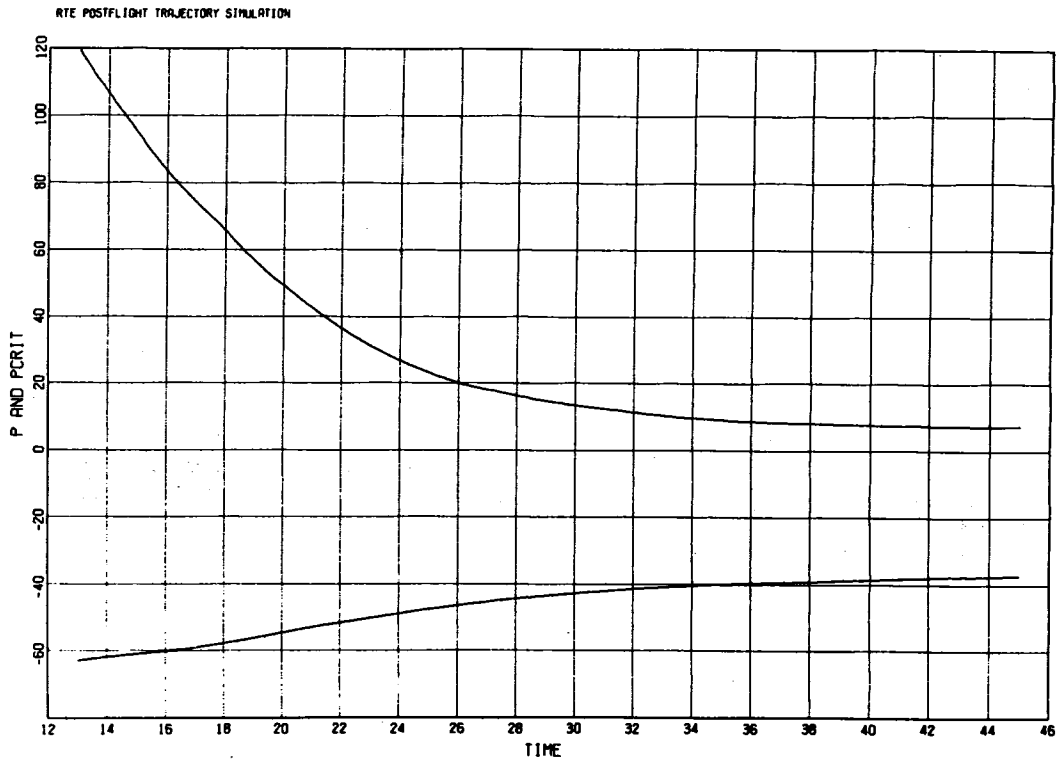

Figure D-12. Spin Rate and Natural Pitch Frequency

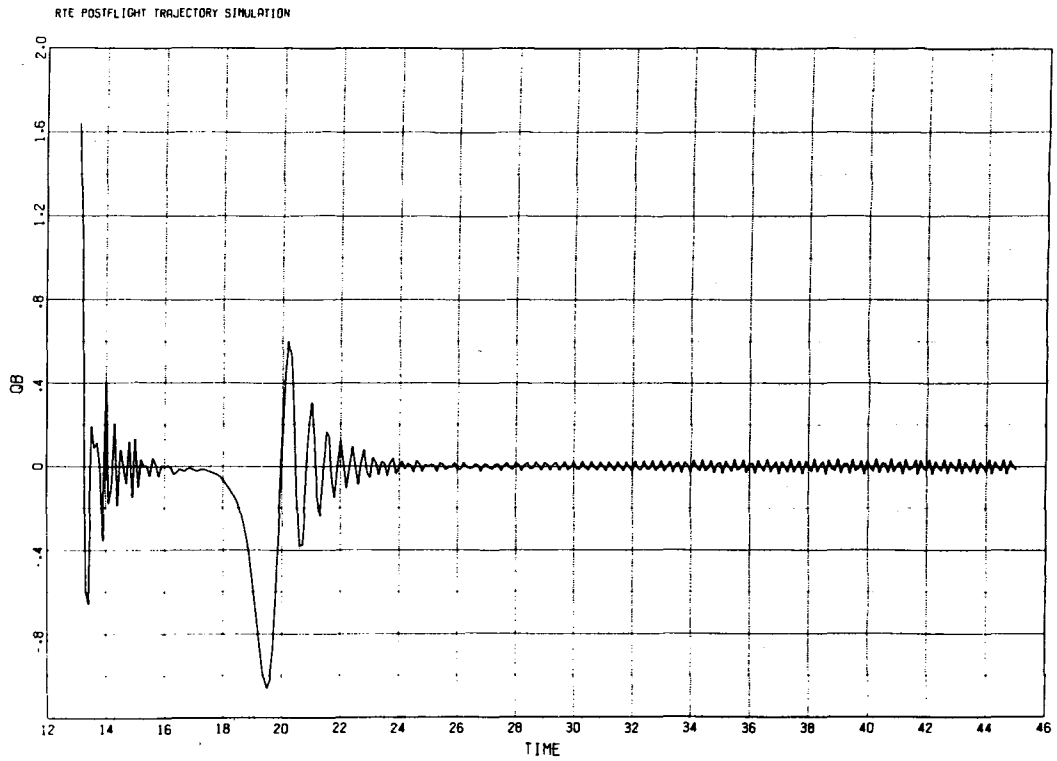

Figure D-13. Pitching Velocity

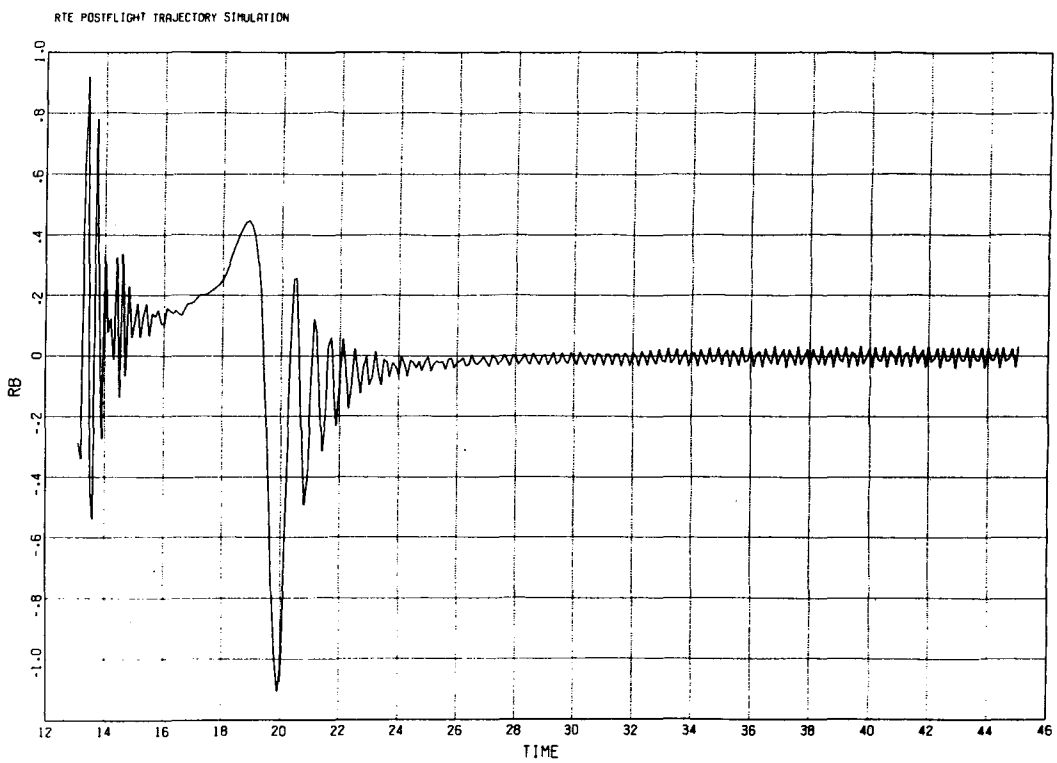

Figure D-14. Yawing Velocity

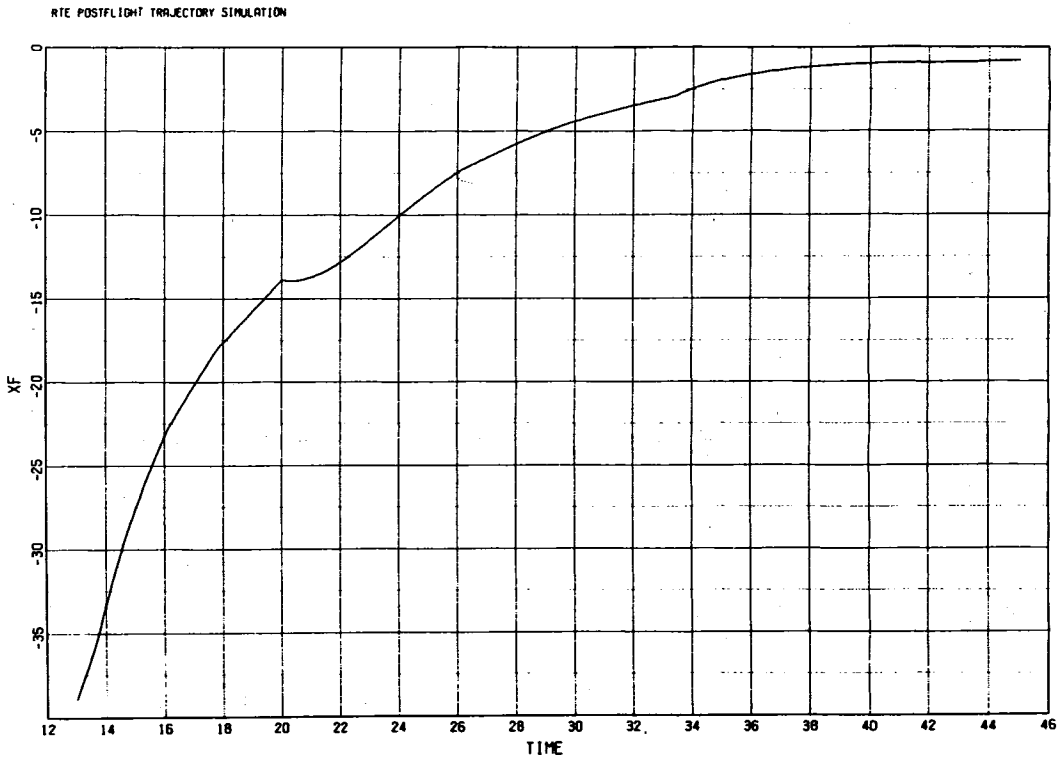

Figure D-15. Axial Acceleration

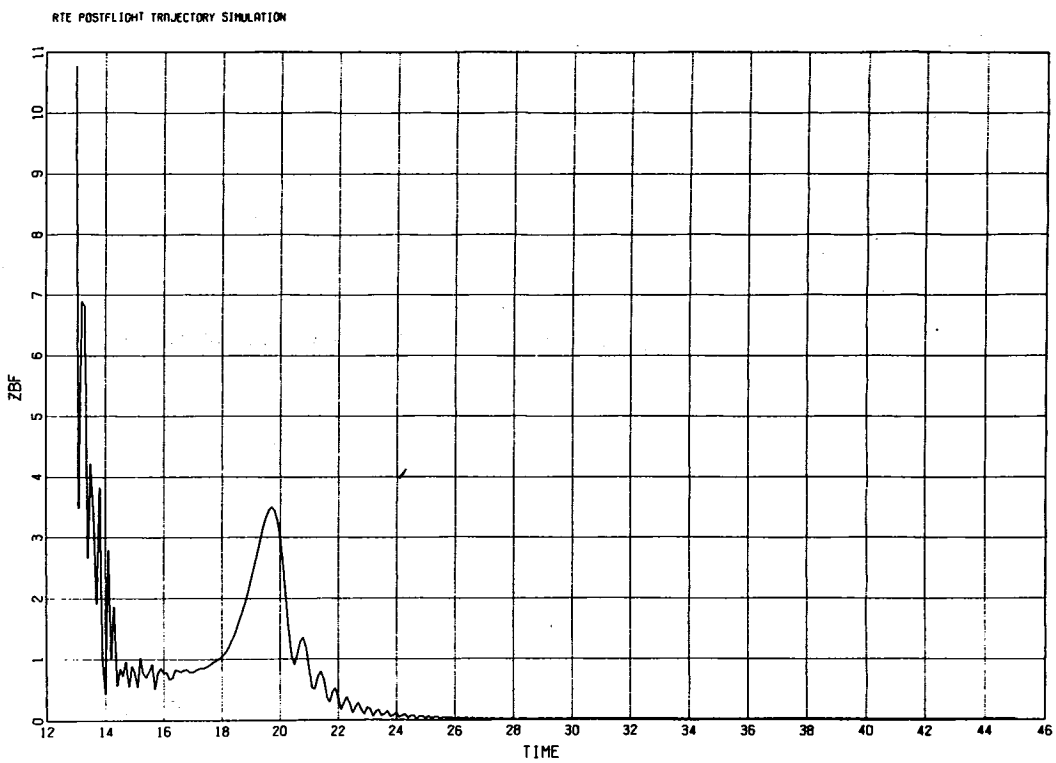

Figure D-16. Total Lateral Acceleration

UNLIMITED RELEASE

INITIAL DISTRIBUTION

Director
Strategic Systems Project Office
Department of the Navy
Washington, D.C. 20376
Attn: CDR L. Stoessl, SP272
H. A. McMasters, SP2721

Naval Plant Representative Office (SPL)
Lockheed Missiles and Space Company
P. O. Box 504
Sunnyvale, CA 94088
Attn: Lt. R. Benzin, SPL-32

Lockheed Missiles and Space Co., Inc.
P. O. Box 504
1111 Lockheed Way
Sunnyvale, CA 94088
Attn: R. W. Carlson, 81-23/154
L. D. Hull, 81-11/154
L. G. Quan, 81-23/154

SAMSO
Air Force Systems Command
Norton AFB, CA 92409
Attn: Col. W. Villines, MNNR
A. Burgess, TRW
W. Crawford, TRW

SAMSO
Air Force Systems Command
P. O. Box 92960
Los Angeles, AFS, CA 90009
Attn: Lt. Col. E. P. Brininstool, RSSR
Lt. Col. W. Goldberg, RSSE
Col. D. Dowler

Commanding Officer
Naval Surface Weapons Center
White Oaks Laboratory
Silver Spring, MD 20910
Attn: C. Lyons, Code 323
R. Feldhuhn
A. M. Morrison

Ballistic Defense Program Office
Commonwealth Building
1300 Wilson Blvd.
Arlington, VA 22209
Attn: J. G. Gilstein
V. S. Kupelian

Commanding Officer
Naval Surface Weapons Center
Dahlgren Laboratory
Computation and Analysis Laboratory
Dahlgren, VA 22448
Attn: R. Hewey
T. A. Clare

The Johns Hopkins University
Applied Physics Laboratory
8621 Georgia Avenue
Silver Spring, MD 20910
Attn: L. S. Glover

Director
Defense Nuclear Agency
Washington, D.C. 20305
Attn: J. Moulton

National Aeronautics and Space Admin.
Ames Research Center
Thermal Projection Branch, Bldg. 234
Moffett Field, CA 94035
Attn: H. Larson
P. Nachtsheim

Los Alamos Scientific Laboratory
Los Alamos, NM 87544
Attn: R. Olwin (ADW-PM)

AVCO Corporation
AVCO Systems Division
201 Lowell St.
Wilmington, MA 01887
Attn: R. Cooper

General Electric Company
3198 Chestnut St.
Philadelphia, PA 19101
Attn: R. Larmour, Rm. 6258F

Aerospace Corporation
P. O. Box 92957
Los Angeles, CA 90009
Attn: D. Nowlan
W. J. Portenier
D. H. Platus
R. Allen

Calspan Corporation
P. O. Box 235
Buffalo, N.Y. 14221
Attn: M. Holden

Kaman Sciences Corporation
P. O. Box 7463
Colorado Springs, Colorado 80933
Attn: F. Barbera
P. Wells
J. Forkois
D. Foxwell
E. Daugs

Director of Defense Research and Engineering
Rm. 3E-1006, The Pentagon
Washington, D.C. 20301
Attn: R. Ruffine
J. Persh

W. J. Howard, 2
G. A. Fowler, 1000
T. B. Lane, 1280
D. B. Shuster, 1300
A. A. Lieber, 1310
M. L. Kramm, 1320
D. J. Rigali, 1323
E. C. Rightley, 1324; Attn: R. D. Fellerhoff
R. C. Maydew, 1330
H. R. Vaughn, 1331
G. G. Wilson, 1331
D. F. McVey, 1332; Attn: D. W. Johnson
S. McAlees, 1333
C. W. Peterson, 1334
W. R. Barton, 1335
L. R. Rollstin, 1335
R. G. Clem, 1350
R. L. Peurifoy, 4300
C. H. Mauney, 4330
B. E. Bader, 4337

T. B. Cook, Jr., 8000
L. Gutierrez, 8100
A. N. Blackwell, 8110
A. F. Baker, 8111
R. M. Green, 8111
C. S. Hoyle, 8113; Attn: L. E. Voelker
D. E. Gregson, 8150
A. S. Rivenes, 8158
J. K. Kryvoruka, 8158 (5)
R. D. Cozine, 8160
W. G. Wilson, 8165; Attn: B. D. Pontsler
D. M. Pegan, 8168
C. S. Selvage, 8180
R. I. Peterson, 8183; Attn: H. D. Sorenson
D. C. Stoner, 8183-1
C. H. DeSelm, 8200
B. F. Murphey, 8300
T. T. Bramlette, 8313
T. S. Gold, 8320
J. L. Wirth, 8340
J. F. Barham, 8360
G. R. Otey, 8362
G. W. Henderson, 8362
W. C. Scrivner, 8400
R. A. Baroody, 8410
S. G. Cain, 8412
L. R. Myers, 8412
Technical Publications and Art Division, 8265, for TIC (2)
F. J. Cupps, 8265/Technical Library Processes Division, 3141
Technical Library Processes Division, 3141 (4)
Library and Security Classification Division, 8266-2 (5)